論文 / 著書情報
Article / Book Information

題目(和文)	
Title(English)	Field-driven successive phase transitions and magnetic excitations of spin-1/2 frustrated antiferromagnet Ba2CoTeO6
著者(和文)	チャンラートプリントーン
Author(English)	Purintorn Chanlert
出典(和文)	学位:博士(学術), 学位授与機関:東京工業大学, 報告番号:甲第10674号, 授与年月日:2017年9月20日, 学位の種別:課程博士, 審査員:田中 秀数,井澤 公一,笹本 智弘,古賀 昌久,吉野 淳二
Citation(English)	Degree:Doctor (Academic), Conferring organization: Tokyo Institute of Technology, Report number:甲第10674号, Conferred date:2017/9/20, Degree Type:Course doctor, Examiner:,,,,
学位種別(和文)	博士論文
Type(English)	Doctoral Thesis

FIELD-DRIVEN SUCCESSIVE PHASE TRANSITIONS AND MAGNETIC EXCITATIONS OF SPIN-1/2 FRUSTRATED ANTIFERROMAGNET Ba_2CoTeO_6

PURINTORN CHANLERT

A THESIS SUBMITTED IN PARTIAL FULFILLMENT
OF THE REQUIREMENTS FOR
THE DEGREE OF DOCTOR OF PHILOSOPHY
(PHYSICS)
GRADUATE SCHOOL OF SCIENCE AND
ENGINEERING
TOKYO INSTITUTE OF TECHNOLOGY
2017

ACKNOWLEDGEMENTS

I would like to first express my sincere gratitude to my PhD. dissertation advisor, Prof. Hidekazu Tanaka, for his invaluable advice and encouragement throughout the PhD program. My deep gratitude also go to Asst. Prof. Nobuyuki Kurita for his expertise and insightful advice, valuable discussions and the support of the whole course of study. I am also thankful to Prof. Koichi Kindo and Asst. Prof. Akira Matsuo of the Institute for Solid State Physics (ISSP), The University of Tokyo, Kashiwa, Chiba, for supporting high field magnetization measurement. and Prof. Hiroyuki Nojiri, Assoc. Prof. Motoi Kimata, and Asst. Prof. Takumi Kihara of the Institute for Materials Research (IMR), Tohoku University, Sendai, Miyagi, for their kind comments and support about high field specific heat and ESR measurements. I am also thankful to Assoc. Prof. Kittiwit Matan for providing me an opportunity to do short-term research at TITECH prior to the start of the PhD course.

I express my sincere thanks to the Japan Society for the Promotion of Science (JSPS) for granting the research budget throughout PhD program. I gratefully acknowledge the Ministry of Education, Culture, Sports, Science and Technology (MEXT) of the government of Japan for giving me such a great opportunity and scholarship to attend doctoral course at Tokyo Institute of Technology. I am particularly indebted to the Development and Promotion of Science and Technology Talents Project (DPST), funded by the Royal Thai Government for the scholarship which enabled me to undertake the study from undergrad through out the master degree. I also wish to thank the Department of Physics of Tokyo Institute of Technology for their support.

I have learnt a lot from the people that I have worked with in the laboratory of Prof. Hidekazu Tanaka in TITECH during these years. Words are inadequate to express my thanks to Dr. Kazuya Katayama for his expertise and insightful advise for frustrated magnetic system. My deep gratitude toward Mr. Masari Watanabe for assisting and supporting the high-field specific heat measurement. The support from all other colleagues is also gratefully acknowledged, in particular, Mr. Takuya Susuki, Mr. Kazuya Yokota, Ms. Makiko Okada, Mr. Tomoyuki Koga, Ms. Saya Ito, Mr. Masato Koike, Mr. Kazuki Shirasawa, and so on.

Special thanks go to Dr. Thana Sutthibutpong and Dr. Ganatee Gitgeatpong for their support and advises on theoretical physics parts. I am grateful to the help of Dr. Supanut Chaidee for the instruction on MATLAB. I am also thankful to Dr. Norrarat Siribuddhaiwan and Mr. Thanate Kerdkaew for their advises on scientific investigation,

and critical thinking. I am also thankful to Dr. Puwis Amatyakul, and Mr. Hamdan Akbar Notonegoro for the encouragement and exhorting during PhD research. In addition, I express my special thanks to Mr. Sukho Kongtawong for his comments and help with LaTeX.

I greatly appreciate all my friends for their kind help on numerous occasions. Finally, I express my sincere gratitude to my family for their encouragement and support throughout my course of study.

Purintorn Chanlert

FIELD-DRIVEN SUCCESSIVE PHASE TRANSITIONS AND MAGNETIC EXCITATIONS OF SPIN-1/2 FRUSTRATED ANTIFERROMAGNET Ba_2CoTeO_6.

PURINTORN CHANLERT 14D50012

Ph.D. (PHYSICS)

THESIS ADVISOR : PROF. HIDEKAZU TANAKA, Ph.D. (PHYSICS)

ABSTRACT

Ba_2CoTeO_6 has a trigonal structure with space group $P\bar{3}m$, in which Co^{2+} with effective spin-1/2 is surrounded octahedrally by six O^{2-} ions. There are two Co^{2+} sites, Co(1) and Co(2). Co(1) sites form a two-dimensional (2D) triangular lattice parallel to the *ab*-plane, while Co(2) sites form a double-layered triangular lattice. The exchange interactions for Co(2) can be mapped onto a honeycomb lattice with the nearest-neighbor J_1 and the next-nearest-neighbor J_2 interactions. Thus Ba_2CoTeO_6 is consists of two subsystems, (A) and (B) composed of Co(1) and Co(2), respectively. In this study, we investigated magnetic properties of Ba_2CoTeO_6 via magnetization and specific heat measurements using single crystals. Magnetic phase transitions take place at $T_{N1} = 11.9$ K and $T_{N2} = 12.9$ K. Subsystem (A) exhibits the magnetization plateau at one-third of the saturation magnetization for $H \perp c$, which is characteristic of the triangular lattice quantum antiferromagnet. Subsystem (B) displays three metamagnetic transitions for $H \parallel c$, which is characteristic of Ising antiferromagnet with competing exchange interactions. From these experimental results it was found that subsystems (A) and (B) are described as $S = 1/2$ triangular lattice Heisenberg antiferromagnet with the weak easy-plane anisotropy and honeycomb lattice J_1-J_2 Ising antiferromagnet, respectively, and that these two subsystems are almost decoupled. In addition to these studies, Electron Spin Resonance (ESR) measurement has been performed. Collective ESR mode for subsystem (A) and local mode for subsystem (B) have been observed at 1.5 K ($< T_{N2}$) for $H \parallel c$. From the analyses of these ESR data combined with the magnetization data, we evaluated exchange parameters and g-factors of both subsystems.

KEY WORDS : HEISENBERG TRIANGULAR LATTICE ANTIFERROMAGNET / ISING J_1-J_2 HONEYCOMB LATTICE ANTIFERROMAGNET / FRUSTRATION IN MAGNETS / Ba_2CoTeO_6

98 pages

CONTENTS

CONTENTS (CONT.)

LIST OF FIGURES

CHAPTER 1

INTRODUCTION

1.1 S=1/2 Quasi-2D Frustrated Antiferomagnet Ba_2CoTeO_6

In this doctoral dissertation, the compound we were working on is Ba_2CoTeO_6. The uniqueness of this compound is that its magnetic structure is composed of two subsystems including (A) Heisenberg triangular lattice antiferromagnet (TLAF) and (B) Ising honeycomb lattice antiferromagnet (HLAF). In this compound, Co^{2+} plays an important role as a magnetic ion where its fictitious spin is one-half ($S = 1/2$) instead of true spin, three-half ($S = 3/2$) [1, 2]. In this introduction chapter, we will briefly explain the reason why Co^{2+} displays fictitious spin 1/2. Moreover, there will be a description why quantum fluctuation was supposed to play a role in stabilizing ground states in this compound originated from magnetic frustration. Quantum fluctuation is important in frustrated quantum magnets because it can lift the degeneracy of classical ground state and stabilizes a specific ground states, which leads to the emergence of the exotic quantum state such as up-up-down (uud) structure accompanied with the magnetization plateau at one-third of the saturation magnetization M_s [3–12]. As we will see below, quantum magnetic properties of subsystem A in Ba_2CoTeO_6 are closely related to those observed in $S = 1/2$ Heisenberg TLAF $Ba_3CoSb_2O_9$ [13–19]. Competition of exchange interactions in Ising-like subsystem B produces magnetic-field-induced three-stage successive phase transitions, although the quantum effect discussed in the case of Heisenberg model [20–23] is not observed. Finally, we will state the purpose and the originality of this doctoral dissertation.

1.2 Cobalt Ion (Co^{2+}) with the Fictitious Spin-1/2

Here, we describe briefly the low-temperature effective model of Co^{2+} ion using the fictitious spin-1/2. Considering Ba_2CoTeO_6 crystal structure, Co^{2+} ion is under an

octahedral environment coordinated by six O^{2-} ions similar to Co^{2+} ion in $Ba_3CoSb_2O_9$ [24]. For an independent Co^{2+} ion, there are seven electrons in 3d orbital ($3d^7$) with the total angular momentum $L=3$ and total spin $S=3/2$ in the ground state. The orbital ground state is seven-fold degenerate. When Co^{2+} is in octahedral environment, energy states splits into three energy levels with two triply degenerate states and one nondegenerate state [1, 2]. Because the energy difference between the lowest two orbital state is of order of 1 eV, it is enough to consider only the lowest orbital triplet state. Within the lowest orbital state, the matrix element of L_α ($\alpha=x,y$ and z) is given by $-(3/2)l_\alpha$ using the matrix element l_α of $l=1$. Thus we can replace $\boldsymbol{L}$ with $-(3/2)\boldsymbol{l}$. The splitting of the lowest orbital state is caused by the spin-orbit coupling and trigonal crystalline field due to the trigonal distortion of the octahedron, which are expressed as

$$\mathcal{H}' = -\frac{3}{2}k\lambda(\boldsymbol{l}\cdot\boldsymbol{S}) - \delta\{(l_z)^2 - 2/3\}, \tag{1.1}$$

where the first and second terms are the spin-orbit coupling and the trigonal crystalline field potential. Coefficients λ and δ are their coupling constants. k with $0 < k \leq 1$ is the reduction factor that expresses the reduction of the matrix elements of the angular momentum $\boldsymbol{l}$ due to the mixing of the p orbital of the surrounding O^{2-} with the $3d$ orbital of Co^{2+}. We write $\lambda' = k\lambda$. The eigenenergies and eigenstates corresponding to the Hamiltonian of Eq. (1.1) are classified using $m = l_z + S_z$ as shown in Table 1.1.

$m = l_z + S_z$	$\lvert l_z, m_z\rangle$	Eigenvalue
5/2	$\lvert 1, 3/2\rangle$	E_l
3/2	$\lvert 1, 1/2\rangle$, $\lvert 0, 3/2\rangle$	${E_q}^+$, ${E_q}^-$
1/2	$\lvert 1, -1/2\rangle$, $\lvert 0, 1/2\rangle$, $\lvert -1, 3/2\rangle$	${E_c}^{(0)}$, ${E_c}^{(1)}$, ${E_c}^{(2)}$

Table 1.1: Eigenvalues and eigenstates of Co^{2+} ion produced by the spin-orbit coupling and trigonal crystalline field in octahedral environment.

Since the matrix elements of $|l_z, m_z\rangle$ are identical to those in $|-l_z, -m_z\rangle$, energy levels are

doubly degenerate. This doubly degenerate state is called Kramer's doublet. We have six Kramers doublets as shown in Table 1.1. Their eigenvalues are classified as: one linear E_l ($m = \pm\frac{5}{2}$), two quadratics $E_q{}^+$, $E_q{}^-$ ($m = \pm\frac{3}{2}$) and three cubics $E_c{}^{(0)}$, $E_c{}^{(1)}$, $E_c{}^{(2)}$ ($m = \pm\frac{1}{2}$). All energy eigenvalues are plotted in the graph displayed in Figure 1.1 as a function of δ/λ'. The doublet state with lowest energy level is $E_c{}^{(0)}$.

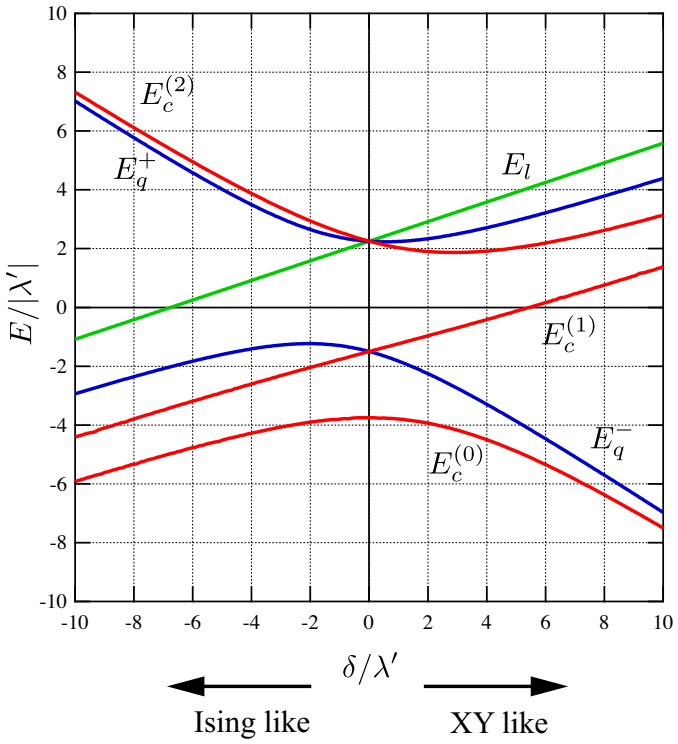

Figure 1.1: Energy doublets of spins in Co^{2+} ions in octahedral environment, where the energy splitting is caused by spin-orbit coupling and trigonal distortion of the octahedron. The doublet state with lowest energy level is $E_c{}^{(0)}$ [2]

We have only to consider the lowest doublet ($E_c^{(0)}$) in case that the temperature is much lower than $|\lambda'|/k_B \simeq 250$ K. Wave function $\psi_\pm^{(0)}$ of the lowest doublet state is expressed by the linear combination of $|\mp 1, \pm 3/2\rangle$, $|0, \pm 1/2\rangle$ and $|\pm 1, \mp 1/2\rangle$ as

$$\psi_\pm^{(0)} = a_1|\mp 1, \pm 3/2\rangle + a_2|0, \pm 1/2\rangle + a_3|\pm 1, \mp 1/2\rangle. \tag{1.2}$$

Within the lowest Kramers doublet, we have

$$\langle\psi_{\pm}^{(0)}|S^z|\psi_{\pm}^{(0)}\rangle = \pm\frac{1}{2}(3a_1^2 + a_2^2 - a_3^2) = \pm\frac{1}{2}p, \tag{1.3}$$

$$\langle\psi_{\pm}^{(0)}|S^{\pm}|\psi_{\mp}^{(0)}\rangle = 2(\sqrt{3}a_1a_3 + a_2^2) = q. \tag{1.4}$$

Using these relations, we can replace the true spin $\boldsymbol{S}$ with $S=3/2$ by the spin-1/2 operator $\boldsymbol{s}$ given by

$$S^x = qs^x, \quad S^y = qs^y, \quad S^z = ps^z. \tag{1.5}$$

We assume that the exchange interaction between true spins $\boldsymbol{S}_i$ and $\boldsymbol{S}_j$ is described by the Heisenberg model $\mathcal{H}_{\text{ex}} = J\boldsymbol{S}_i \cdot \boldsymbol{S}_j$. Substituting eq. (1.5) into $\mathcal{H}_{\text{ex}}$, we obtain the effective model

$$\mathcal{H}_{\text{eff}} = J^{\perp}\left(s_i^x s_j^x + s_i^y s_j^y\right) + J^{\parallel} s_i^z s_j^z, \tag{1.6}$$

with

$$J^{\perp} = q^2 J, \quad J^{\parallel} = p^2 J. \tag{1.7}$$

In general, the effective exchange interaction between fictitious spins are largely anisotropic owing to the trigonal crystalline field. However, when the trigonal crystalline field is absent ($\delta = 0$), the effective exchange interaction $\mathcal{H}_{\text{eff}}$ becomes the Heisenberg model. Further details of the effective model of Co^{2+} in Ba_2CoTeO_6 will be described in the Appendix.

1.3 Quantum Spin Systems

We consider a spin model with the uniaxial symmetry. The Hamiltonian can be represented by the so-called XXZ model as follows:

$$\mathcal{H} = \sum_{i,j}\{J_{\perp}(S_i^x S_j^x + S_i^y S_j^y) + J_{\parallel} S_i^z S_j^z\} \tag{1.8}$$

where $\boldsymbol{S_i}$ represents spin of a magnetic ion i. $J_{\parallel}$ and $J_{\perp}$ denotes the z and xy components of the exchange constant. Extreme cases $J_{\perp}$ and $J_{\parallel} = 0$ are called Ising model and XY model, respectively, and the case of $J_{\parallel} = J_{\perp}$ is called Heisenberg model.

1.4 Geometrical Frustration in Magnet

Frustrated magnets has been attracting considerable attention from the viewpoint of remarkable quantum and many body effects which offer spin liquid and quantization of magnetization [25–27]. As we mentioned before, magnetic frustration can lead to the degenerate classical ground states. First of all, it is necessary to describe what is the frustration and how important it is. We consider Ising model with antiferromagnetic exchange interaction between spins. Since Ising spin has only one degree of freedom, it can point only up or down directions. Supposing a square with spins placed on the their corners as shown in Fig. 1.2(a), it is possible to have a spin state that satisfy the requirement of all exchange interaction, i.e., the spin state in which two spins point up and the other two point down can minimize all the exchange energies. This is the case of antiferromagnetic Ising model on a hexagon as shown in Fig. 1.2(b). It can be said that frustration does not occur in this system. However, if we consider a triangle with three spins placed on the three corners as Fig. 1.2(c), the situation is different. We assume that one spin points up, and one spin points down. The problem is that the last spin can not decide whether pointing up or down because both states have the same energy. Thus, the ground state is doubly degenerate. This kind of situation is called geometrical frustration, in which magnetic frustration is caused by innate geometry of the magnetic lattice.

Next, we consider the antiferromagnetic classical Heisenberg model on a triangle. In this model, the spin structure with minimum energy is the 120° structure as shown in Fig. 1.3. In Fig. 1.3(a), we show two types of the 120° structures. In case we go round the triangle counterclockwise, all three spins will rotate counterclockwise by 120°. We call this type of spin as the left-handedness. On the other hand, for the spin structure shown in Fig. 1.3(b), if we go round the triangle counterclockwise, spins will rotate clockwise (right-handedness). We can declare that two types of 120° structure have chiral symmetry. We define the left-handedness as positive chirality and the right-handedness as negative chirality. Since the classical Heisenberg spins in triangular lattice

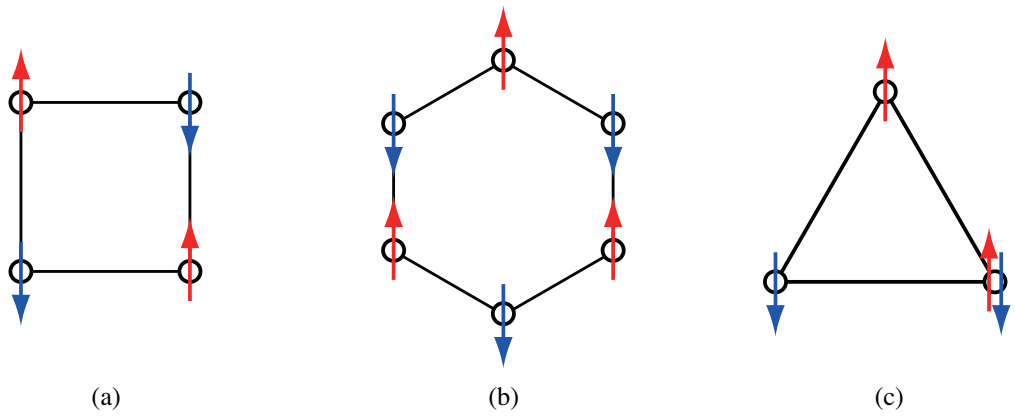

Figure 1.2: Antiferromagnetic Ising models on the corners of (a) square, (b) hexagon and (c) triangle. In (a) and (b), the requirement of all exchange interactions are satisfied, while in (c) the requirement of one of three exchange interactions is not satisfied, whether the third spin points up or down. This situation is called geometrical frustration.

have the chiral symmetry, the ground state is doubly degenerate.

The triangular lattice is composed of edge-sharing triangles as shown in Fig. 1.4. The classical ground state of the Heisenberg model on the triangular lattice is the 120° structure as shown in Fig. 1.4. In this case, the chirality of spins of neighboring triangles can be uniquely determined, as shown in Fig. 1.4. Thus, if we specify the chirality for one triangle, then the chiralities for the other triangles are automatically determined. Therefore, the classical ground state of the Heisenberg model on the triangular lattice is doubly degenerate.

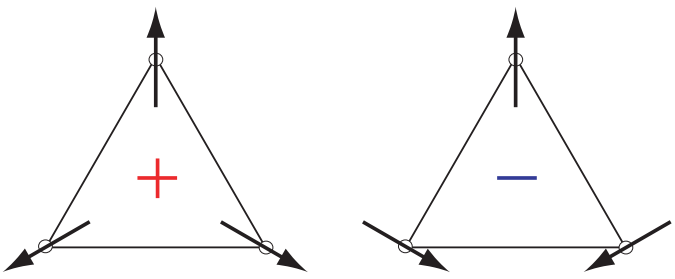

Figure 1.3: Two types of 120° structures of classical Heisenberg model on triangles with positive and negative chirality.

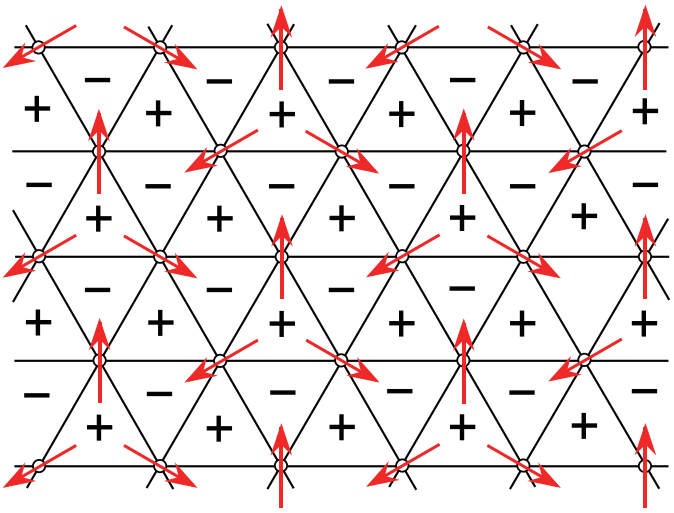

Figure 1.4: Classical ground state of the Heisenberg model on the triangular lattice, where spins formthe 120° structure. Symbols "+" and "−" denote the chirality of the spin structure of each triangle.

In the case of $S = 1/2$, quantum effect becomes maximal, so that the quantum fluctuation may destroy the classical ground state with the 120° spin structure. In 1973, Anderson predicted a resonating-valence-bond (RVB) spin liquid state without a long-range magnetic ordering as the ground state of $S = 1/2$ Heisenberg model on the triangular lattice [28]. The RVB state is described by the linear superposition of various configurations composed of singlet dimers, where translational symmetry is not broken [28, 29]. Motivated by the fascinating RVB state, great effort has been made to elucidate the nature of their ground state. The theoretical consensus at present is that the ground state is an ordered state with the 120° [30–33]. Although the ground state is similar to that of the classical model, the magnitude sublattice spin $\langle S \rangle$ is significantly reduced to be $\langle S \rangle = 0.205$ owing to the quantum fluctuation [34].

1.5 Quantum Order-by-Disorder

In quantum physics, the quantum fluctuation is the temporary change of the energy at one point in space. In many-spin systems [3, 4, 25], if we can determine the ordered state in a classical way, where spins are treated as classical vectors, the ground state can

always be identified. This classically determined ground state is called classical ground state. In the system without spin frustration, the benefit of quantum fluctuation is just the correction of the classical ground state. The magnitude of quantum fluctuation is considered to be minute compared to the classical one so that it does not have the ability to destabilize the classical ground state. This situation is illustrated in Fig. 1.5(a).

However, for frustrated systems, the classical ground state is often degenerate or there are many states that have almost the same classical energy. In such case, the classical ground state is unable to be uniquely determined. Since the energy of the quantum fluctuation varies depending on the characteristics of spin state, the energy of each degenerate classical basis becomes different. Owing to the quantum fluctuation, the specific spin state is stabilized uniquely as the ground state. Figure 1.5 illustrates the degenerate classical ground state energies and the quantum fluctuation energies depending on spin states. This mechanism to select the ground state with the help of quantum fluctuation is called "quantum order-by-disorder". The quantum order-by-disorder will play an important role in determining the magnetic ground states in both zero field and field-driven cases. This quantum effect becomes maximal for the $S = 1/2$ case. Thus, we can expect remarkable quantum effect in Ba_2CoTeO_6 at low temperatures.

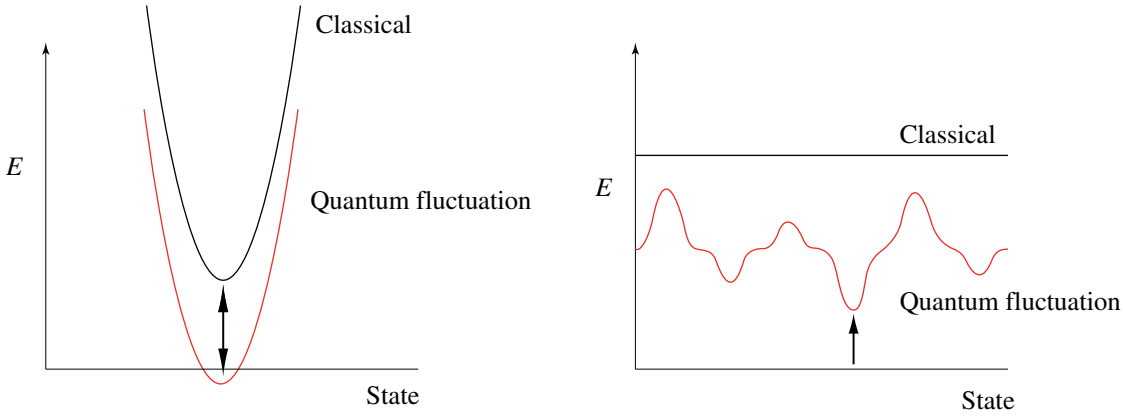

Figure 1.5: Effect of quantum fluctuation in (a) nonfrustrated system and (b) frustrated system. For nonfrustrated system. quantum fluctuation only corrects the classical ground state, while in frustrated system with degenerate classical ground states, a specific spin state with the lowest quantum fluctuation energy is selected as the ground state.

1.6 $S = 1/2$ Heisenberg Triangular Lattice Antiferromagnet (TLAF)

Recently, geometrically frustrated antiferromagnets have been attracting considerable attention from the viewpoint of exotic ground states and interesting quantum phenomena. One of the simplest models is a Heisenberg triangular lattice antiferromagnet (TLAF) [27, 29, 35]. Triangular lattice is a two-dimensional lattice, which is composed of edge-sharing triangles.

In the classical Heisenberg TLAF, the ground state is the 120° as shown in Fig. 1.4. The spin structure is composed of three sublattices labeled as $i = 1, 2$ and 3. We write three sublattice spins as $\boldsymbol{S}_1$, $\boldsymbol{S}_2$ and $\boldsymbol{S}_3$. The equilibrium condition of the sublattice spins in a magnetic field $\boldsymbol{H}$ can be written as

$$\boldsymbol{S}_1 + \boldsymbol{S}_2 + \boldsymbol{S}_3 = \frac{g\mu_{\mathrm{B}}\boldsymbol{H}}{3J}. \tag{1.9}$$

In order to determine the configuration of one sublattice spin, we need two parameters. Therefore, in general, we need six parameters to determine the configuration of three sublattice spins. However, the number of parameters can be reduced to five, because the

global rotation around the magnetic field is trivial. On the other hand, number of equations describing the equilibrium condition is three, i. e. three components of Eq. (1.9). Since the number of equations is smaller than the number of parameters necessary to determine the spin configuration, the classical ground state cannot be uniquely determined. Consequently, the ground state of classical Heisenberg TLAF in the magnetic field is infinitely degenerate.

For the quantum spin case, the zero-field ground state is the ordered state with the 120°, even in the case of $S = 1/2$. Although the zero-field ground state is the same as that of the classical model [30–34], marked macroscopic quantum effect takes place in the magnetic field [3–11, 36]. This because the classical degeneracy mentioned above can be lifted by quantum fluctuation, and a specific spin state is selected as the ground state. The degeneracy lifting mechanism is called quantum order-by-disorder as mentioned before.

Spin wave analysis [3, 4], coupled cluster method [6], exact diagonalization [5, 7], grand canonical numerical analysis [8] and cluster mean-field theory [9] were used to calculate magnetization process of $S = 1/2$ Heisenberg TLAF. These theory demonstrated that the "up-up-down" (uud) state is stabilized by the quantum fluctuation in a finite field range, so that the magnetization exhibits a plateau at one-third of the saturation magnetization M_s. Figure 1.6 shows the magnetization curve calculated using the coupled cluster method and exact diagonalization [6]. The calculated magnetization curve is in striking contrast with the classical magnetization curve, which increases linearly with increasing magnetic field obeying Eq. (1.9) and saturates. The classical magnetization curve displays no anomaly up to the saturation. Figure 1.7 shows the representative spin structures expected in magnetic fields. At low magnetic fields below the lower edge field of the 1/3-plateau state, the quantum fluctuation stabilizes the low-field coplanar structure shown in Fig. 1.7(a). At high magnetic fields above the higher edge field of the 1/3-plateau state, another coplanar structure shown in Fig. 1.7(d) is stabilized up to the saturation. High symmetric umbrella structure shown in Fig. 1.7(b) is unstable over all

field range.

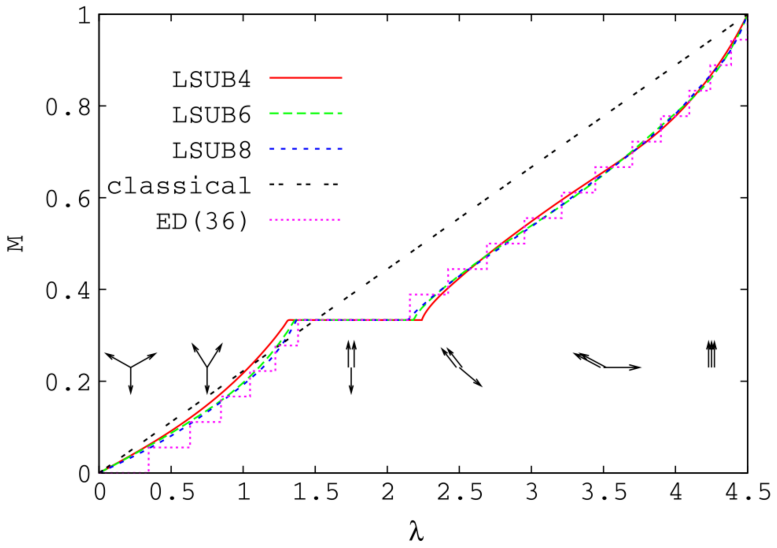

Figure 1.6: Theoretical magnetization curves calculated using coupled cluster method (CCM) and exact diagonalization (ED), compared with classical magnetization curve [6].

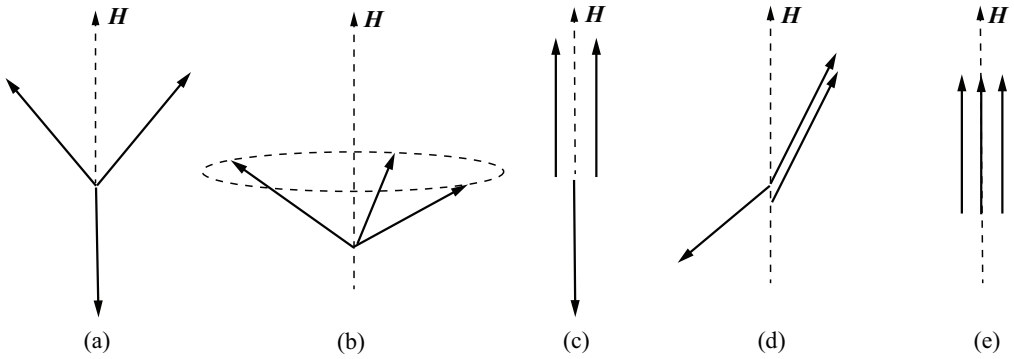

Figure 1.7: Representative spin structures of $S = 1/2$ Heisenberg TLAF under applied magnetic field. (a) coplanar I structure, (b) umbrella structure, (c) up-up-down (uud) structure, (d) coplanar II structure, and (e) saturated structure.

As show above, it was demonstrated theoretically that the quantum fluctuation produces the macroscopic quantum phenomenon, 1/3-magnetization plateau, in magnetic fields. In order to verify the quantum magnetization process predicted by theory, great experimental effort has been made to search model substances of $S = 1/2$ Heisenberg

TLAFs. However, model substances that exhibit the 1/3-magnetization plateau are handful. Only Cs_2CuBr_4 [37, 38] and $Ba_3CoSb_2O_9$ [14, 16] are known to display clear 1/3-magnetization plateau.

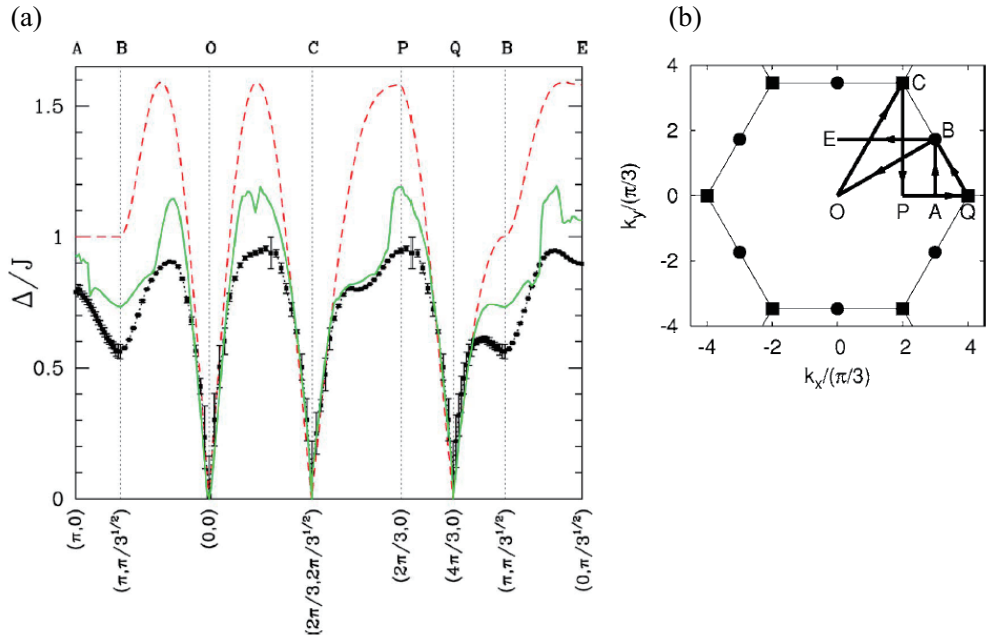

Figure 1.8: (a) Dispersion curves of single magnon excitations calculated by the series expansion approach [40]. Red dashed and green lines are the dispersion curves calculated by linear spin wave theory and spin wave theory with $1/S$ correction. (b) Two-dimensional reciprocal lattice of TLAF, where Q and C, and B correspond to the K and M points, respectively. Reprinted from Ref. [40].

Magnetic excitations of $S = 1/2$ Heisenberg TLAFs have been theoretically investigated [39–44]. In contrast to the ground state properties, theoretical consensus is limited only to the single magnon excitations. Figure 1.8 shows the dispersion relations of single magnon excitations calculated by the series expansion approach [40]. The dispersion relation of low-energy single magnon excitations near the magnetic Bragg point (K point) is described by linear spin wave theory. However, in a large area of the Brillouin zone, the excitation energy is significantly renormalized downward by quantum fluctuations, causing the dispersion curve to become flat. In addition, series expansion approach [40, 44] has demonstrated that the dispersion curve shows a rotonlike minimum

at the M point, and nonlinear spin wave theory [41, 43] has shown that spontaneous decays of magnons occur owing to the magnon interaction, which leads to line broadening of the excitation spectrum. For the excitation continuum, however, there is no theoretical consensus.

1.7 Previous Studies on $S = 1/2$ Heisenberg TLAF Spin System

1.7.1 $CsCuCl_3$

The quantum-fluctuation-assisted phase transition in a magnetic field was first reported on TLAF $CsCuCl_3$ [4, 45, 46]. Crystal structure of $CsCuCl_3$ is hexagonal with Cu^{2+} as a magnetic ion. For this compound, triangular lattice forms in the ab plane. Exchange interaction between Cu^{2+} ions with $S = 1/2$ in a triangular lattice plane is antiferromagnetic, but exchange interaction along c-axis is ferromagnetic. Magnetic phase transition occurs at T_N= 10.5 K [47]. Below T_N, spins form the 120° structure in the ab plane and a helical structure along c axis, as shown in Fig. 1.9. Because of the low-symmetric crystal structure the Dzyaloshinsky-Moriya (DM) interaction between neighboring spin along the c axis is allowed. This helical structure can be explained by competition between the ferromagnetic exchange interaction and the DM interaction along the c axis [47, 48].

When magnetic field is applied parallel and perpendicular to the c axis, a small jump anomaly and a plateau-like anomaly at around 1/3 of the saturation magnetization were observed in the magnetization curves, respectively, as shown in Fig. 1.10 [4, 46]. However, unlike the theoretical result of Heisenberg triangular lattice antiferromagnet mentioned above, the observed magnetization plateau of $CsCuCl_3$ is narrow and not completely flat [4]. $CsCuCl_3$ has the anisotropy of the easy-plane type due to the DM interaction and anisotropic exchange interaction [48]. Nikuni and Shiba [4] demonstrated that the discontinuous transition for $H \parallel c$ is the transition from the umbrella structure stabilized by the easy-plane anisotropy to the coplanar II structure driven by the quantum fluctuation.

Very recently, Sera *et al.* [49] reported that $CsCuCl_3$ exhibits the 1/3-magnetization

plateau for $H \parallel c$ in hydrostatic pressures above 0.68 GPa.

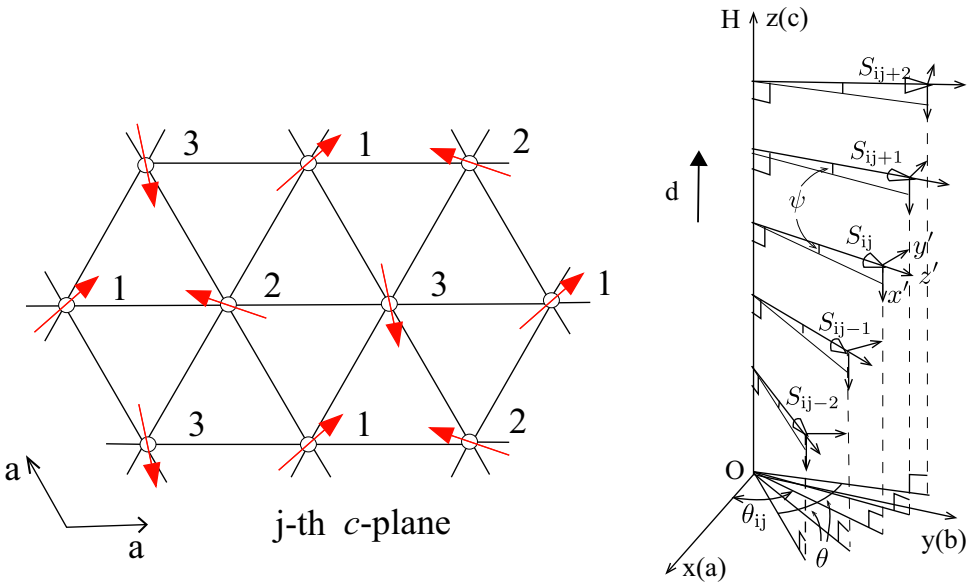

Figure 1.9: (a) The 120° spin structure in the ab plane of $CsCuCl_3$ observed below $T_N = 10.5$ K. (b) Helical structure caused by competition between the ferromagnetic exchange interaction and the Dzyaloshinsky-Moriya (DM) interaction in c axis. Reprinted from Ref. [48].

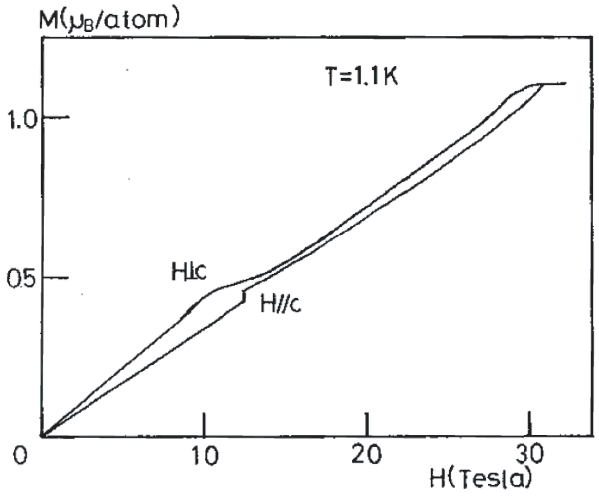

Figure 1.10: Magnetization processes of $CsCuCl_3$ measured at 1.1 K [46].

1.7.2 Cs_2CuBr_4

Cs_2CuBr_4 was first reported to exhibit a clear 1/3-magnetization plateau [37, 38, 50]. Magnetic ions Cu^{2+} having S=1/2 are located at the center of the tetrahedra $CuBr_4$ and form a distorted triangular lattice in the bc plane, as shown in Fig. 1.11. Because of the distortion of lattice, there are two kinds of exchange interaction J_1 and J_2. The magnetic phase transition occurs at $T_N = 1.4$ K [37, 50]. The order phase below T_N has an incommensurate spin structure cause by the inequivalence of J_1 and J_2 [38]. When a magnetic field is applied parallel to the b and c axis, a magnetization plateau is observed at approximately one-third of the saturation magnetization M_s, as shown in Fig. 1.12. It was found from neutron diffraction experiment that the uud spin structure is actually realized at the plateau state [38]. In Cs_2CuBr_4, narrow magnetization plateau was also observed near two-third of M_s [38, 50].

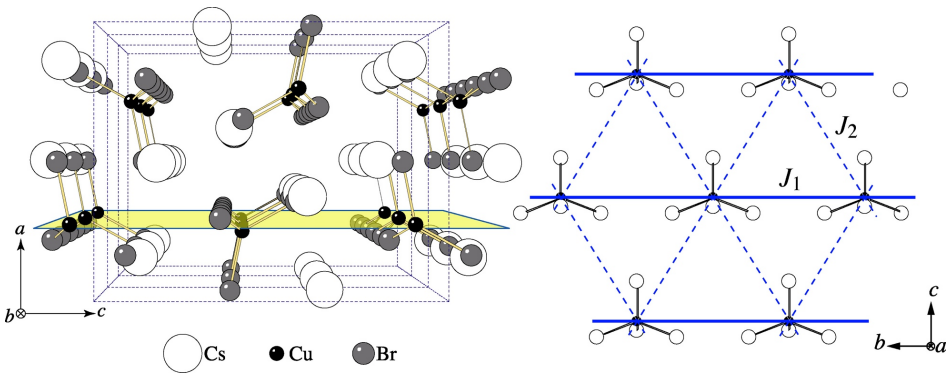

Figure 1.11: (a) Crystal structure of Cs_2CuBr_4, where the yellow plane denotes triangular lattice parallel to the bc plane. (b) Triangular lattice on the bc plane. Since the triangular lattice is not uniform, there are two kinds of exchange interaction J_1 and J_2. Reprinted from Ref. [37].

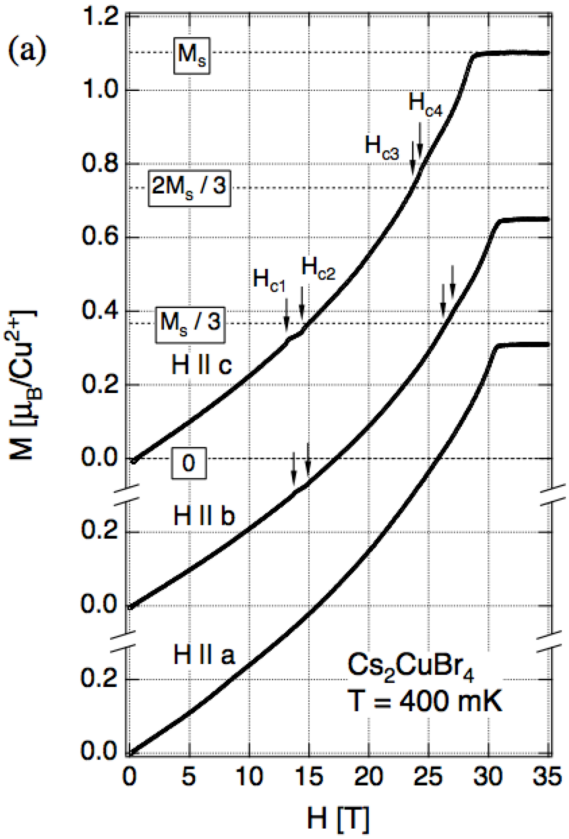

Figure 1.12: Magnetization curves measured at 0.4 K for $H \parallel a$, $H \parallel b$, and $H \parallel c$. H_{c1} and H_{c2} indicate the edge fields of $M_s/3$ plateaus for $H \parallel b$, and $H \parallel c$. For these field directions, narrow magnetization plateau is also observed between H_{c3} and H_{c4}. Reprinted from Ref. [38].

1.7.3 $Ba_3CoSb_2O_9$

$Ba_3CoSb_2O_9$ has a hexagonal perovskite structure similar to that in Ba_2CoTeO_6. In $Ba_3CoSb_2O_9$, the layers of CoO_6 octahedra are separated by a layer of Sb_2O_9 double octahedra. $Ba_3CoSb_2O_9$ has a uniform triangular lattice of Co^{2+} parallel to the *ab* plane [24]. and Co^{2+} is the magnetic ion where antiferromagnetic exchange interaction happens between each magnetic ion. $Ba_3CoSb_2O_9$ undergoes the magnetic phase transition at $T_N = 3.8$ K. In the ordered phase, spins form the 120° structure in the triangular layer and the antiferromagnet arrangement along the *c* axis [24]. When a magnetic field was applied parallel to the *ab* plane, a clear magnetization plateau was observed at 1/3 of saturation magnetization [14, 16] (see Figs. 1.13 and 1.14). The experimental magnetiza-

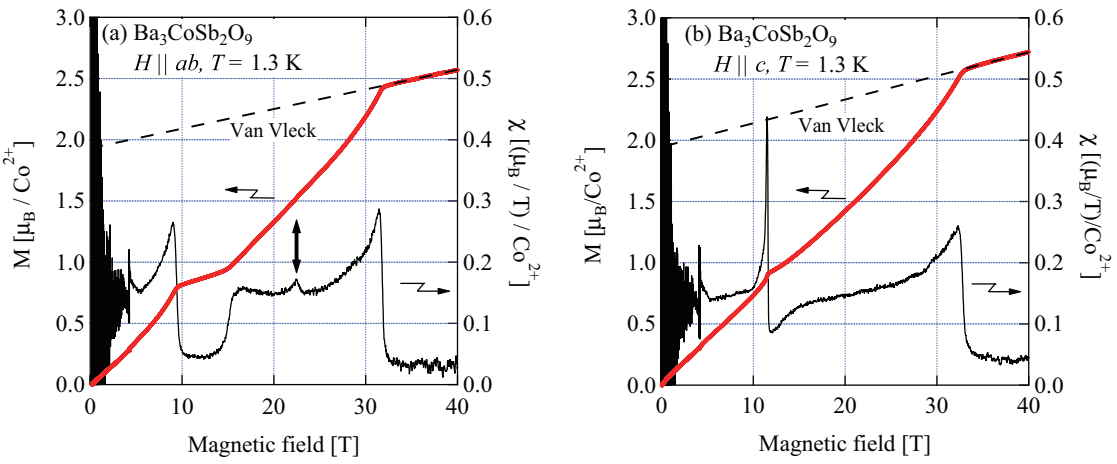

Figure 1.13: (Color online) Magnetization curves and its field derivative in $Ba_3CoSb_2O_9$ single crystals, measured at 1.3 K for (a) $H \parallel ab$ and (b) $H \parallel c$. Dashed lines denote the magnetization owing to the Van Vleck paramagnetism, which are linear in magnetic field H. Reprinted from Ref. [16].

tion curve for powder sample is in perfect agreement with theoretical calculations using the coupled cluster method (CCM) and exact diagonalization (ED) [14]. It was found from the high-field magnetization measurements that the exchange interaction between effective spins with $S = 1/2$ are close to the Heisenberg model. This indicates that the crystalline field acting on Co^{2+} is close to cubic field. In addition, small magnetization anomaly at $\frac{3}{5}M_s$ indicative of a new high-field phase was observed. However, in the case of applying a magnetic field parallel to the c axis, magnetization curve exhibits a cusp near one-third of saturation magnetization due to small anisotropic exchange interaction of the easy-plane type [16]. From the saturation field of $H_s \approx 32.5$ T and g factor of $g \approx 3.85$, the intralayer exchange interaction was estimated as $J/k_B = 18.5$ K. The whole of the magnetization process of $Ba_3CoSb_2O_9$ was theoretically explained from the microscopic model [9, 18].

The magnetic phase diagram was investigated via specific heat [15] and ultrasound velocity [17] measurements. Figure 1.15 shows the phase diagrams for $H \parallel c$ and $H \perp c$ obtained via ultrasound velocity measurements [17]. The feature of the phase diagram for $H \perp c$ is that the "uud" phase sticks out in the paramagnetic phase. For $H \parallel c$,

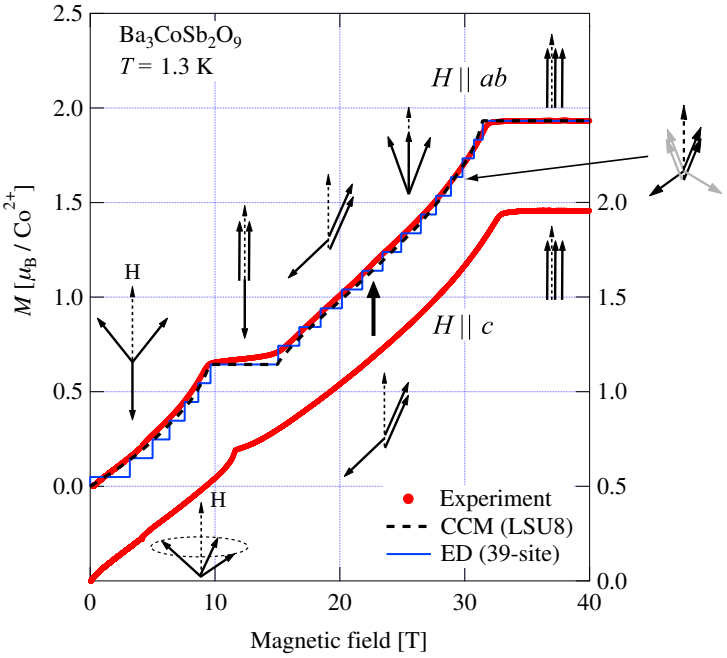

Figure 1.14: Magnetization curves of $Ba_3CoSb_2O_9$ for $H \parallel ab$ (up) and $H \parallel c$ (down) after the subtraction of the Van Vleck paramagnetism that is linear in magnetic field H. The dashed curve and the steplike solid line indicate the theoretical results calculated by a coupled cluster method (CCM) and exact diagonalization (ED). Reprinted from Ref. [16].

the transition field between the umbrella and high-field coplanar phases is independent of temperature. According to the Clausius-Clapeyron equation, this indicates that the field-induced phase transition arises not from the entropy gain but from energy gain. Namely, the transition is originated from the quantum fluctuation.

Below T_N, two collective ESR modes were observed as shown in Fig. 1.16. Using a six-sublattice model with easy-plane anisotropy, the interlayer exchange and anisotropic exchange constant were estimated as $J'/k_B = 1.40$ K and $\Delta J/k_B = 0.898$ K, respectively [16], where ΔJ is defined as $\Delta J = J^{\perp} - J^{\parallel}$. Since anisotropic exchange interaction is much smaller than the intralayer exchange interaction J, It was proved that $Ba_3CoSb_2O_9$ approximates the $S = 1/2$ Heisenberg TLAF. At present, $Ba_3CoSb_2O_9$ is the best realization of $S = 1/2$ Heisenberg TLAF.

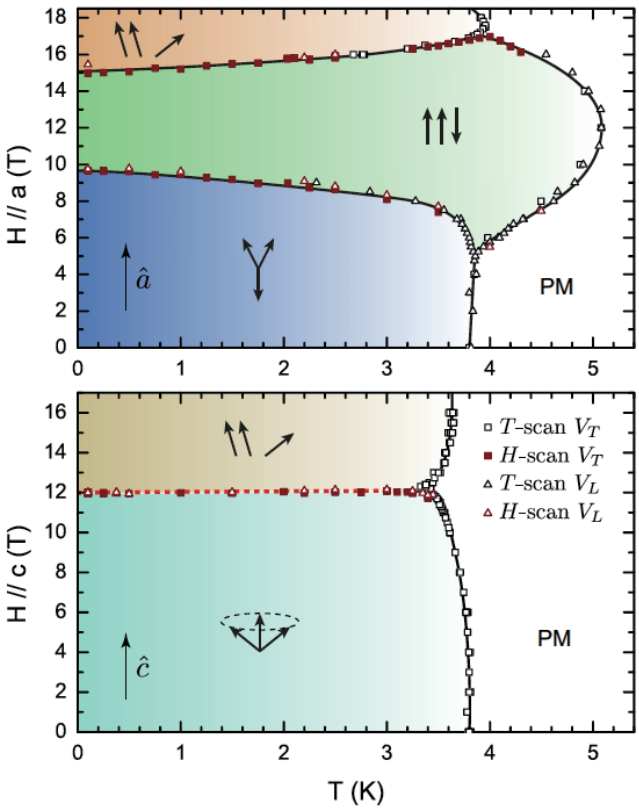

Figure 1.15: The magnetic phase diagrams in $Ba_3CoSb_2O_9$ obtained for $H \parallel c$ and $H \perp c$ via ultrasound velocity measurements. Reprinted from Ref. [17].

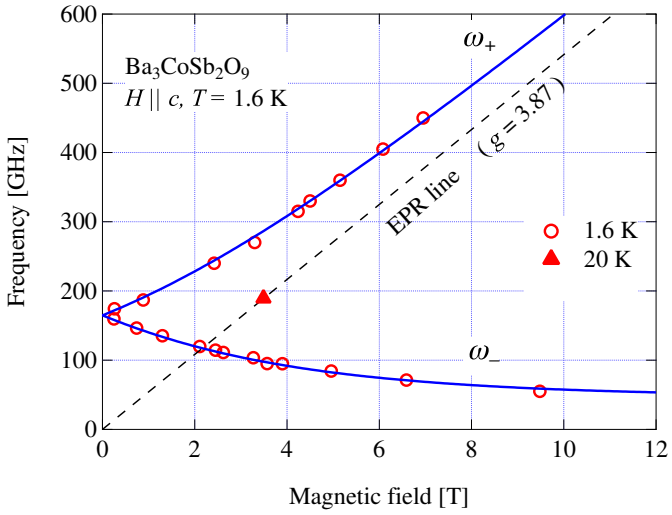

Figure 1.16: Frequency-field diagram of the collective ESR modes observed in $Ba_3CoSb_2O_9$ for $H \parallel c$. Red open marks represent the resonance points at 1.6 K. The solid curve is the result calculated using a six sublattice model. The dashed line is the EPR line. Reprinted from Ref. [16].

Magnetic excitations in $Ba_3CoSb_2O_9$ were also investigated via inelastic neutron scattering experiments [19, 51]. Ma *et al.* [19] observed renormalized flat dispersion, which was predicted by theory [39–44]. Ito *et al.* [51] observed three-stage energy structure of excitation spectra as shown in Fig. 1.17. The lowest stage is composed of two distinct branches of single-magnon excitations, which rise up from the K point. The second and third stages are dispersive excitation continua. A rotonlike minimum, which was predicted by theory [40, 44], was clearly observed at the M point.

A remarkable feature of magnetic excitations in $Ba_3CoSb_2O_9$ is two strong dispersive excitation continua, in which the higher energy excitation continuum extends to over the energy of six times larger than the exchange interaction $J = 1.67$ meV. Because $Ba_3CoSb_2O_9$ is approximately described by $S = 1/2$ Heisenberg TLAF, it is considered that the observed excitation spectra are close to the true excitation spectra of $S = 1/2$ Heisenberg TLAF. At present, no theory describes the structure of the excitation continua observed in this experiment, and thus, a new theoretical framework is required.

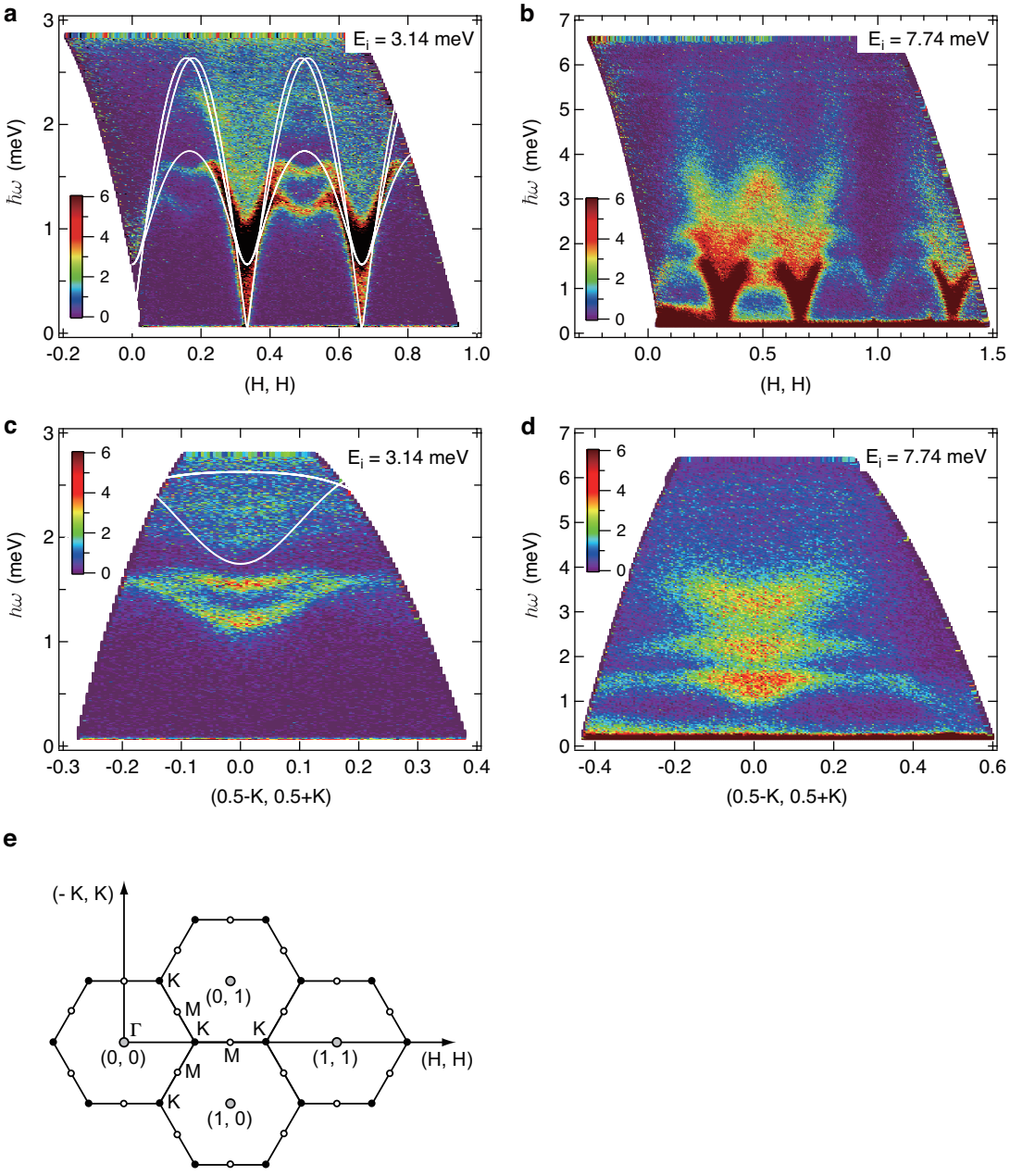

Figure 1.17: Excitation spectra of $Ba_3CoSb_2O_9$ measured at $T = 1.0$ K. **a-d** Energy-momentum maps of the scattering intensity along two high-symmetry directions parallel to $\boldsymbol{Q} = (H, H)$ and $(-K, K)$ measured with incident neutron energies of $E_i = 3.14$ and 7.74 meV, where the scattering intensities were integrated over L. The solid lines in a are dispersion curves calculated by linear spin wave theory with $J = 1.67$ meV and $\Delta J/J = 0.046$ on the basis of the 2D model. **e** 2D reciprocal lattice. Reprinted from manuscript of Ref. [51].

1.8 Bond Frustration in Magnet

As mentioned in subsection 1.4, spin frustration is absent in the antiferromagnetic Ising model on the corners of square and hexagon. However, when the next-nearest-neighbor exchange interaction is switched on, spin frustration takes place owing to the competition of nearest-neighbor J_1 and next-nearest-neighbor J_2 exchange interactions. The spin configurations in Figs. 1.18(a) and (b) satisfy the requirement of J_1 interaction but do not satisfy the requirement of J_2. This frustrated situation is called "bond frustration".

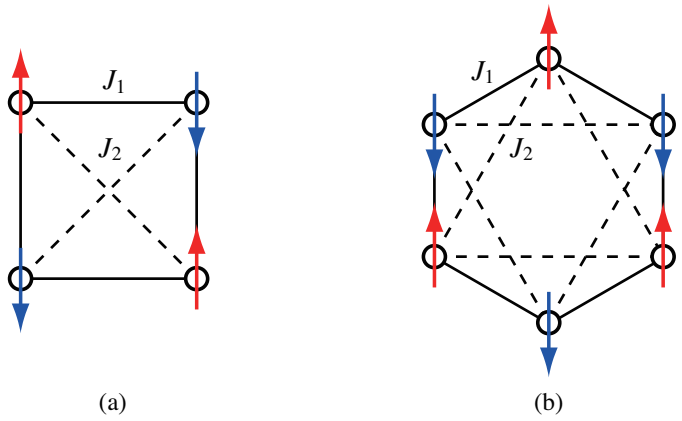

Figure 1.18: Illustration of the bond frustration. Antiferromagnetic J_1-J_2 Ising model on the corners of (a) square and (b) hexagon, where solid and dashed lines are the nearest-neighbor J_1 and next-nearest-neighbor J_2 exchange interactions, respectively.

Rastelli *et al.* [52] and Fouet *et al.* [53] investigated the J_1-J_2-J_3 classical Heisenberg model on the honeycomb lattice, which takes the third-nearest-neighbor exchange interaction into account. Figure 1.19(a) shows the ground state phase diagram of this model. There are four collinear phases (I, II, IV and VI) and two spiral phases (III and V). In the case of $J_3 = 0$, an antiferromagnetic phase (I) changes into a spiral phase at $J_2/J_1 = 1/6$ with increasing J_2/J_1. Ganesh*et al.* [23] investigated the quantum effect on the ground state for an $S = 1/2$ J_1-J_2 Heisenberg honeycomb lattice antiferromagnet. They demonstrated that nonmagnetic plaquette resonating-valence-bond state and dimer state can emerge with increasing J_2/J_1, as shown in Fig. 1.19(b). The classical

spiral phase is superseded by quantum singlet phases. Thus, quantum fluctuation makes drastic change in the ground state.

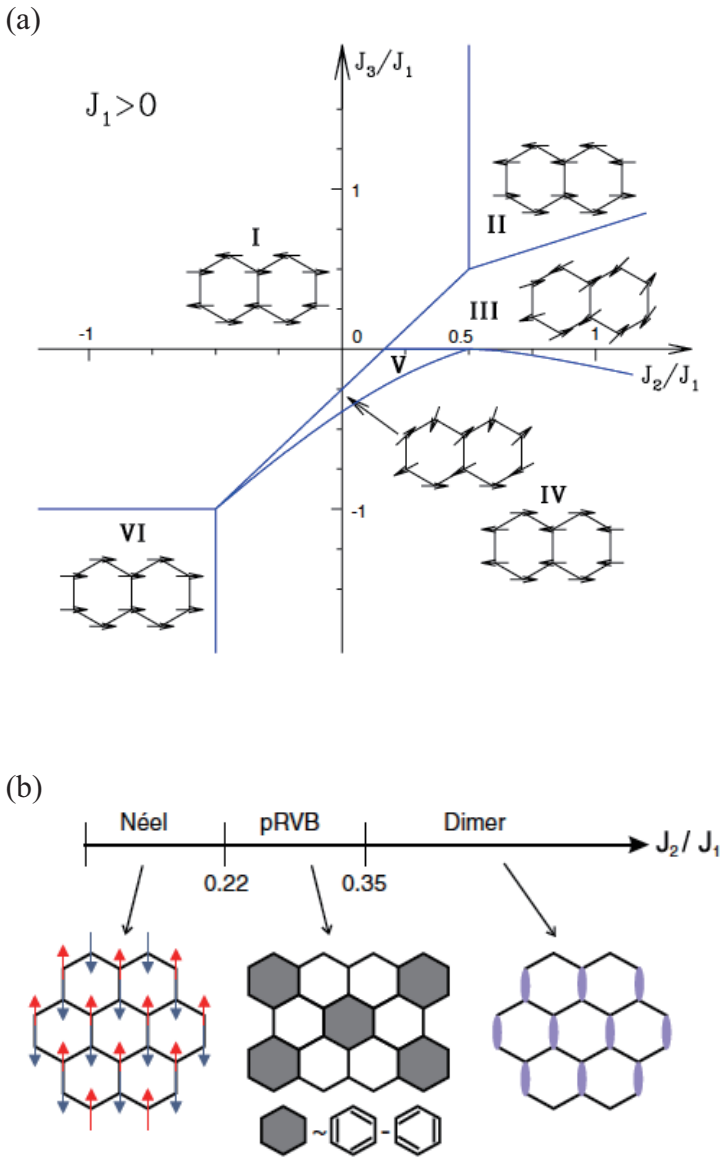

Figure 1.19: (a) The ground state phase diagram for the J_1-J_2-J_3 classical Heisenberg model on the honeycomb lattice with antiferromagnetic J_1 interaction. There are four collinear phases (I, II, IV and VI) and two spiral phases (III and V). Reprinted from Ref [53]. (b) Ground states of $S = 1/2$ $J_1 - J_2$ Heisenberg honeycomb lattice antiferromagnet, where the Néel, plaquette resonating-valence-bond state, and dimer state can emerge with increasing J_2/J_1. Reprinted from Ref. [23].

1.9 Frustrated Ising Model in Magnetic Fields

Although the quantum effect is absent in the Ising model, bond frustration owing to the competition of exchange interactions can lead unusual successive metamagnetic phase transitions in magnetic fields as observed in $CoCl_2 \cdot 2H_2O$ [54] (see Fig. 1.20). The Ising model in longitudinal magnetic field is expressed as

$$\mathcal{H} = \sum_{i,j} J_{ij} S_i^z S_j^z - g\mu_B H S_i^z. \tag{1.10}$$

Kanamori developed general theory to obtain exact ground state in magnetic field for given model without assuming sublattices [55]. He successfully explained the successive metamagnetic transitions observed in $CoCl_2 \cdot 2H_2O$ assuming competing exchange interactions, which are reasonable from the crystal structure. However, for antiferromagnetic J_1-J_2 Ising model on a honeycomb lattice, which is realized in Ba_2CoTeO_6, the ground states in magnetic fields have not been investigated theoretically.

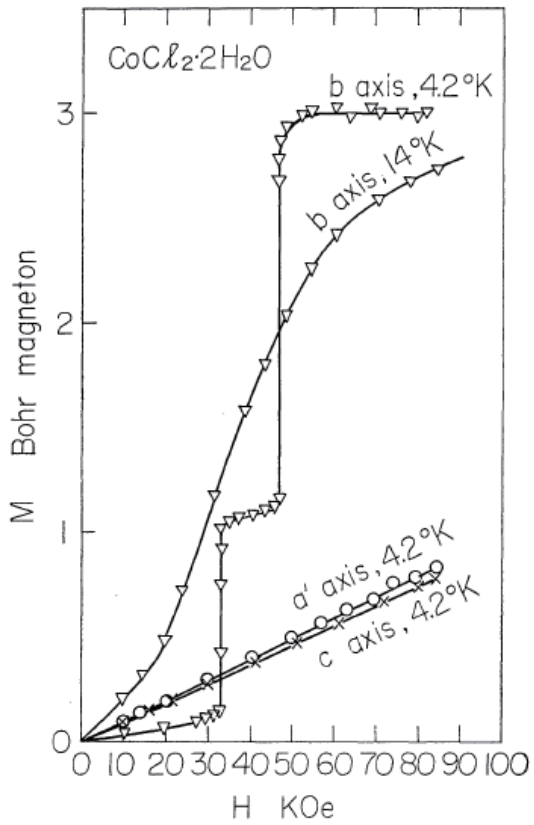

Figure 1.20: Magnetization process observed in $CoCl_2 \cdot H_2O$. For $H \parallel b$, magnetization shows stepwise change with a plateau at one-third of the saturation magnetization. Reprinted from Ref. [54].

1.10 Previous Study on Ba_2CoTeO_6

Ba_2CoTeO_6, which is the subject of this dissertation, is a hexagonal perovskite type compound [56] similar to $Ba_3CoSb_2O_9$ [24] and $Ba_3CoNb_2O_9$ [57], in which Co^{2+} ions have effective $S = 1/2$. In Fig. 1.21, we compare their crystal structures.

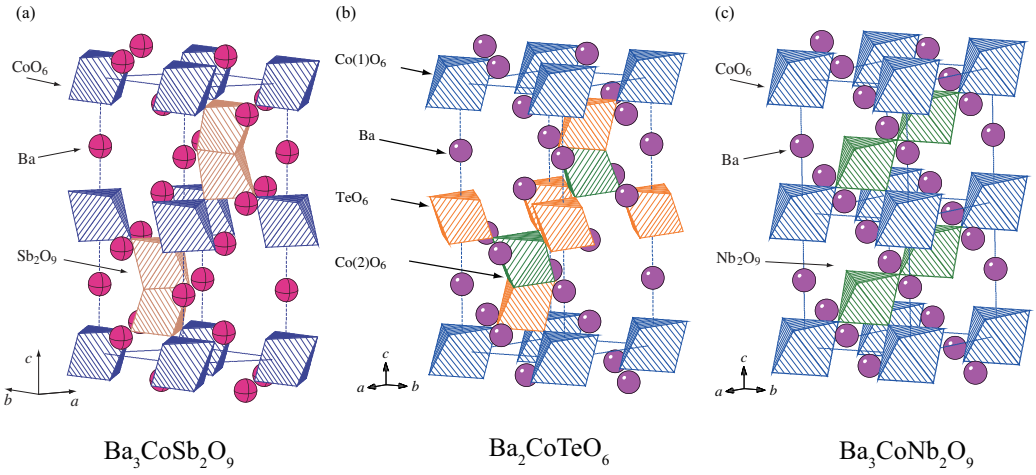

Figure 1.21: Comparison of crystal structures of three compounds with hexagonal perovskite structures (a)$Ba_3CoSb_2O_9$ [24], (b)Ba_2CoTeO_6 [56] and (c)$Ba_3CoNb_2O_9$ [57].

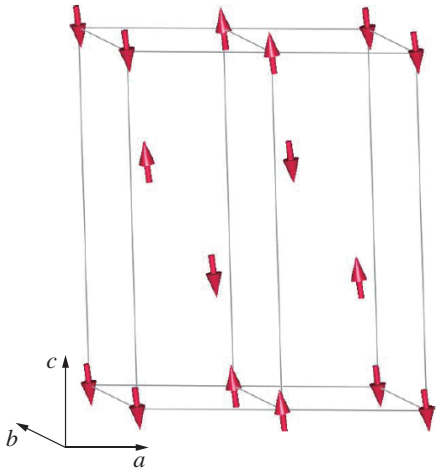

Figure 1.22: Magnetic structure of Ba_2CoTeO_6 at $T = 5$ K reported by Ivanov *et al.* [56].

Ivanov *et al.* [56] performed magnetic susceptibility and specific heat measurements on powdered sample of Ba_2CoTeO_6. They observed a sharp specific heat anomaly at around $T_N = 12$ K indicative of magnetic ordering. They carried out neutron powder diffraction (NPD) experiment at $T = 5$ K. They observed that in the ordered phase below

T_{N}, the magnetic unit cell is enlarged to $2a \times a$ in the ab plane and that that all the spins are roughly parallel to the c axis with canting by an angle of 24.5°, as shown in Fig. 1.22.

1.11 Purpose of This Study

Figures 1.23(a) and (b) shows the crystal structure of Ba_2CoTeO_6 [56] and its magnetic model, which is expected from the crystal structure. In Ba_2CoTeO_6, there are two Co^{2+} sites, $Co^{2+}(1)$ and $Co^{2+}(2)$. Both $Co(1)O_6$ and $Co(2)O_6$ octahedra are linked by TeO_6 octahedra in the ab plane sharing their corners. $Co^{2+}(1)$ ions form a a triangular lattice parallel to the ab plane, which we call subsystem A, while $Co^{2+}(2)$ ions form a double-layered triangular lattice, as shown in Fig. 1.23(b), which we call subsystem B. The crystalline fields acting on $Co^{2+}(1)$ and $Co^{2+}(2)$ ions are different. Because the $Co(1)O_6$ octahedron is almost cubic, we can expect that subsystem A is described as an $S = 1/2$ Heisenberg-like TLAF as in the case of $Ba_3CoSb_2O_9$ [14, 16].

For subsystem B, the lattice point of one triangular layer shifts onto the center of the triangle of the other triangular layer. Thus, the double-layered triangular lattice of subsystem B can be regarded as a honeycomb lattice, when viewed along the c axis, as shown in Fig. 1.23(c). Because it is considered that dominant superexchange interactions arise via TeO_6 octahedra linked with $Co(2)O_6$ octahedra by sharing corners, as discussed in Refs. [57, 58], the interlayer exchange interaction J_1 and the nearest neighbor exchange interaction J_2 in the triangular lattice must be dominant. The shape of the $Co(2)O_6$ octahedron is non-centrosymmetric, because the triangular face shared with TeO_6 octahedron is smaller than the opposite face. $Co^{2+}(2)$ shifts opposite to the TeO_6 octahedron. Consequently, the trigonal crystalline field acting on $Co^{2+}(2)$ should be comparable to the spin-orbit coupling. In such case, the exchange interaction between effective spins of $Co^{2+}(2)$ ions is considered to be strongly anisotropic XXZ model [2] with Ising-like anisotropy. Therefore, we can expect that subsystem B can be described as a J_1-J_2 Ising-like honeycomb lattice antiferromagnet (HLAF), as shown in Fig. 1.23(c).

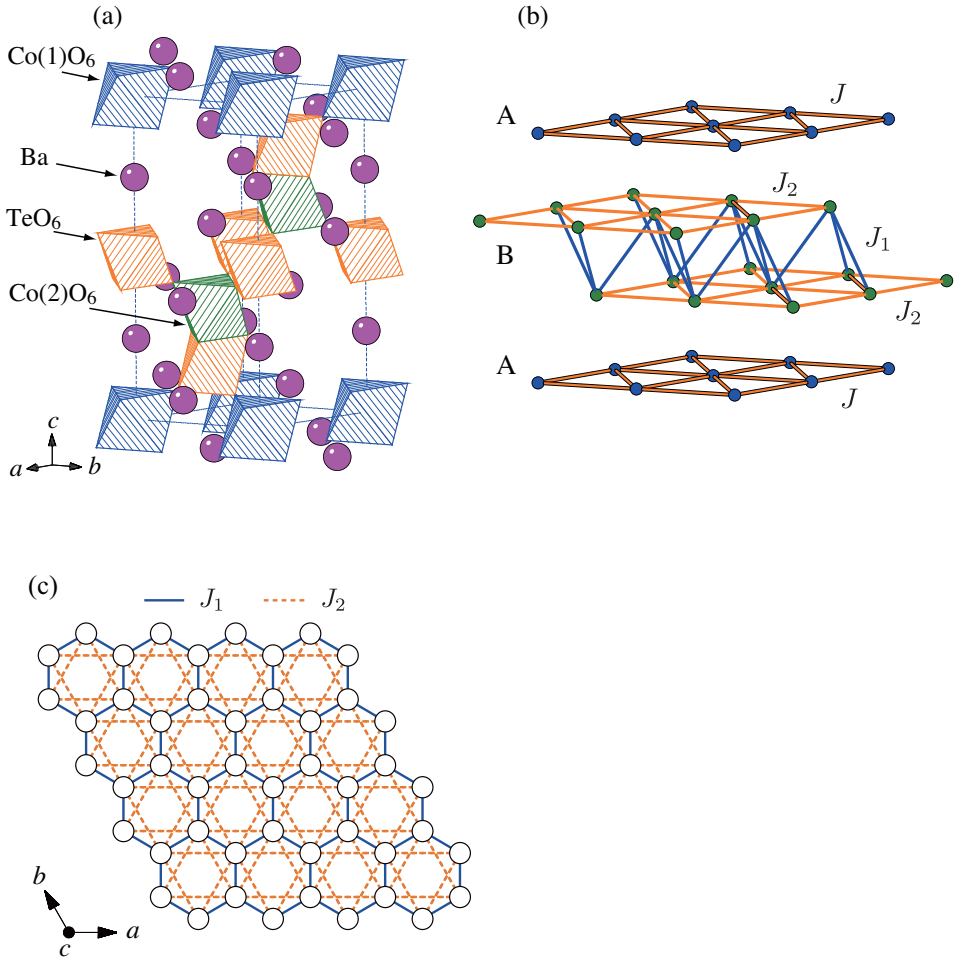

Figure 1.23: (a) Perspective view of the crystal structure of Ba_2CoTeO_6. $Co(1)O_6$, $Co(2)O_6$ and TeO_6 octahedra are indicated by blue, green and orange octahedra, respectively. (b) Magnetic model of Ba_2CoTeO_6 composed of two subsystems, A of triangular lattice and B of double-layered triangular lattice, which are consist of Co(1) and Co(2), respectively. (c) Effective magnetic model of subsystem B that is described as a J_1-J_2 Ising honeycomb lattice antiferromagnet.

$S=1/2$ Heisenberg TLAF and J_1-J_2 Ising HLAF are prototypical magnetic systems governed by geometrical and bond frustrations, respective. The model substances of $S=1/2$ Heisenberg TLAF exhibiting the 1/3-magnetization plateau are handful. As mentioned above, exotic magnetic excitation spectra were observed in $Ba_3CoSb_2O_9$ [51], which is considered to be the best realization of $S=1/2$ Heisenberg TLAF. It was re-

vealed that for magnetic excitations, there is significant difference between experiment and theory. In order to elucidate the nature of the magnetic excitations of $S = 1/2$ Heisenberg TLAF, other model substances with different magnetic parameters are needed. For J_1-J_2 Ising HLAF, we can expect multiple phase transitions in magnetic fields parallel to the Ising axis and quantum phase transition in transverse magnetic field. However, there is no model substance. Also, there is no theory on the ground states in magnetic fields. Thus, it is considered that many magnetic properties still remain to be elucidated on these two spin models. Since Ba_2CoTeO_6 includes both systems, its magnetic properties, in particular in magnetic fields, are of great interest from the viewpoint of quantum and many-body effects. The magnitude of coupling between subsystems A and B has not been clarified. This uniqueness of Ba_2CoTeO_6 motivates us to investigate its magnetic properties in details.

In previous work by Ivanov *et al.* [56], measurements were only performed on powdered sample, and the temperature range is limited to above 5 K. Thus, it is considered that its magnetic properties have not been sufficiently understood. In this doctoral dissertation, we synthesized high quality Ba_2CoTeO_6 single crystals and performed magnetic susceptibility, high-field magnetization and specific heat measurements in addition to multifrequency electron spin resonance (ESR) measurements. As shown below, we observed the second phase transition at $T_{N2} = 3.0$ K, which can interpreted as the ordering temperature of subsystem A. We found that the total magnetization is given by the superposition of individual magnetizations of subsystems A and B. This indicates that these two subsystems are almost decoupled. We observed three-step metamagnetic transitions in magnetic fields for $H \parallel c$, which is originated from Ising-like subsystem B. This unusual magnetization process can be successfully described within the J_1-J_2 Ising HLAF on the basis of Kanamori theory [55]. For $H \perp c$, magnetization curve exhibits the 1/3-plateau, which originated from subsystem A described as the $S = 1/2$ Heisenberg TLAF. For $H \parallel c$, we observed collective ESR modes characteristic of the Heisenberg TLAF with the small easy-plane anisotropy and a local excitation mode, which can be

assigned as the single flip of Ising-like spin of subsystem B. From a detailed analysis of the collective and local ESR modes, combined with the magnetization data, we determined the magnetic parameters of subsystems A and B.

CHAPTER 2

EXPERIMENTAL PROCEDURES

2.1 Ba_2CoTeO_6 Sample Preparation

2.1.1 Sample Preparation

The Ba_2CoTeO_6 sample was first prepared in polycrystalline form via conventional solid state method. The chemical reaction is as follows:

$$2BaCO_3 + CoO + TeO_2 + \frac{1}{2}O_2 \longrightarrow Ba_2CoTeO_6 + 2CO_2 \tag{2.1}$$

Stoichiometric amount of reagent-grade $BaCO_3$, CoO and TeO_2 were weighed and mixed in a mortar. The materials were ground until they became well mixed. The materials were placed in an alumina crucible and were calcined at 1000 °C over 24 h in a air. Temperature of furnace was increases to 1000 °C over 6h and held at 1000 °C for 24h and decreased to room temperature over 12 h. Obtained Ba_2CoTeO_6 powder with purple color was ground and calcined again. pressed into an alumina crucible. The powder sample was pressed into pellets using a high-pressure jack. The sample pellets were sintered at 1000 °C over 24 h. This process was repeated again to make homogeneous sample. The samples obtained were examined by X-ray-powder diffraction.

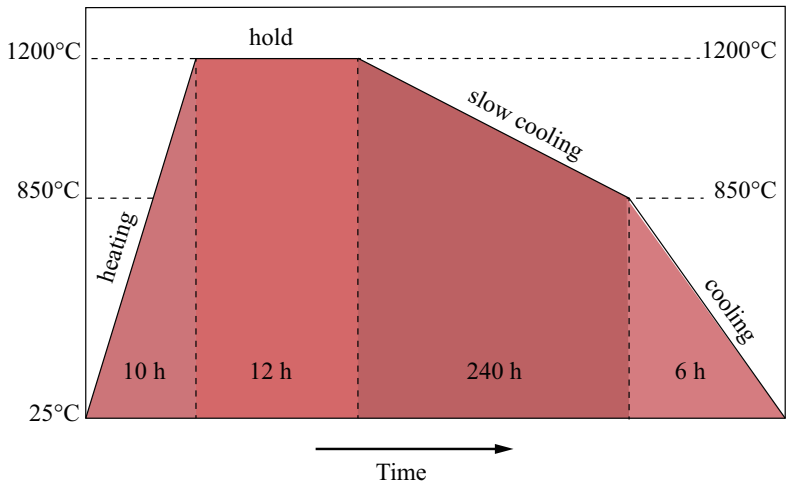

Figure 2.1: Temperature steps at the center of box furnace to grow single crystals of Ba_2CoTeO_6.

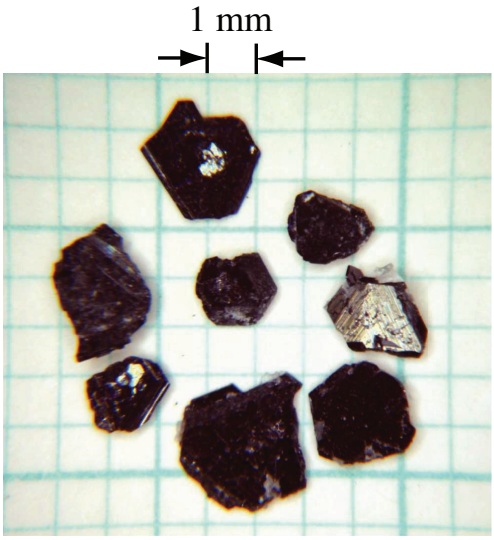

Figure 2.2: Photograph of Ba_2CoTeO_6 single crystals. The color of crystals is black. The wide plane of the crystals is the crystallographic *ab* plane.

We prepared Ba_2CoTeO_6 single crystals via the flux method using $BaCl_2$ as the flux. Ba_2CoTeO_6 powder and $BaCl_2$ were mixed in a molar ratio of 1 : 8 and placed into an alumina crucible. The crucible was covered with an alumina lid and placed in

a bigger crucible and covered with a bigger alumina lid in order to prevent the melted chemicals from overflowing during the heating time. The double crucible with alumina lid were placed in a high-temperature box furnace. Figure 2.1 shows the temperature steps at the center of the furnace. The temperature was increased to 1200 °C over 6 h. Temperature was held at 1200 °C for 12 h and lowered slowly to 840 °C over 240 h. Finally, the furnace was cooled down to room temperature over 12 h. Plate-shaped single crystals with a typical size of $2 \times 2 \times 0.3$ mm^3 were obtained, as shown in Fig. 2.2. The crystal quality prepared by this method is excellent. The wide plane of the crystals is the crystallographic *ab* plane. The crystals are cleaved parallel to the *ab* plane.

2.2 Magnetic Susceptibility Measurement

For precise magnetic susceptibility (χ) measurement at low temperatures, a high sensitive magnetometer is necessary since the magnetic susceptibility of antiferromagnet is usually small. Superconducting Quantum Interference Device (SQUID) is a high sensitive magnetometer appropriated to measure subtle changes in magnetization, especially at low temperatures. In this research, SQUID magnetometer (Quantum Design MPMS XL) was used to measure magnetic susceptibility of Ba_2CoTeO_6. MPMS XL has a sample space surrounded by superconducting magnet and detecting coils and also includes liquid helium cooling system which controls the temperature of the sample space by manipulating the heater and the flow of liquid He-4 from the liquid helium dewar. Figure 2.3 shows the schematic diagram of MPMS XL used in the susceptibility measurements.

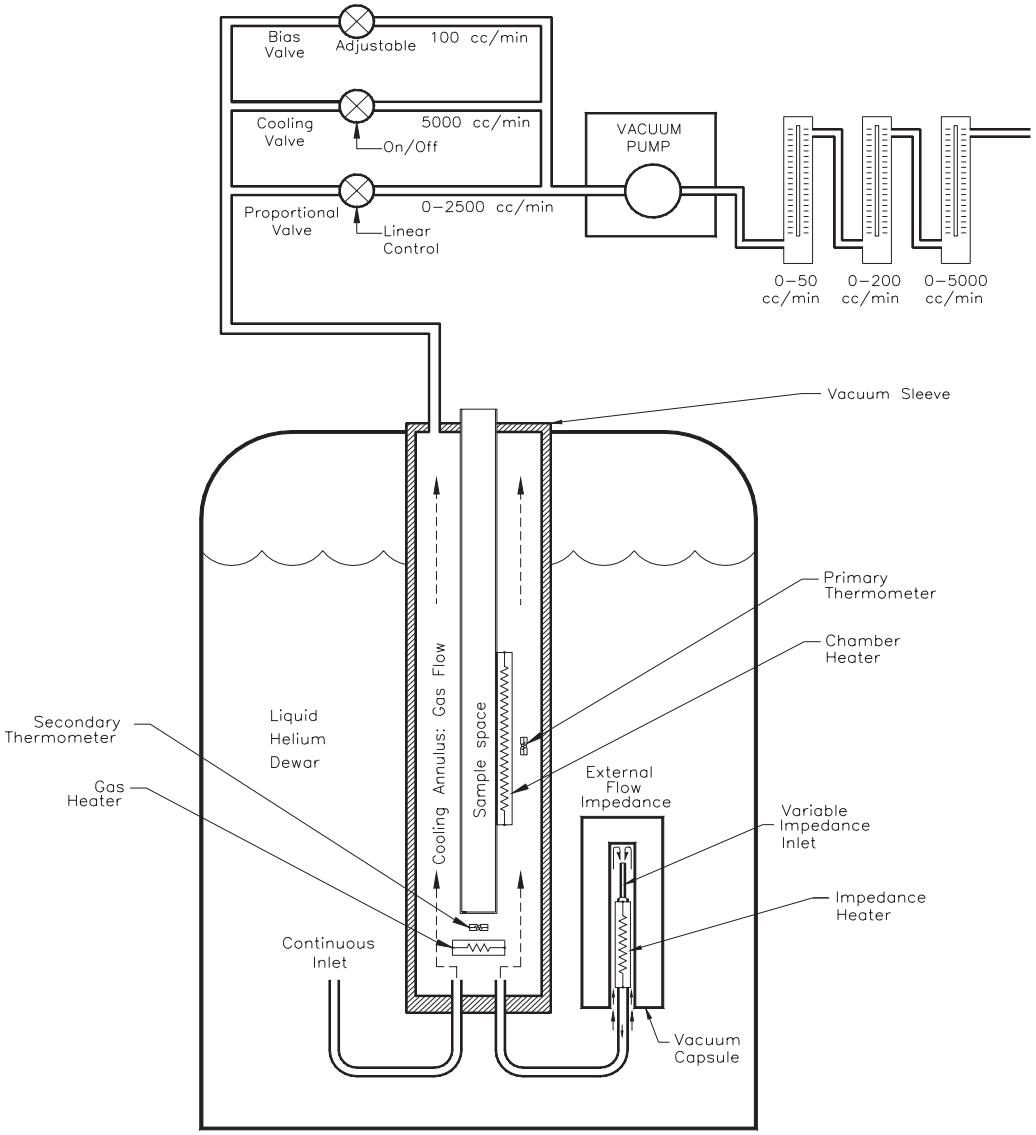

Figure 2.3: Schematic diagram of Quantum Design MPMS XL equipment [59].

2.3 High-field Magnetization Measurement

High field magnetization measurements were performed using an induction method with a multilayer pulse magnet at the International MegaGauss Science Laboratory, Institute

for Solid State Physics (ISSP), the University of Tokyo. Figure 2.4 shows the block diagram of magnetization measuring system. The capacitor bank is connected to the pulse magnet. The pulsed magnetic field is generated by discharging from the capacitor bank. The present measurements were performed using pulsed magnetic field up to 60 T. Cylindrical sample holder is composed of a plastic tube with internal diameter of 3.0 mm. We placed several single crystals of Ba_2CoTeO_6 with their c planes perpendicular and parallel to the cylindrical axis of the holder, so that the magnetic field can be applied parallel and perpendicular to the c axis. When the pulsed magnetic field is applied, the sample is magnetized. Then, the electromotive force is induced in the pick up coil placed around the sample. The magnetization value of the sample was obtained by integrating the electromotive force. We also measured he electromotive force without sample to obtain the resultant electromotive force from the sample only. The present measurements were performed at 4.2 and 1.3 K using liquid ^{4}He as coolant.

Since the raw data are in the form of voltage and time for both magnetization M and magnetic field H data, the first step is to transform them into magnetization and magnetic field data using a software, IGOR Pro. After converting raw magnetization and magnetic field data, the next step is to calibrate them using magnetization data from SQUID magnetometer. Since the data gathered from the measuring equipment is in the form of voltage-time for both magnetization and magnetic field, it needs to be transformed into the data we can analyze. In this research, we used data processing program 'IGOR' to transform the data. In this program, Macro is the function where we can do programming several commands in IGOR program in order to manipulate the data. We used a macro named 'Nicolet' to process the data. By this data process, the raw data were transformed into magnetization vs magnetic field ($M-H$) and dM/dH vs magnetic field ($dM/dH-H$) data.

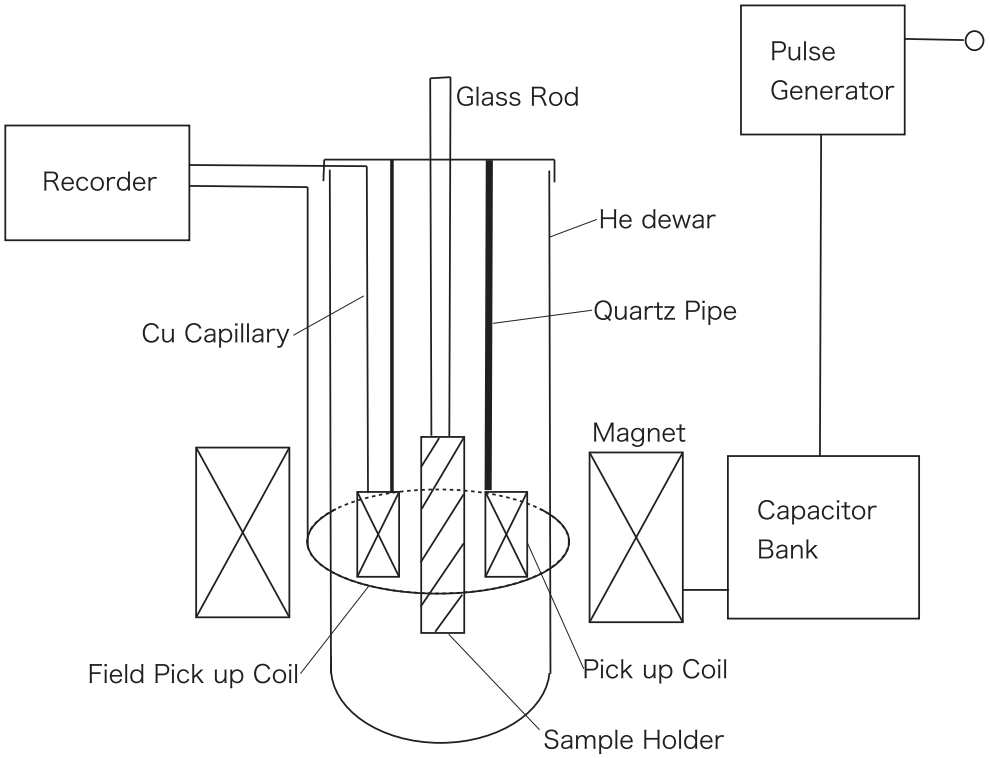

Figure 2.4: Block diagram of high-magnetic-field magnetization measurement, where a pulsed magnetic field is generated using a multilayer pulse magnet [60].

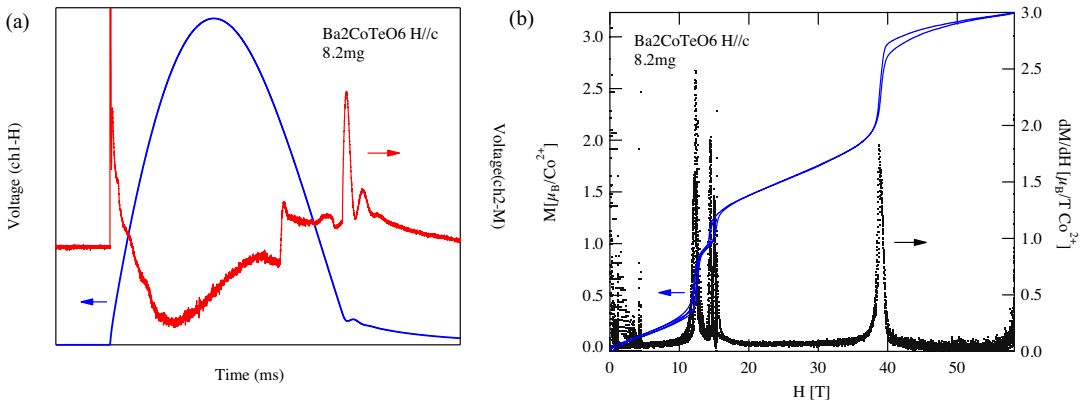

Figure 2.5: (a) The raw data gathered from the detector as a function of voltage and time. The blue line indicates a signal of magnetic field, while the red line is indicating a signal of magnetization. (b) Magnetization data for $H\ c$ obtained from the conversion of voltage and time data by using 'Nicolet' macro in Igor pro.

2.4 Specific Heat Measurement

The specific heat of Ba_2CoTeO_6 single crystals was measured down to 1.8 K in magnetic fields of up to 9 T using a Physical Property Measurement System (Quantum Design PPMS) by the relaxation method. PPMS is the instrument designed to measure various physical properties such as specific heat and resistivity. PPMS with helium-3 option can measure the specific heat down to 0.4 K or even lower with dilution refrigerator option. In PPMS, relaxation method, which is one of the most accurate specific heat measurement techniques, is employed.

Figure 2.6 shows the schematic diagram of sample platform. In order to apply the known amount of heat and to monitor the time variation of the temperature, a platform heater and a platform thermometer are attached to the bottom side of the sample platform. Small wires provide the electrical connection to the platform heater and the platform thermometer and also provide the thermal connection for the platform. The sample is mounted to the platform by using a thin layer of Apiezon-N grease, which provides the required thermal contact to the platform. This setting is surrounded by vacuum of about 0.01 mTorr, so that thermal conductance is totally dominated by the conductance of wires. This gives a reproducible heat link to the bath with a corresponding time-constant large enough to allow both the platform and sample to achieve sufficient thermal equilibrium during the measurements.

Relaxation method is the technique where heating power causes sample base temperature to rise up and cool down within a specific time constant. Relaxation curve is the term that describes changing of temperature within a specific time duration. The analysis of relaxation curve results in obtaining several parameters that will be used to determine the value of the specific heat. The equation describing relaxation curve can be written as [61, 62]:

$$\begin{aligned} T_p =& T_0 + \frac{P_0}{K_{pb}}\Big(1 - \frac{\tau - \tau_2}{\tau_1 - \tau_2}e^{-t/\tau_1} - \frac{\tau_1 - \tau}{\tau_1 - \tau_2}e^{-t/\tau_2}\Big)\{\Theta(t) - \Theta(t - t_0)\} \\ &+ \frac{P_0}{K_{pb}}\Big\{\frac{\tau_2 - \tau}{\tau_1 - \tau_2}e^{-(t-t_0)/\tau_1}(e^{-t_0/\tau_1} - 1) + \frac{\tau - \tau_1}{\tau_1 - \tau_2}e^{-(t-t_0)/\tau_1}(e^{-t_0/\tau_1} - 1)\Big\}\Theta(t - t_0), \end{aligned} \tag{2.2}$$

where T_p, T_0, P_0, $\Theta(t)$ and t represent platform temperature, base temperature, heating power, time duration and time stamp, respectively. For each relaxation curve, T_p is the raw data measured by platform thermometer at time t while T_0, P_0 and $\Theta(t)$ are the constant parameters for each relaxation curve. However, sample dependence parameters, including τ, τ_1, τ_2 and K_{pb} representing delayed-time constant, time constant-1, time constant-2 and wire conductance, respectively, can be obtained by fitting the relaxation curve using least square fitting method. τ, τ_1, τ_2 and K_{pb} obtained from the fitting will be used to determine the value of the specific heat of each relaxation curve [61].

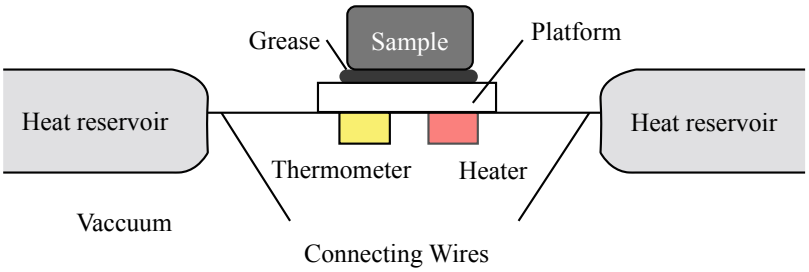

Figure 2.6: Schematic diagram of sample platform for relaxation method.

2.5 Electron Spin Resonance (ESR) Measurement

Due to Zeeman effect, electrons with spin quantum number ($S = \frac{1}{2}$) and $m_\mathrm{s} = \pm 1/2$ align parallel or antiparallel to the applied magnetic field (H) according to its magnetic component m_s. Each alignment has a specific energy given by

$$E = m_\mathrm{s} g \mu_\mathrm{B} H, \tag{2.3}$$

where g represents g-factor of the electron. In the case of unpaired free electron, $g \approx 2.00$.Consequently, The energy separation between lower and upper energy states for unpaired free electron is given by

$$\Delta E = g_e \mu_\mathrm{B} H. \tag{2.4}$$

Electrons in the lower energy state can absorb energy, corresponding to the resonance condition, $\Delta E = h\nu = g\mu_{\mathrm{B}}H$, to change to the upper energy state. This equation is corresponding to fundamental EPR (Electron Paramagnetic Resonance) spectroscopy. Thus, by using this resonance equation, ones can obtain the value of the g-factor of the electron in the lattice where the spin configuration is in paramagnetic state. Figure 2.7 illustrates the Zeeman splitting and ESR absorption at magnetic field corresponding to $h\nu = g\mu_{\mathrm{B}}H$.

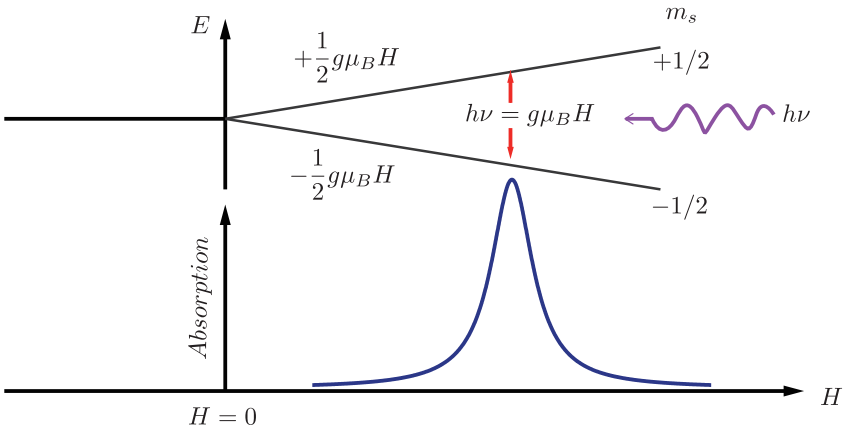

Figure 2.7: Illustration of ESR for unpaired free electron with $m_s = \pm 1/2$ in a magnetic field. Upper and lower panels show the Zeeman splitting and ESR absorption at magnetic field corresponding to $h\nu = g\mu_{\mathrm{B}}H$.

The multifrequency-high magnetic field ESR measurements in both pulsed and static magnetic fields with fixed frequencies ranging from 80 to 450 GHz were performed in the temperature range of $1.5 - 40$ K, at the Institute for Materials Research, Tohoku University. Pulsed magnetic fields up to 25 T and static magnetic fields up to 18 T were applied using a multilayer pulse magnet and a superconducting magnet, respectively. Configuration of ESR measurement using pulsed magnetic fields is illustrated in Fig. 2.8.

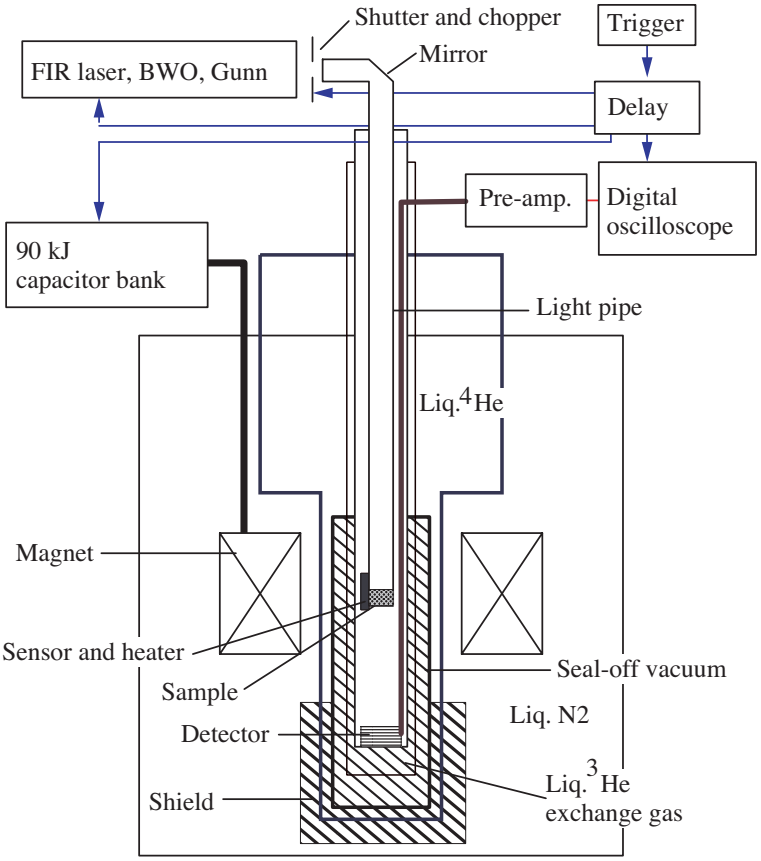

Figure 2.8: Schematic diagram of Terahertz electron spin resonance apparatus: TESRA-IMR, Institute of Materials Research, Tohoku university. [63]

CHAPTER 3

EXPERIMENTAL RESULTS AND ANALYSES

3.1 Magnetic susceptibility

The magnetic susceptibility was measured for both $H \parallel c$ and $H \perp c$ in order to investigate anisotropic properties of the single crystal and to detect phase transition. In Fig. 3.1, we show the temperature dependences of raw magnetic susceptibilities ($\chi = M/H$) measured at $H = 1$ T for $H \parallel c$ (red symbols) and $H \perp c$ (blue symbols). We plotted the susceptibility data for $T \leq 60$ K, where the $S = 1/2$ description of the magnetic moment for Co^{2+} in an octahedral environment is valid.

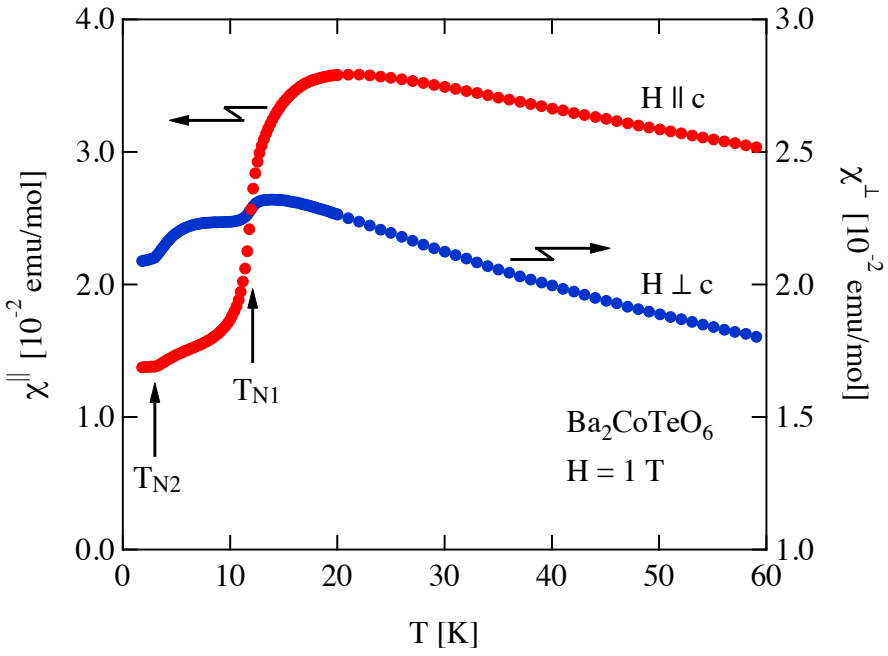

Figure 3.1: Temperature dependences of magnetic susceptibilities in Ba_2CoTeO_6 measured for $H \parallel c$ and $H \perp c$ at $H = 1$ T. Two vertical arrows indicate anomalies caused by magnetic phase transitions at $T_{N1} = 12.0$ K and $T_{N2} = 3.0$ K.

As seen in Fig. 3.1, the magnitude and temperature dependence of magnetic susceptibility is very anisotropic. Because the symmetry of the crystalline field acting on

Co^{2+} in subsystem A should be close to cubic one, the magnetic susceptibility produced by subsystem A is expected to be nearly isotropic. Thus, The anisotropic susceptibility observed is attributed to the anisotropic g-factor and exchange interaction in subsystem B, in which the symmetry of the crystalline fields acting on Co^{2+} is far from the cubic symmetry due to the noncentrosymmetric distortion of $Co(2)O_6$. Because the magnetic susceptibility for $H \parallel c$ is much larger than that for $H \perp c$, the g-factor for $H \parallel c$, $g_{\rm B}^{\parallel}$, is sufficiently larger than the g-factor for $H \perp c$, $g_{\rm B}^{\perp}$. This indicates that the effective exchange interaction expressed by Eq. (1.8) is Ising-like in subsystem B, i.,e., $J^{\parallel} \gg J^{\perp}$.

For $H \parallel c$, the magnetic susceptibility exhibits a rounded maximum at 20 K and an inflection point at $T_{\rm N1} = 12.0$ K owing to magnetic ordering, which is consistent with $T_{\rm N} \simeq 12$ K reported by Ivanov *et.al.* [56]. With decreasing temperature, the magnetic susceptibility exhibits a bend anomaly at $T_{\rm N2} = 3.0$ K indicative of the second magnetic ordering, which was not reported by Ivanov *et.al.* [56]. The magnetic susceptibility for $H \perp c$ also shows the inflectional and bend anomalies at $T_{\rm N1}$ and $T_{\rm N2}$, respectively. The successive magnetic phase transitions observed by the susceptibility measurements were confirmed by the specific heat measurements shown below.

The temperature dependences of the magnetic susceptibilities measured at various magnetic fields for $H \parallel c$ and $H \perp c$ are displayed in Figs. 3.2(a) and (b). With increasing magnetic field for $H \parallel c$, $T_{\rm N1}$ shifts toward the low-temperature side, which is more clearly observed in specific heat data shown below. On the other hand, the shift of $T_{\rm N2}$ in the magnetic field is little. However, the bend anomaly at $T_{\rm N2}$ becomes difficult to distinguish with increasing magnetic field above 3 T. For $H \perp c$, the first magnetic ordering temperature $T_{\rm N1}$ slightly shifts toward the low-temperature side with increasing the magnetic field. The bend anomaly at $T_{\rm N2}$ can be observed below 5 T. However, it changes into a cusp anomaly at the magnetic field above 6 T.

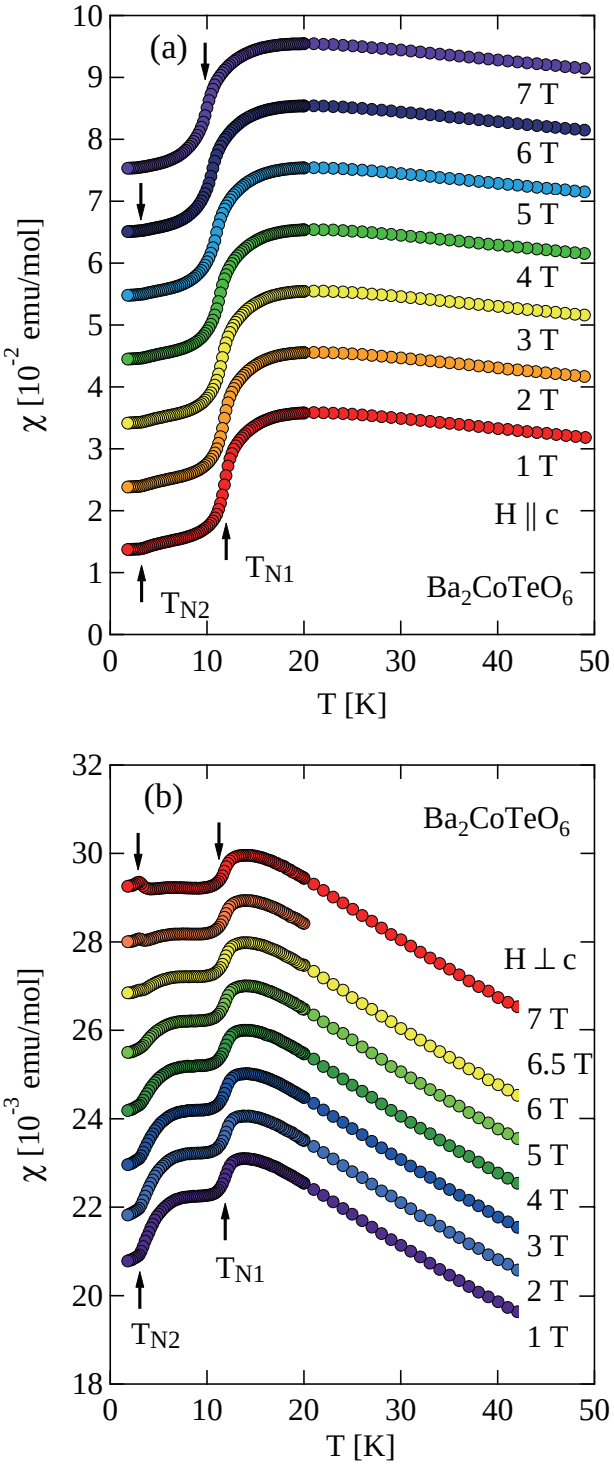

Figure 3.2: Temperature dependences of magnetic susceptibilities in Ba_2CoTeO_6 measured at various magnetic fields (a) for $H \parallel c$ and (b) for $H \perp c$. The susceptibility data are shifted upward by multiples of (a) 1×10^{-2} emu/mol and (b) 1×10^{-3} emu/mol. Vertical arrows indicate anomalies caused by magnetic phase transitions T_{N1} and T_{N2}.

3.2 Specific heat in zero and finite magnetic field

Figures 3.3 and 3.4 show the temperature dependences of the specific heat divided by temperature, C/T, below 16 K measured at various magnetic field for $H \parallel c$ and $H \perp c$, respectively. At zero magnetic field, two sharp peaks indicative of magnetic phase transitions are observed at $T_{N1} = 11.93$ and $T_{N2} = 2.91$ K, which are coincide with the transition temperatures $T_{N1} = 12.0$ and $T_{N2} = 3.0$ K determined from the temperature dependence of the magnetic susceptibility.

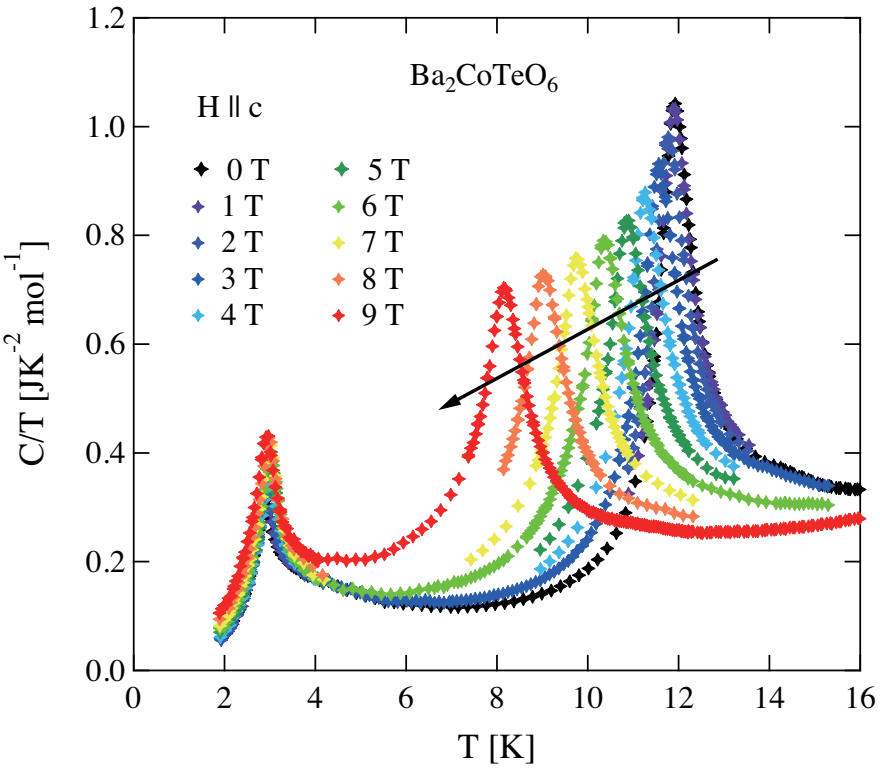

Figure 3.3: Temperature dependence of specific heat divided by temperature (C/T) of Ba_2CoTeO_6 measured at various magnetic fields for $H \parallel c$.

For $H \parallel c$, the higher transition temperature T_{N1} shifts toward the low-temperature side with increasing magnetic field, whereas the lower transition temperature T_{N2} is almost independent of the magnetic field. For $H \perp$ c, the lower transition temperature T_{N2} starts to split into two transitions at approximately 7 T with increasing magnetic field

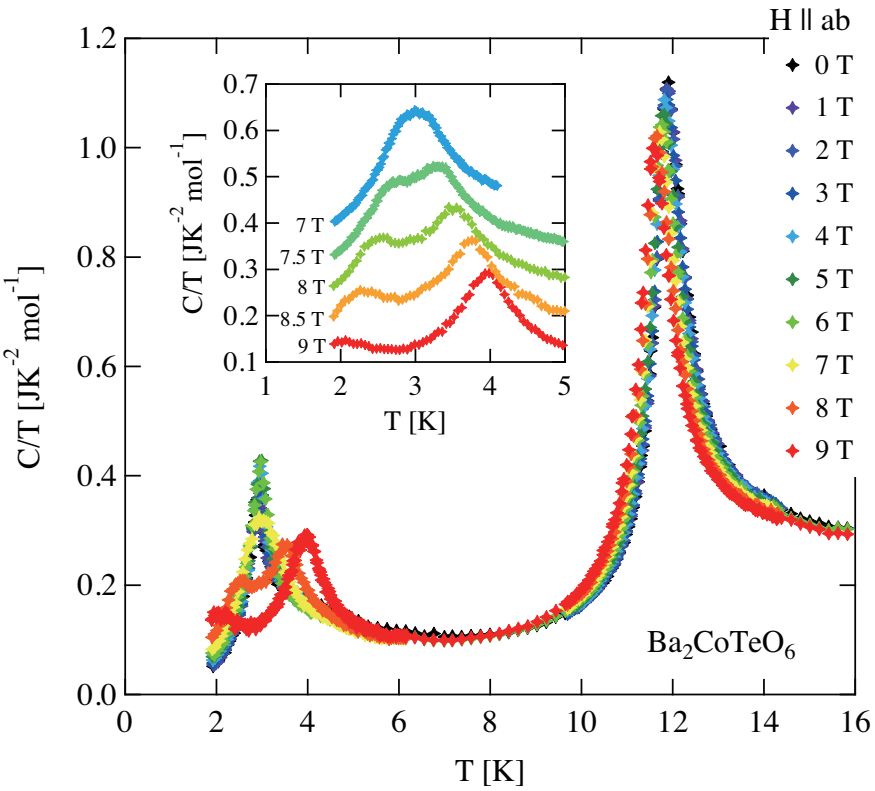

Figure 3.4: Temperature dependence of specific heat divided by temperature (C/T) measured at various magnetic fields for $H \perp$ c. The inset shows the splitting of specific heat peak for $H \geq 7$ T, The data are shifted upward by multiples of 0.08 J/mol K^2.

(see inset of Fig. 3.4), whereas T_{N1} shifts slightly toward the low-temperature side. The specific heat results at varied magnetic fields are consistent with those from susceptibility measurement. The behavior of specific heat in magnetic fields is quite similar to that observed in $S = 1/2$ Heisenberg TLAF $Ba_3CoSb_2O_9$ [15].

Figure 3.5 shows magnetic field vs temperature phase diagram in Ba_2CoTeO_6 for $H \parallel c$ and $H \perp c$. In Fig. 3.5, transition data above 10 T were obtained from the high-field magnetization measurements shown below. The phase labeled "Para" represents the paramagnetic phase. "LF I" is the low-field phase, in which only spins in subsystem B are ordered, while in the "LF II" phase, spins in both subsystems, A and B, are ordered. In phases labeled "1/3 - PB" and "1/2 - PB" for $H \parallel c$, Ising-like subsystem B exhibits 1/3 - and 1/2 - magnetization plateaus, respectively, as shown below. In a phase "1/3 - PA", Heisenberg-like subsystem A displays a quantum 1/3-magnetization plateau.

The behavior of the phase boundaries related to T_{N2} is very similar to that observed in $Ba_3CoSb_2O_9$, as shown in Fig. 1.15 [17]. This indicates that the phase transition at T_{N2} corresponds to the magnetic ordering of Heisenberg-like subsystem A.

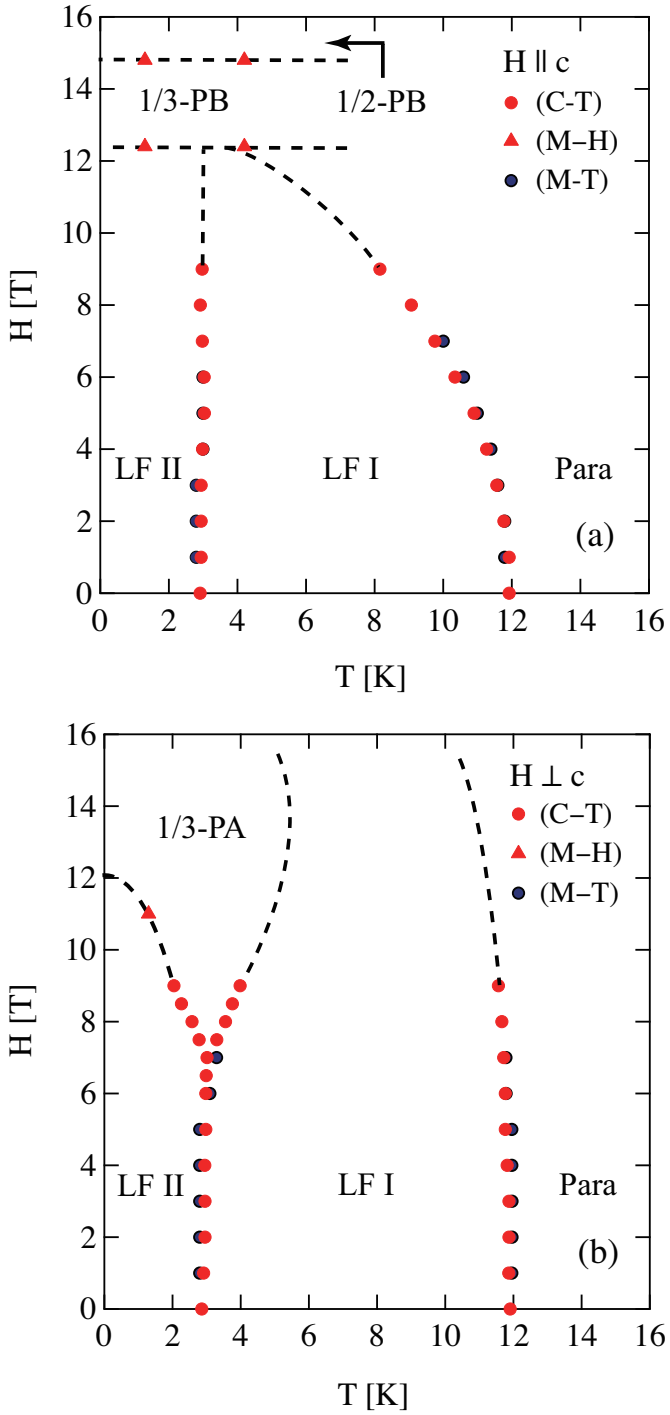

Figure 3.5: Temperature vs magnetic field phase diagram in Ba_2CoTeO_6 (a) for $H \parallel c$ and (b) $H \perp c$. Transition data obtained from the temperature dependencies of specific heat and magnetic susceptibility are plotted using red and black closed circles, respectively, and those obtained from high-field magnetization measurements are plotted using closed triangles. Dashed lines are visual guides. For labeling and spin states of phases "Para", "LF I", "LF - II", "1/3 - PB", "1/2-PB" and "1/3 - PA" see text.

3.3 Magnetization process

Figure 3.6(a) shows the magnetization curves measured at 1.3 K for $H \parallel c$. Three phase transitions with a magnetization jump are observed at $H_{c1}^{\parallel} = 12.3$ T, $H_{c2}^{\parallel} = 14.8$ T, and $H_{s}^{\parallel} = 39.0$ T. These transitions are accompanied with a small hysteresis. For $H_{s}^{\parallel}$, transition fields upon sweeping magnetic field up and down are almost the same, while those for $H_{c1}^{\parallel}$ and $H_{c2}^{\parallel}$ are somewhat different, which is more clearly observed from $dM_{raw}^{\parallel}/dH$ vs H shown in Fig. 3.6(b). However, above $H_{s}^{\parallel}$, a fairly large hysteresis is observed. Although we do not have clear explanation of the hysteresis, it is considered that the hysteresis above $H_{s}^{\parallel}$ is ascribed to the magnetocaloric effect, whereas the hysteresis at $H_{c1}^{\parallel}$ and $H_{c2}^{\parallel}$ is intrinsic hysteresis characteristic of the first order transition. The hysteresis becomes smaller with increasing temperature as shown in Fig. 3.7.

From Fig. 3.6(a), we can see that the slopes of the raw magnetization $M_{raw}^{\parallel}$ for $H < H_{c1}^{\parallel}$ and $H_{c2}^{\parallel} < H < H_{s}^{\parallel}$ are almost the same, whereas, the magnetization slope for $H > H_{s}^{\parallel}$ is smaller than those for $H < H_{s}^{\parallel}$. It is natural to interpret that the magnetization produced by the effective spin-1/2 saturates at $H_{s}^{\parallel}$, and that the linear increase in magnetization for $H > H_{s}^{\parallel}$ is attributed to the large temperature-independent Van Vleck paramagnetism, which is characteristic of Co^{2+} in octahedral environment. From the magnetization slope for $H > H_{s}^{\parallel}$, the Van Vleck paramagnetic susceptibility is evaluated as $\chi_{VV}^{\parallel} = 6.09 \times 10^{-3}$ emu/mol. The value of $\chi_{VV}^{\parallel}$ and that observed in $Ba_3CoSb_2O_9$ [16] are the same order in magnitude. $M_{A+B}^{\parallel}$ in Fig. 3.6(a) is the magnetization obtained by subtracting the Van Vleck paramagnetism. The saturation magnetization is estimated to be $M_{s}^{\parallel} = 2.60\ \mu_B/Co^{2+}$.

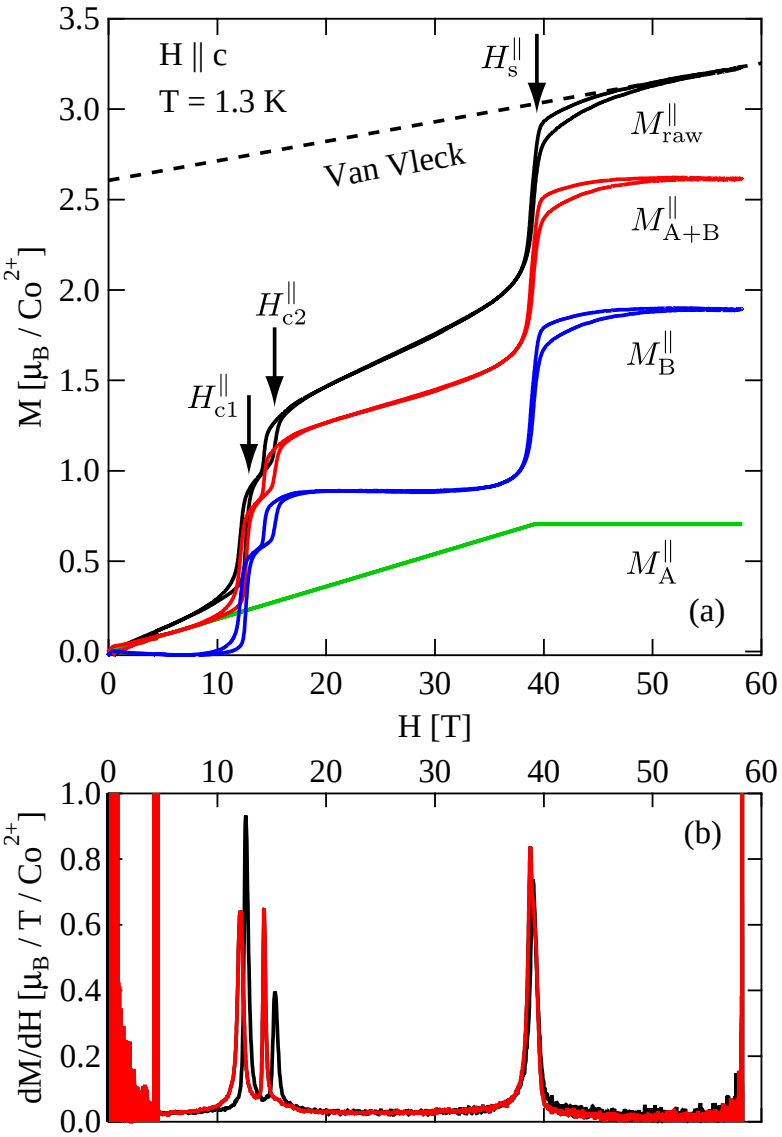

Figure 3.6: Magnetization curves in Ba_2CoTeO_6 measured at 1.3 K for $H \parallel c$. $M_{raw}^{\parallel}$ and $M_{A+B}^{\parallel}$ are the raw magnetization and the magnetization corrected for the Van Vleck paramagnetism, respectively. $M_{A+B}^{\parallel}$ is divided into two components $M_A^{\parallel}$ and $M_B^{\parallel}$ produced by spins in subsystem A and B, respectively. Transition fields are indicated by vertical arrows. (b) Field derivative of the raw magnetization $dM_{raw}^{\parallel}/dH$ measured at 1.3 K in the magnetic field up to 58 T for $H \parallel c$. Black and red lines denote the data obtained on sweeping field up and down, respectively.

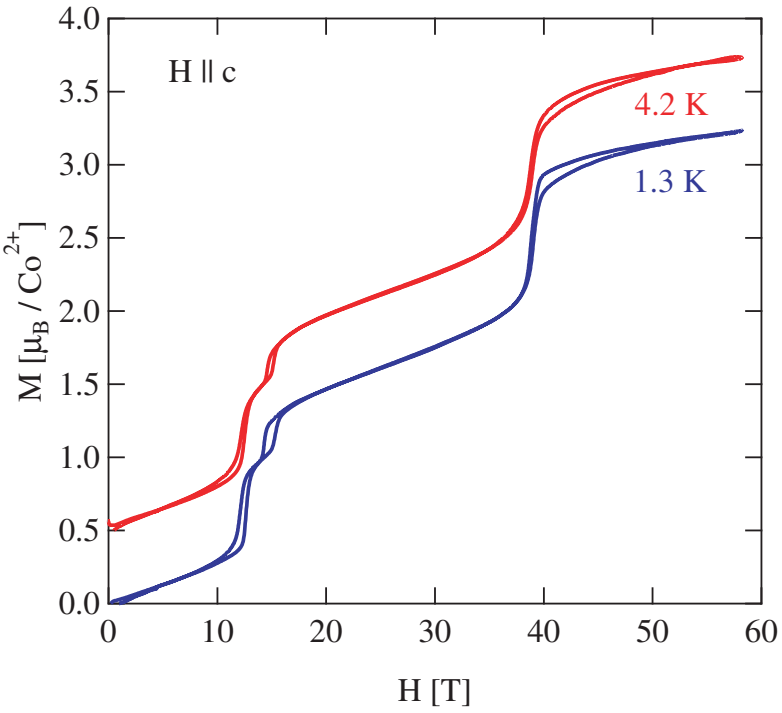

Figure 3.7: Magnetization curves for $H \parallel c$ measured at $T = 4.2$ and 1.3 K, which are between T_{N1} and T_{N2}, and below T_{N2}, respectively.

For $M^{\parallel}_{A+B}$ curve, the slopes for $H < H^{\parallel}_{c1}$ and $H^{\parallel}_{c2} < H < H^{\parallel}_{s}$ are almost the same. In the $S = 1/2$ Heisenberg-like TLAF $Ba_3CoSb_2O_9$, the magnetization increases roughly in proportion to H with increasing magnetic field as shown in Fig. 1.14(b) [16], although the magnetization curve is slightly convex function of H. Because the environment of Co^{2+} in subsystem A is close to that in $Ba_3CoSb_2O_9$, we can expect that the field dependence of the magnetization produced by subsystem A is similar to that observed in $Ba_3CoSb_2O_9$. Because the stepwise magnetization is also observed at 4.2 K, which is above T_{N2} but below T_{N1}, we can deduce that the stepwise magnetization is produced by Ising-like spins in subsystem B. Thus, we can assume that the component $M^{\parallel}_{A}$ produced by subsystem A increases almost linearly in H and saturates near 39 T, while the component $M^{\parallel}_{B}$ produced by subsystem B shows a stepwise magnetization process with plateaus at 0, 1/3 and 1/2 of the saturation magnetization, which is characteristic of the Ising spin system, and that $M^{\parallel}_{A+B}$ is given by the superposition of $M^{\parallel}_{A}$ and $M^{\parallel}_{B}$. From the analysis of the magnetization curve for $H \parallel c$, the g-factors in subsystems A

and B are evaluated to be $g_{\rm A}^{\parallel} \simeq 4.22$ and $g_{\rm B}^{\parallel} \simeq 5.66$, respectively. It should be noted that the g-factors evaluated from the ESR data are $g_{\rm A}^{\parallel} = 3.65$ and $g_{\rm B}^{\parallel} = 6.27$, respectively, as shown later.

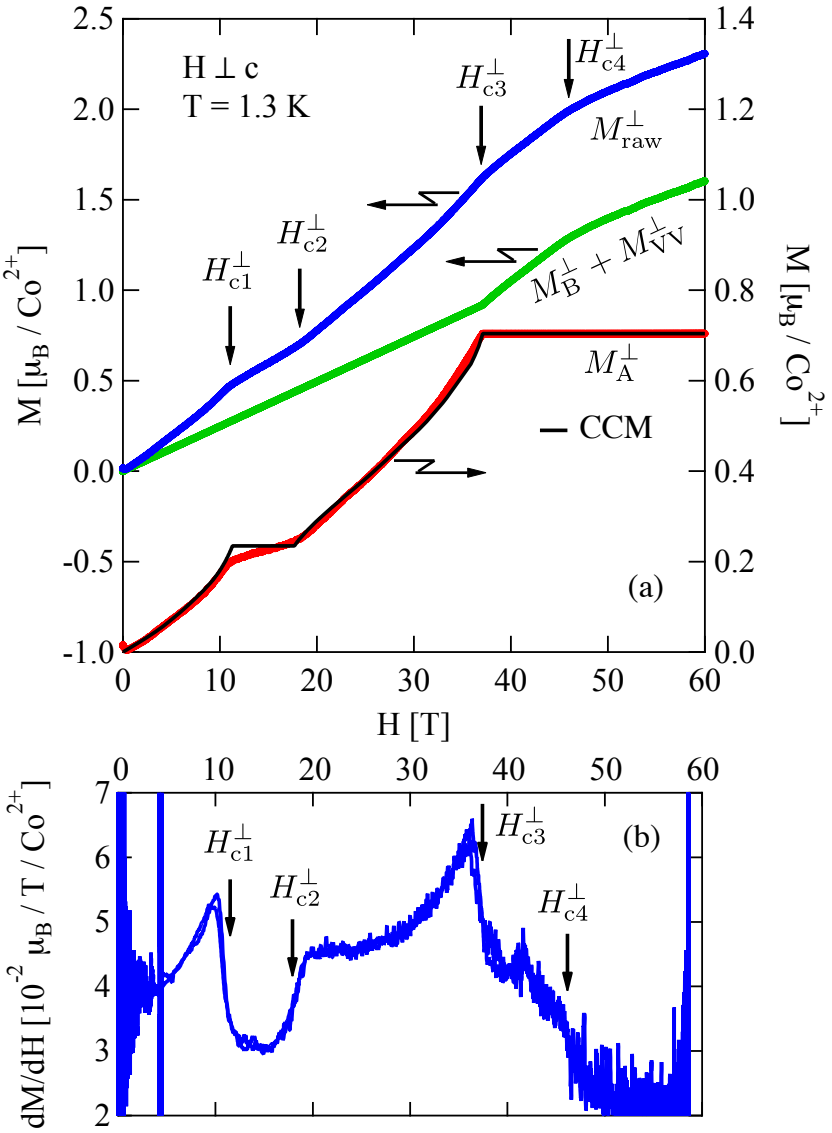

Figure 3.8: (a) Magnetization curve in Ba_2CoTeO_6 measured at 1.3 K for $H \perp c$. $M_{\rm raw}^{\perp}$ and $M_{\rm B}^{\perp}+M_{\rm VV}^{\perp}$ are the raw magnetization and the sum of the magnetizations of the subsystem B and the Van Vleck paramagnetism, respectively. $M_{\rm A}^{\perp}$ is the magnetization extracted as the magnetization of subsystem A. Vertical arrows indicate the transition fields determined from the $dM_{\rm raw}^{\parallel}/dH$ data shown in (b). The solid line is the theoretical magnetization curve calculated by the coupled cluster method (CCM) [6]. (b) Field derivative of the raw magnetization $dM_{\rm raw}^{\parallel}/dH$ measured at 1.3 K for $H \perp c$. The $dM_{\rm raw}^{\parallel}/dH$ data up to 40 T is very similar to that observed in $Ba_3CoSb_2O_9$, as shown in Fig. 1.13(a).

Figure 3.8 shows the raw magnetization curve $M^{\perp}_{\rm raw}$ and its field derivative $dM^{\perp}_{\rm raw}/dH$ for $H \perp$ c measured at 1.3 K. In $dM^{\perp}_{\rm raw}/dH$ vs H, four transitions are clearly observed at $H^{\perp}_{\rm c1} = 11.0$ T, $H^{\perp}_{\rm c2} = 18.0$ T, $H^{\perp}_{\rm c3} = 37.2$ T and $H^{\perp}_{\rm c4} = 45.9$ T. The magnetization obtained by extrapolating the magnetization slope above $H^{\perp}_{\rm c4}$ to zero magnetic field is approximately 1.0 $\mu_B/{\rm Co}^{2+}$, which is half of the saturation magnetization $M^{\perp}_{\rm s} \simeq 2.0$ $\mu_{\rm B}/{\rm Co}^{2+}$ expected from the g-factors for $H \perp c$. Thus, $H^{\perp}_{\rm c4}$ is not the saturation field.

As shown in Fig. 3.8(b), the magnetic field dependence of $dM^{\perp}_{\rm raw}/dH$ for $H \leq H^{\perp}_{\rm c3}$ is very similar to that observed for $H \perp c$ in the $S = 1/2$ Heisenberg-like TLAF $Ba_3CoSb_2O_9$ with small easy-plane anisotropy [16] (see Fig. 1.13(a)). Three critical fields $H^{\perp}_{\rm c1}$, $H^{\perp}_{\rm c2}$, and $H^{\perp}_{\rm c3}$ coincide with the lower and upper edge fields of the 1/3 - magnetization plateau and saturation field in $Ba_3CoSb_2O_9$ for $H \perp c$ [16] when we rescale the magnetic field. This indicates that the magnetization process of subsystem A for $H \perp c$ is little affected by subsystem B. From this observation together with the fact that the total magnetization for $H \parallel c$ is approximately given by the superposition of individual magnetizations for subsystems A and B, we can deduce that subsystems A and B are approximately decoupled.

Assuming that the magnetization for the Ising-like subsystem B is linear in H up to $H^{\perp}_{\rm c3}$, which is typical of the case for H perpendicular to the easy-axis in three-dimensional Ising antiferromagnet [54] (see Fig. 1.20), and the g-factor of subsystem A for $H \perp c$ is almost the same as $g^{\parallel}_{\rm A} \simeq 4.22$, we divide $M^{\perp}_{\rm raw}$ into the magnetization of subsystem A ($M^{\perp}_{\rm A}$) and the sum of the magnetization of subsystem B and Van Vleck paramagnetic magnetization ($M^{\perp}_{\rm B} + M^{\perp}_{\rm VV}$), as shown in Fig. 3.8(a). $M^{\perp}_{\rm A}$ displays a 1/3 - plateau caused by the quantum order-by-disorder [3–11]. The solid line in Fig. 3.8(a) is the theoretical magnetization curve calculated by the coupled cluster method (CCM) [6] with $J/k_{\rm B} = 23.5$ K and $g^{\perp}_{\rm A} = 4.22$. The magnetization $M^{\perp}_{\rm A}$ is in good agreement with the theoretical result. The behavior of the magnetization $M^{\perp}_{\rm A}$ is very similar to the magnetization for $H \perp c$ in the $S = 1/2$ Heisenberg-like TLAF $Ba_3CoSb_2O_9$ with small easy-plane anisotropy [16] (see Fig. 1.13(a)). This indicates that the spins in subsystem

A are ordered parallel to the *ab* plane below $T_{N2} = 3.0$ K. This ordered spin structure of subsystem A can be confirmed by the electron spin resonance mode shown below. As shown in Fig. 3.5, the magnetic field dependence of the phase boundary for T_{N2} is similar to that for the phase boundary observed in $Ba_3CoSb_2O_9$ (see Fig. 1.15). From this fact and the results of magnetization measurements, we can deduce that the spins in subsystem A are paramagnetic above T_{N2} and the spins in subsystem B are ordered parallel to the *c* axis below T_{N1}, although Ivanov *et al.* [56] reported that all the spins are ordered at $T_N \simeq 15$ K with canting by an angle of 24.5° from the *c* axis. In order to verify our prediction, neutron diffraction experiment is necessary.

The results of high-field magnetization measurements show that the total magnetization is approximately given by the superposition of magnetizations for isolated subsystems A and B. This indicates that the coupling between the two subsystems is weak. It is considered that the anomalies at $H_{c3}^{\perp} = 37.2$ and $H_{c4}^{\perp} = 45.9$ T in $M_B^{\perp} + M_{VV}^{\perp}$ for $H \perp c$ are attributed to the quantum phase transitions in subsystem B. Usually, the magnetization curve for the classical Ising-like magnet is linear in H and displays no transition up to the saturation when the magnetic field is applied parallel to the hard axis. Therefore, we speculate that these transitions are the quantum phase transitions due to the transverse magnetic field in the $J_1 - J_2$ Ising-like HLAF. The transitions at $H_{c3}^{\perp} = 37.2$ T for $H \perp c$ and at $H_s^{\parallel} = 39.0$ T for $H \parallel c$ occur simultaneously in both subsystems. If the interaction between the subsystems is negligible, then these transitions take place independently. It is considered that the transitions that take place originally at slightly different magnetic fields in these two subsystems occur simultaneously with the help of the weak exchange interaction between the subsystems.

As described above, the magnetization of subsystem A exhibits the 1/3 - plateau for $H \perp c$, while the for $H \parallel c$ the magnetization displays no anomaly corresponding to the transition between the umbrella state to the high-field coplanar state observed in $Ba_3CoSb_2O_9$. It seems that this is because the magnetization anomaly the transition is weak. Then, we measured the magnetocaloric effect (MCE) for $H \parallel c$. The measure-

ment was performed at Institute of Materials Research, Tohoku university. Figure 3.9 shows the preliminary data of MCE measured sweeping magnetic field down. We can see that sharp decrease in the resistance of thermometer owing to the MCE at near two critical fields $H_{c1}^{\parallel} = 12.3$ and $H_{c2}^{\parallel} = 14.8$ T observed by the high-field magnetization measurements for $H \parallel c$. In addition to these anomalies, a sharp anomaly is observed at $H_{c0}^{\parallel} = 11.6$ H. Because the magnetic parameters in $Ba_3CoSb_2O_9$ are similar to those in subsystem A and the transition between the umbrella state to the high-field coplanar state occurs at 11.5 T for $H \parallel c$, we infer that the transition detected by the MCE for $H \parallel c$ is the transition between the umbrella state to the high-field coplanar state.

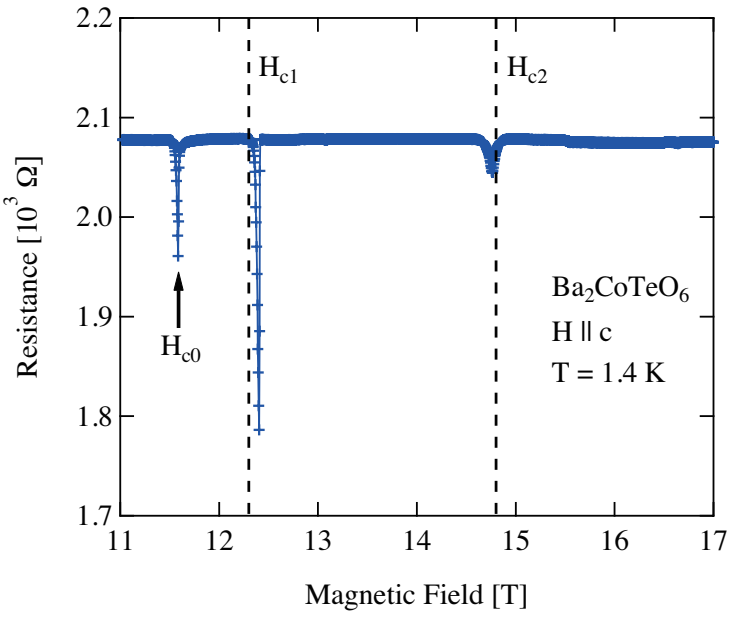

Figure 3.9: Magnetocaloric effect (MCE) measurement at 1.4 K with sweeping magnetic field down for $H \parallel c$. Vertical axis denotes the resistance of thermometer, which corresponds to the temperature. Two vertical dashed lines denote the critical fields $H_{c1}^{\parallel} = 12.3$ and $H_{c2}^{\parallel} = 14.8$ T observed by the high-field magnetization measurements for $H \parallel c$.

3.4 Ground state for $H \parallel c$ in subsystem B

In this section, we will investigate field-driven classical ground states of subsystem B for $H \parallel c$. For simplification, we assume the $J_1 - J_2$ Ising HLAF. To the best of our

knowledge, In case that J_1 is much larger than J_2, the structure is considered to be a simple antiferromagnetic ordering ("AF I"), as shown in Fig. 3.10(a). However, the magnetic unit cell below T_{N1} reported by [56] is enlarged to $2a \times a$. This indicates that "AF II" structure as shown in Fig. 3.10(b) is realized at zero magnetic field. The energy states of AF I and AF II per spin can be expressed by

$$E^{(\mathrm{a})} = -\frac{3}{8}J_1 + \frac{3}{4}J_2, \tag{3.1}$$

and

$$E^{(\mathrm{b})} = -\frac{1}{8}(J_1 + 2J_2). \tag{3.2}$$

From the condition of $E^{(\mathrm{b})} < E^{(\mathrm{a})}$, we can conclude that $J_1 < 4J_2$ in Ba_2CoTeO_6.

According to the Kanamori theory [55], the stable state just below the saturation field is such that the density of the down spins is maximum under the condition that no two down spins interact via given exchange interactions. Considering this condition, two spin states shown in Figs. 3.10(f) and 3.10(g) are appropriate and have the maximum magnetization of $M = M_{\mathrm{Bs}}^{\parallel}/2$. These two states possess the same energy as

$$E^{(\mathrm{f,g})} = \frac{1}{4}h, \tag{3.3}$$

with $h = g\mu_{\mathrm{B}}H$. Here, we note that the spin state of the 1/2 - plateau state is infinitely degenerate, because any sequences of (f) and (g) structure in the b direction with the same pattern in the a direction posses the same energy. Comparing $E^{(\mathrm{f,g})}$ with the energy of the saturated state given by

$$E^{(\mathrm{s})} = \frac{3}{8}(J_1 + 2J_2) - \frac{h}{2}, \tag{3.4}$$

the saturation field is obtained as

$$h_{\mathrm{s}} = \frac{3}{2}J_1 + 3J_2. \tag{3.5}$$

The spin structures shown in Figs. 3.10(c) - 3.10(e) are candidates of the 1/3 - plateau state. Energies of structures in Figs. 3.10(c) and 3.10(d) are the same and is

expressed as

$$E^{(\mathrm{c,d})} = -\frac{1}{24}(3J_1 - 2J_2) - \frac{h}{6}. \tag{3.6}$$

We note that the 1/3 - plateau state with structures in Figs. 3.10(c) and 3.10(d) is infinitely degenerate, because any sequences of these two structures in the b direction with the same pattern in the a direction have the same energy. The energy of the structure in Fig. 3.10(e) is given by

$$E^{(\mathrm{e})} = \frac{1}{24}(J_1 - 6J_2) - \frac{h}{6}. \tag{3.7}$$

Comparing $E^{(\mathrm{c,d})}$ and $E^{(\mathrm{e})}$, we see that the structures in Figs. 3.10(c) and 3.10(d) are stable for $J_1 \geq 2J_2$, while the structure in Fig. 3.10(e) is stable for $J_1 < 2J_2$.

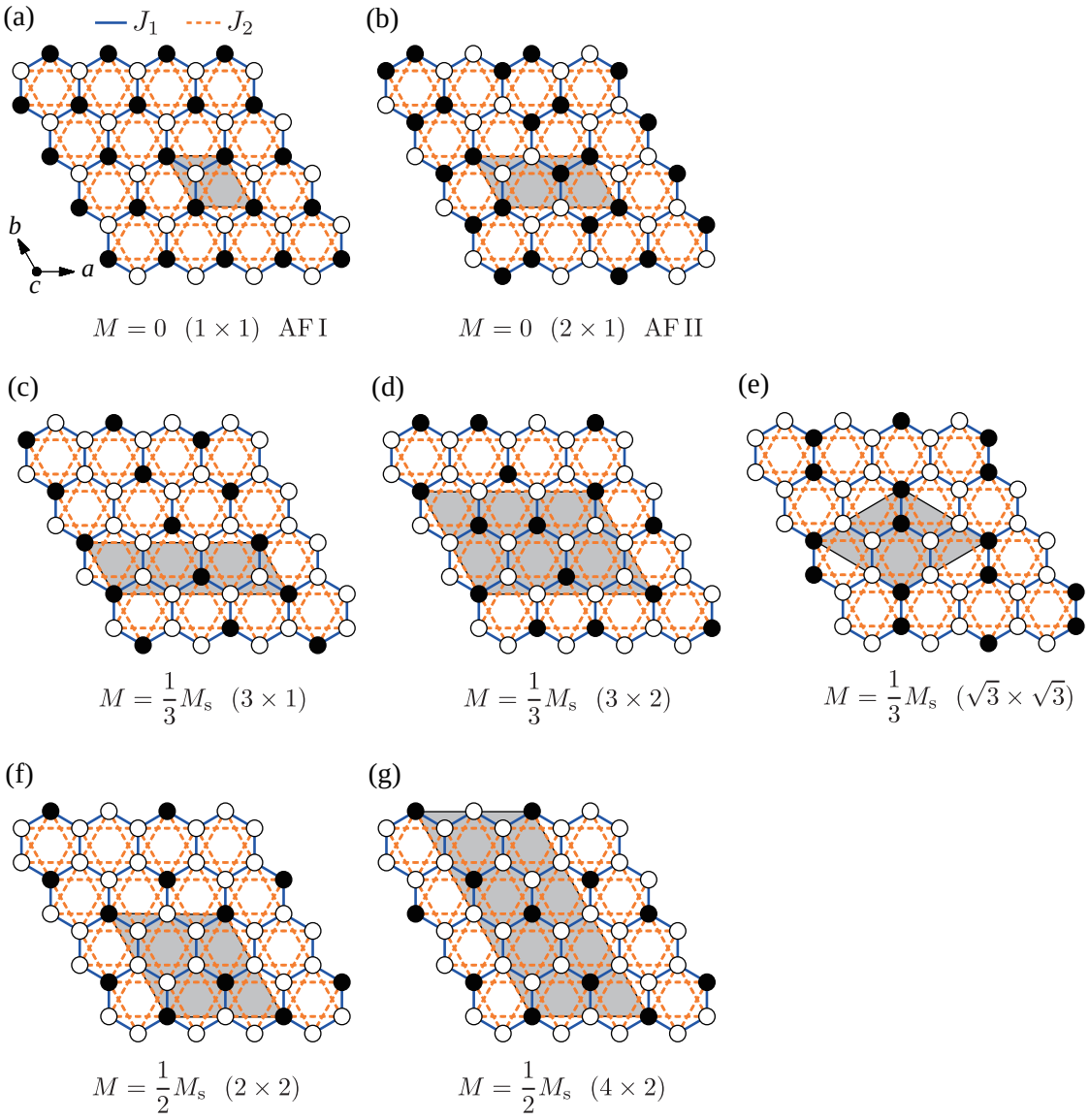

Figure 3.10: Models of spin arrangements at magnetization plateau states for subsystem B, which were derived on the basis of the J_1-J_2 Ising honeycomb lattice antiferromagnet. The nearest neighbor J_1 and next-nearest neighbor J_2 exchange interactions are expressed by blue solid line and orange dashed line, respectively. Up and down spins are indicated by open and closed circles, respectively. Magnetic unit cells are represented by shaded parallelograms. (a) A simple antiferromagnetic state on a hexagonal structure (AF I) stabilized when $J_2 < J_1/4$. (b) An antiferromagnetic state with the 2×1 enlarged unit cell (AF II) observed at zero magnetic field below T_{N1} [56]. This spin state is stabilized when $J_2 > J_1/4$. Spin states in (c), (d), and (e) are candidates for the 1/3 - plateau state. Spin states in (f) and (g) are those for the 1/2 - plateau state.

Using six energies $E^{(a)}, E^{(b)}, E^{(f,g)}, E^{(s)}, E^{(c,d)}$ and $E^{(e)}$, we can calculate the phase boundaries in magnetic fields for the J_1-J_2 Ising HLAF. Comparing $E^{(c,d)}$ and $E^{(e)}$ with the energy of the zero-field ground state $E^{(b)}$, the critical field h_{c1} is obtained

as

$$h_{c1} = \begin{cases} 2J_2 & (\text{for } J_1 \geq 2J_2), \\ J_1 & (\text{for } J_1 < 2J_2). \end{cases} \tag{3.8}$$

Similarly, the critical field h_{c2} is obtained as

$$h_{c2} = \begin{cases} \frac{1}{2}(3J_1 - 2J_2) & (\text{for } J_1 \geq 2J_2), \\ \frac{1}{2}(6J_2 - J_1) & (\text{for } J_1 < 2J_2). \end{cases} \tag{3.9}$$

Figure 3.11 displays the ground state phase diagram in the $J_1/J_2 - h/J_1$ plane.

Using $H_{c1}^{\parallel} = 12.3$ T, $H_s^{\parallel}$, and $g_B^{\parallel} = 6.30$, we get $J_1/k_B = 57.8$ K and $J_2/k_B = 26.0$ K for $J_1 \geq 2J_2$, and $J_1/k_B = 51.9$ K and $J_2/k_B = 28.9$ K for $J_1 < 2J_2$. In Fig. 3.11, two dashed lines parallel to the y axis represent the ground states for the cases of $J_1/J_2 = 0.45$ and 0.55, respectively. Using these parameters, $H_{c2}^{\parallel}$ can be estimated as $H_{c2}^{cal} = 14.4$ T, which is almost the same as the experimental value $H_{c2}^{exp} = 14.8$ T. This result confirms that subsystem B is described as the $J_1 - J_2$ Ising HLAF and is approximately decoupled from subsystem A. We see that in Ba_2CoTeO_6, J_1 is close to $2J_2$, so that the field range of the 1/3 - plateau state is small.

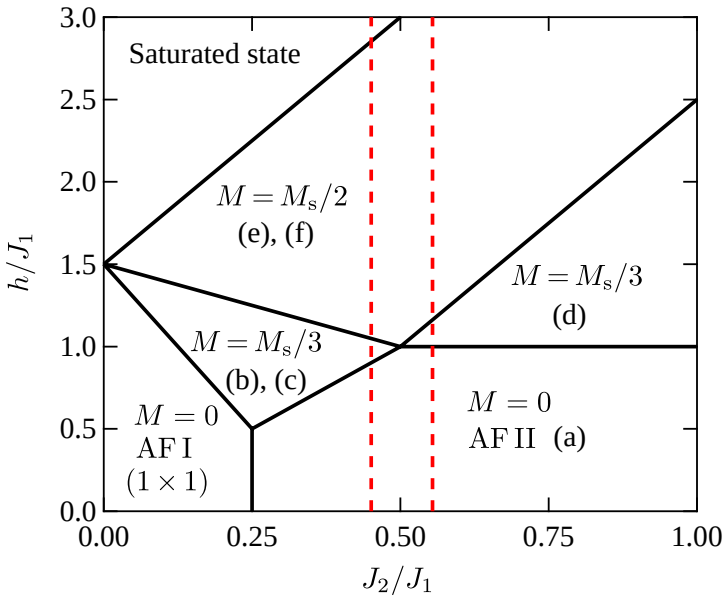

Figure 3.11: Magnetic field (h/J_1) vs J_2/J_1 phase diagram of the $J_1 - J_2$ Ising honeycomb lattice antiferromagnet. Two dashed lines represent the ground states for $J_2/J_1 = 0.45$ and 0.55, which were obtained from the analysis of magnetization curve for $H \parallel c$ in Ba_2CoTeO_6.

3.5 Electron spin resonance (ESR)

We first measure electron paramagnetic resonance (EPR) to estimate the g-factors. Figure 3.12 shows the paramagnetic resonance (EPR) spectra measured for $H \parallel c$ and $H \perp c$ at 40 K ($\gg T_{\mathrm{N1}} = 12$ K) and 190 GHz, using pulsed magnetic fields. A single resonance peak with a linewidth of approximately 1 T is observed for both field directions. The resonance fields of EPR for both field directions are almost the same. This indicates that the EPR signal originates from the Heisenberg-like subsystem A. From the resonance fields, the g-factors of subsystem A are estimated as $g_{\mathrm{A}}^{\parallel} = 3.88$ and $g_{\mathrm{A}}^{\perp} = 3.83$ for $H \parallel c$ and $H \perp c$, respectively. These g-factors are almost the same as those observed in $Ba_3CoSb_2O_9$ [16]. Usually, the g-factor for Co^{2+} in the octahedral environment is strongly anisotropic. Thus, such almost isotropic g-factors observed in $Ba_3CoSb_2O_9$ and Ba_2CoTeO_6 are rare examples.

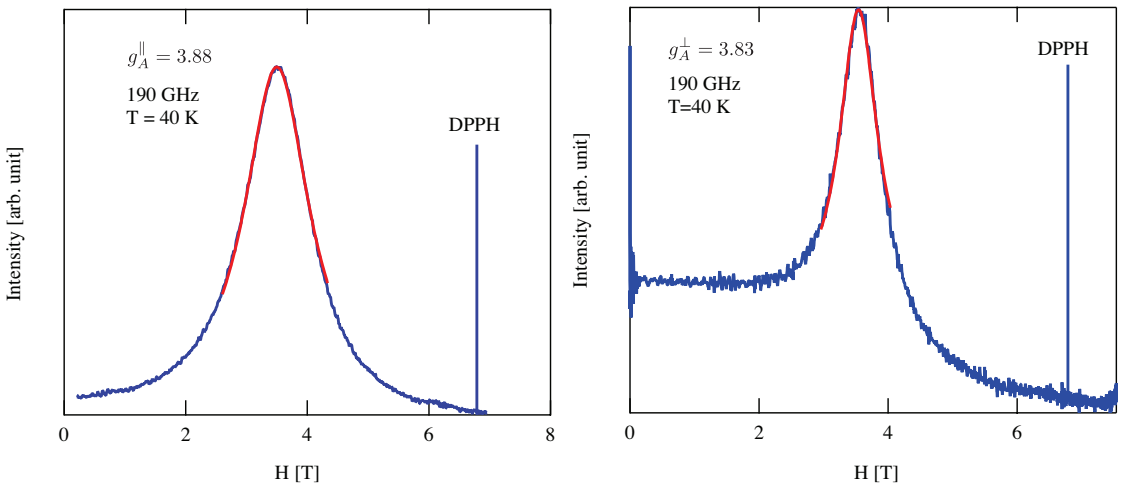

Figure 3.12: EPR absorption spectra in Ba_2CoTeO_6 measured at $\nu = 190$ GHz and $T = 40$ K for (a) $H \parallel c$ and (b) $H \perp c$, using pulsed magnetic fields. Sharp line labeled DPPH indicates the resonance field corresponding to $g = 2$. Red lines are fits using Lorentzian function.

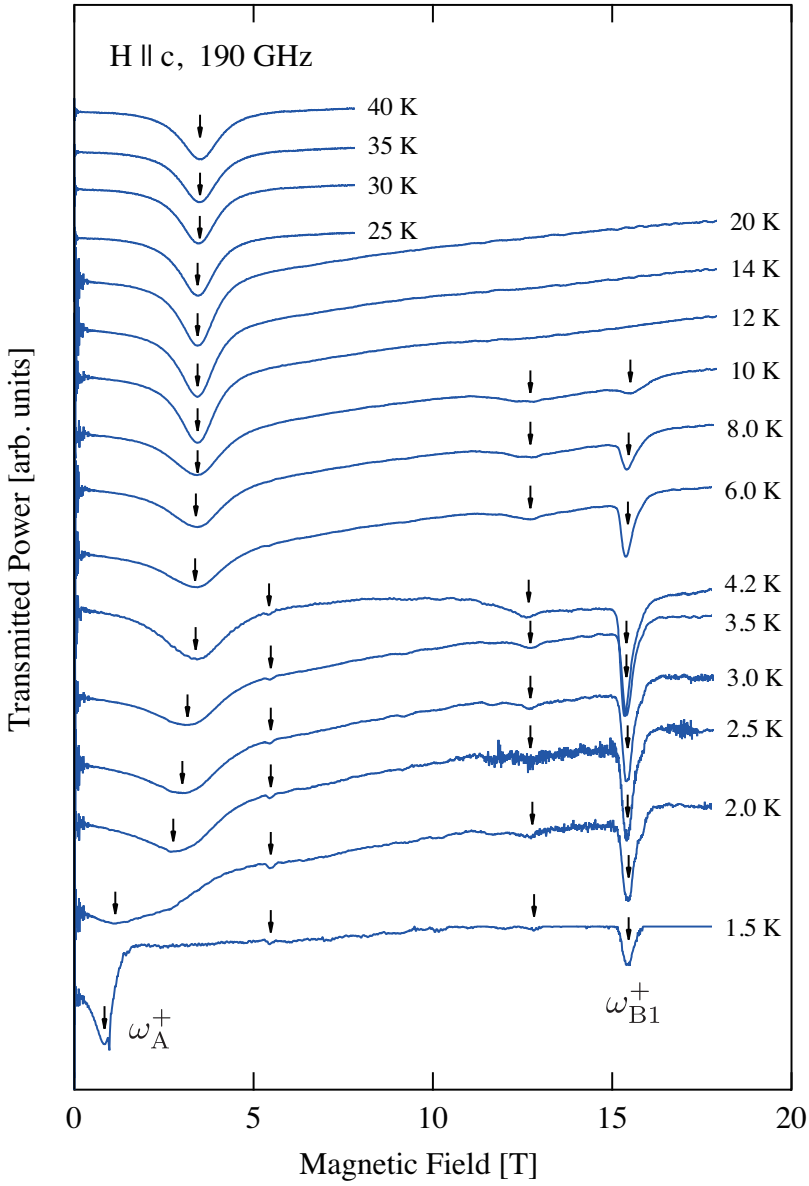

Figure 3.13: ESR spectra of Ba_2CoTeO_6 for $H \parallel c$ measured at various temperatures from 1.8 to 40 K with the frequency of 190 GHz. The vertical axis denotes the detected transmitted power. Arrows indicate resonance fields. The data are arbitrarily shifted in the longitudinal direction for clarity. Strong ESR signals labeled ω_{A}^{+} and ω_{B1}^{+} denote collective and local modes of subsystems A and B, respectively.

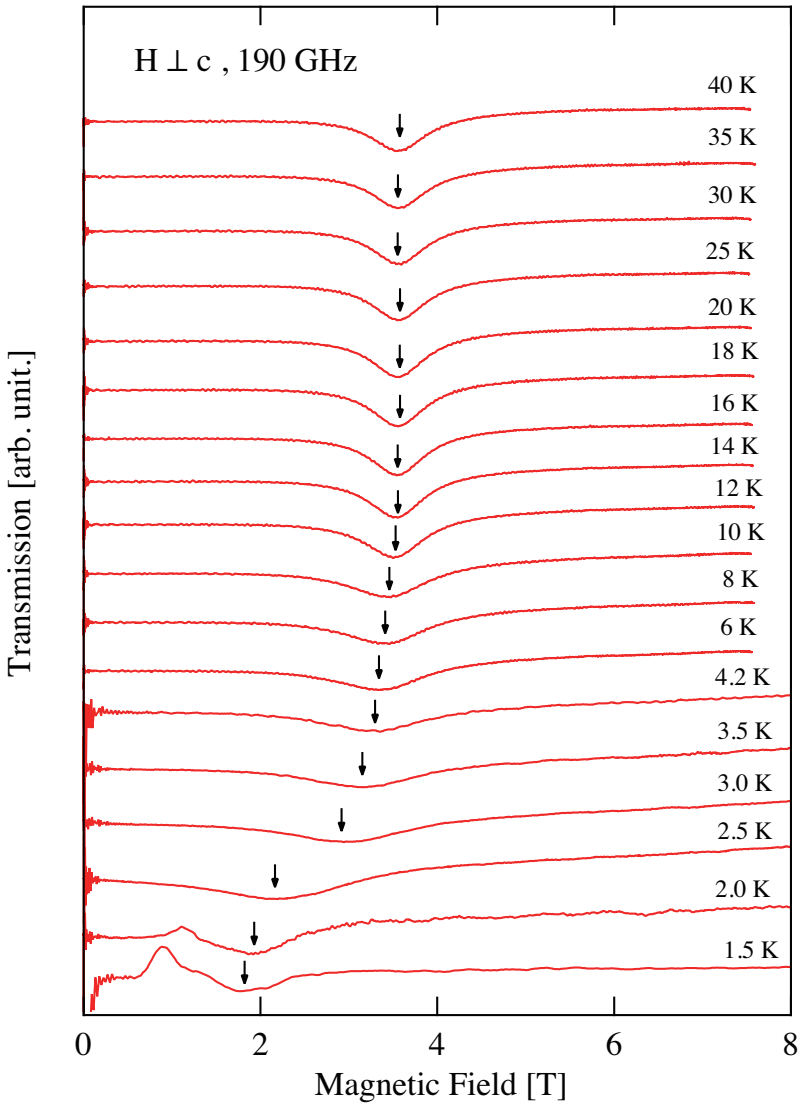

Figure 3.14: (ESR spectra of Ba_2CoTeO_6 for $H \perp c$ measured at various temperatures from 1.8 to 40 K with the frequency of 190 GHz. The vertical axis denotes the detected transmitted power. Arrows indicate resonance fields. The data are arbitrarily shifted in the longitudinal direction for clarity.

Figure 3.13 and 3.14 show the temperature evolution of electron spin resonance (ESR) spectra measured at 190 GHz for $H \parallel c$ and $H \perp c$, respectively, using pulsed magnetic fields. As temperature is decreased below $T_{N1} = 12.0$ K for $H \parallel c$, two peaks appear at $H = 12.5$ and 15.5 T. The resonance signal centered at 15.5 T is strong down to 1.5 K. An additional weak peak appears at $H = 5.5$ T below 6 K. The strong resonance peak

that corresponds to EPR above T_{N1} starts to shift to the low-field side at $T = 3.5$ K, which is just above $T_{N2} = 3.0$ K, and its resonance field decreases to 0.82 T at 1.5 K. For $H \perp c$, the resonance field shifts gradually towards the low-field side down to 3.5 K, with decreasing temperature. Below $T_{N2} = 3.0$ K, the resonance field shifts rapidly towards the low-field side and reaches 1.8 T.

In the present study, we focus on the case for $H \parallel c$, where the spin configuration is symmetric with respect to the magnetic field. Figures 3.15(a) and (b) show examples of ESR spectra measured at several frequencies for $H \parallel c$ using pulsed and static magnetic fields, respectively. These spectra were measured at 1.5 K, which is sufficiently lower than $T_{N2} = 3.0$ K. Absorption signals observed upon sweeping field both up and down were determined as intrinsic resonance signals, which are indicated by vertical arrows in Fig. 3.15. The obtained resonance data are summarized in Fig. 3.16.

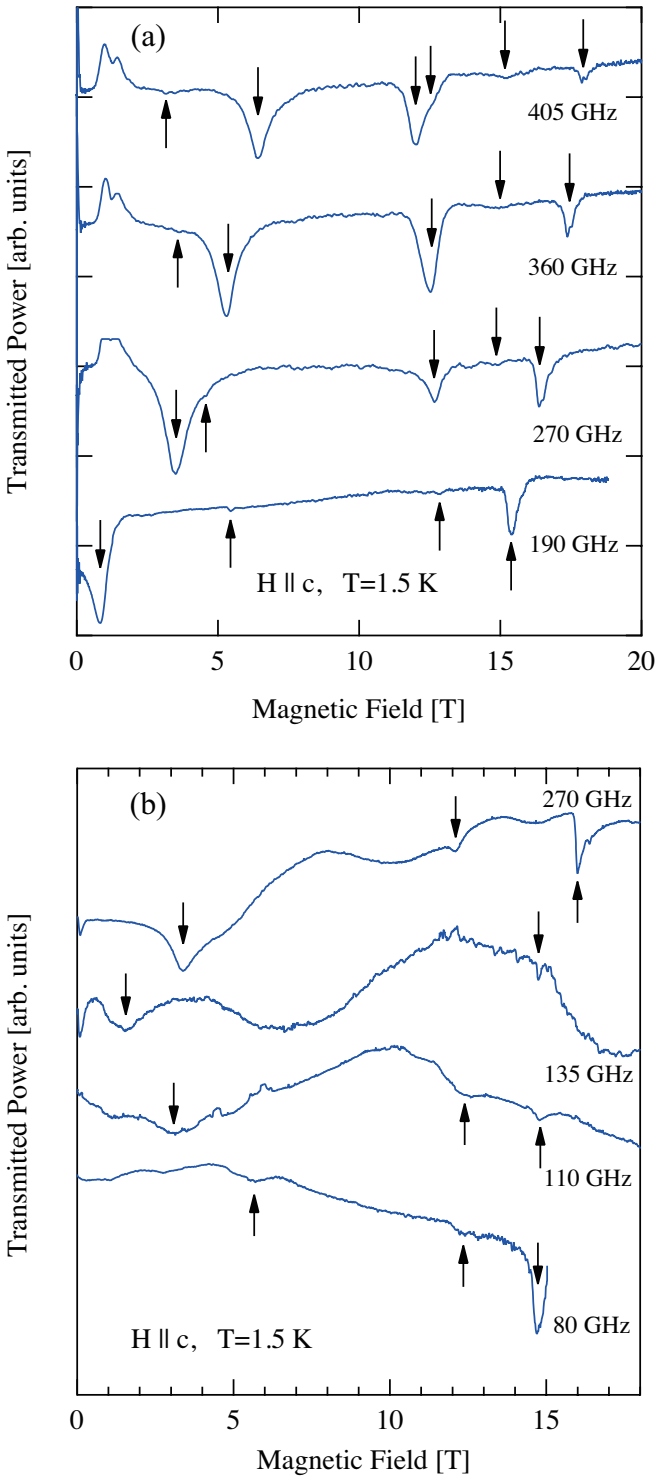

Figure 3.15: Examples of ESR spectra of Ba_2CoTeO_6 measured at several frequencies for $H \parallel c$ using (a) pulsed magnetic fields and (b) static magnetic fields. Resonance data were collected at 1.5 K ($< T_{N2} = 3.0$ K). Vertical arrows indicate resonance fields. The data are arbitrarily shifted in the longitudinal direction for clarity.

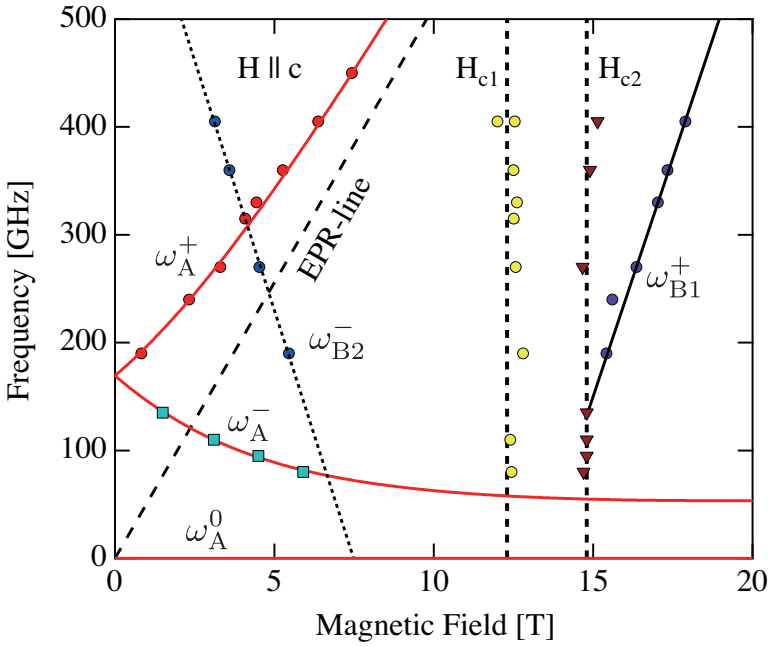

Figure 3.16: Frequency-field diagram of the ESR modes in Ba_2CoTeO_6 for $H \parallel c$. Symbols denote the resonance points obtained at 1.5 K. ω_A^+ and ω_A^- are the collective ESR modes of subsystem A. Red solid curves are fits with Eq. (3.11) based on a six-sublattice model (see text). Red horizontal line is the $\hbar\omega_A^0$ mode with zero frequency. The dashed line is the EPR line described with $g = 3.65$, which is obtained by the fit to the $\omega_A^\pm$ mode with Eq. (3.11). The linear ω_{B1}^+ mode is the single flip of the up spin of subsystem B. The black solid line is the fit by Eq. (3.12). The resonance modes observed at the transition fields H_{c1} and H_{c2} are the critical resonance modes for subsystem B. The weak linear ω_{B2}^- mode is a unknown mode. Thin dotted line is a linear fit to the ω_{B2}^- mode.

Six kinds of resonance modes are observed. Below 8 T, two strong ESR modes that consist of two branches labeled as ω_A^+ and ω_A^- are observed. At zero magnetic field, these two modes appear to be degenerate with an energy gap of approximately 170 GHz. As the magnetic field increases, the energy of the ω_A^+ mode increases and tends to approach the EPR line with $g = 3.88$, whereas the energy of the ω_A^- mode decreases monotonically toward zero. Because the resonance conditions of these two modes are quite similar to those observed in the $S = 1/2$ Heisenberg-like TLAF $Ba_3CoSb_2O_9$ with weak easy-plane anisotropy [16], we can assign the ω_A^+ and ω_A^- modes to the collective excitations in subsystem A.

Two frequency-independent resonance modes are observed at $H = 12.5$ and 14.8

T. Because these two resonance fields are almost the same as the transition fields $H_{c1}^{\parallel} = 12.3$ T and $H_{c2}^{\parallel} = 14.8$ T for subsystem B, these modes are assigned as the critical resonance modes. There are two linear ESR modes labeled as ω_{B1}^{+} and ω_{B2}^{-}, which are observed for $H > H_{c2}^{\parallel}$ and $H < H_{c1}^{\parallel}$, respectively. The intensity of the ω_{B1}^{+} mode is strong. Because the ω_{B1}^{+} and ω_{B2}^{-} appear below T_{N1} and their frequencies are linear in magnetic field, which is characteristic of the resonance in the Ising-like spin system, these two modes are originated from subsystem B.

We first analyze the collective ESR modes ω_{A}^{+} and ω_{A}^{-}, assuming that the triangular layers in subsystem A are weakly coupled by the effective antiferromagnetic interlayer exchange interaction J'. For simplification, we neglect the effect of the coupling between subsystem A and B, because the total magnetization is approximately given by the superposition of magnetizations from magnetically decoupled subsystem A and B, as explained in Sec. 3.3. This is supported from the facts that the paramagnetic resonance of subsystem A observed at $H = 3.5$ T, which is continuously connected to the ω_{A}^{+} mode, is not affected by the ordering of subsystem B at $T_{N1} = 12$ K and the resonance field of the ω_{B1}^{+} mode does not change across $T_{N2} = 3.0$ K, as shown in Fig. 3.13. Based on these assumptions, we describe the magnetic model of subsystem A for $H \parallel c$ as

$$\mathcal{H}_{A} = \sum_{\langle i,j \rangle} \left[J \boldsymbol{S}_i \cdot \boldsymbol{S}_j + \Delta J (S_i^x S_j^x + S_i^y S_j^y) \right] + \sum_{\langle l,m \rangle} J' \boldsymbol{S}_l \cdot \boldsymbol{S}_m - \sum_i g_{A}^{\parallel} \mu_B S_i^z H, \tag{3.10}$$

where J and ΔJ (> 0) are the intralayer exchange interaction and anisotropic exchange interaction of easy-plane type in the layer, respectively. Here, the z-axis is taken to be parallel to the c axis.

The classical ground state of the model of Eq. (3.10) is as follows: In one triangular layer, spins lie in the layer and form the 120° structure. Two neighboring spins along the c axis are antiparallel owing to the antiferromagnetic J'. Therefore, the spin structure is composed of six sublattices. In a finite magnetic field, all the sublattice spins are canted from the triangular layer with the same canting angle. Theory demonstrated

that the dispersion relation of low-energy single magnon excitations in the vicinity of the magnetic Bragg point can be described by linear spin wave theory [39–44]. However, in a large area of the Brillouin zone, the excitation energy is significantly renormalized downward by quantum fluctuations. The ESR excitations corresponds to the excitations at the magnetic Bragg point. Because the dispersion relations of single magnon excitations obtained from linear spin wave theory are equivalent to the solutions of the classical equations of motion for sublattice spins, we calculate the resonance conditions of the collective ESR modes by solving the torque equations. According to the analytical procedure of Ref. [64], we solve the torque equations for the six-sublattice model and obtain the resonance conditions as

$$\begin{aligned}\hbar\omega_{\pm} = &\sqrt{\left(4J' + \frac{9}{2}J + \frac{9}{2}\Delta J\right)\left\{\frac{3\Delta J}{4} + \frac{8J' + 9J + 3\Delta J}{2(4J' + 9J + 3\Delta J)^2}\,(g_{\mathrm{A}}^{\parallel}\mu_{\mathrm{B}}H)^2\right\}} \\ &\pm \frac{9J + 9\Delta J}{8J' + 18J + 6\Delta J}\, g_{\mathrm{A}}^{\parallel}\mu_{\mathrm{B}}H,\end{aligned} \tag{3.11}$$

and $\hbar\omega_{\mathrm{A}}^{0} = 0$. In the $\hbar\omega_{\mathrm{A}}^{\pm}$ modes, sublattice spins, $\boldsymbol{S}_1$, $\boldsymbol{S}_2$ and $\boldsymbol{S}_3$ (or $\boldsymbol{S}_4$, $\boldsymbol{S}_5$ and $\boldsymbol{S}_6$), in a triangular layer precess with the cyclic phase difference by $\Delta\theta_{ij} = \pm 2\pi/3$. Neighboring sublattice spins $\boldsymbol{S}_i$ and $\boldsymbol{S}_{i+3}$ along the c axis precess in phase. The $\hbar\omega_{\mathrm{A}}^{0}$ mode is the zero mode, which corresponds to the global rotation of spins with respect to the magnetic field. Details of the derivation of the resonance conditions of Eq. (3.11) is described in Appendix.

The intralayer exchange constant J was evaluated to be $J/k_{\mathrm{B}} = 20.5\,\mathrm{K}$ from the saturation field $H_{c3}^{\perp} = 37.2$ T for $H \perp c$ and $g_{\mathrm{A}}^{\perp} = 3.83$ using the relation $g\mu_{\mathrm{B}}H_{\mathrm{s}} = 9J/2$ on the assumption of $\Delta J/J \ll 1$ and $J'/J \ll 1$. The magnitude of J in Ba_2CoTeO_6 is somewhat larger than $J/k_{\mathrm{B}} = 18.5$ K in $Ba_3CoSb_2O_9$ [16]. In the analysis, we fixed only the value of J. We treat the g-factor as an adjustable parameter, because no good fit was obtained, hen the g-factor is fixed to $g_{\mathrm{A}}^{\parallel} = 3.88$ obtained from the EPR measurement for $H \parallel c$. Red solid curves in Fig. 3.16 are fits obtained using equation (3.11) with $J'/k_{\mathrm{B}} = 1.6\,\mathrm{K}$, $\Delta J/k_{\mathrm{B}} = 0.86\,\mathrm{K}$ and $g_{\mathrm{A}}^{\parallel} = 3.65$. The agreement between the experimental

and theoretical results is considerably good. Because J' and ΔJ are much smaller than J, we can deduce that subsystem A closely approximates two-dimensional $S = 1/2$ Heisenberg TLAF. These magnetic parameters of Ba_2CoTeO_6 are similar to those observed in $Ba_3CoSb_2O_9$ [16]. The ratio of the easy-plane anisotropy to the intralayer exchange interaction $\Delta J/J$ in subsystem A is somewhat smaller than that in $Ba_3CoSb_2O_9$. This means that the exchange interaction is more isotropic in subsystem A than in $Ba_3CoSb_2O_9$.

The g-factor of $g_{\rm A}^{\parallel} = 3.65$ obtained from the best fit of the collective ESR modes is smaller than $g_{\rm A}^{\parallel} = 3.88$ obtained from the EPR measurement. We infer that the discrepancy arises from the dynamical shift of the resonance field owing to the easy-plane anisotropy ΔJ and the weak interaction between subsystems A and B. The lattice points of subsystem A are located at the centers of the hexagons of subsystem B when projected on the *ab* plane, as shown in Fig. 1.23. Because the ordering of Ising spins of subsystems B do not have the hexagonal symmetry as shown in Fig. 3.10(b), the effective field acting on the subsystem A from subsystem B is not uniform.

Next we analyze the strong $\omega_{\rm B1}^{+}$ mode observed above $H_{\rm c2}^{\parallel} = 14.8$ T. The spin structure for $H > H_{\rm c2}^{\parallel}$ are shown in Figs. 3.10(e) and (f). Because the frequency of the $\omega_{\rm B1}^{+}$ mode increases with increasing magnetic field, this mode is attributed to the flip of up spin in Ising-like subsystem B. The energy of the flip of one up spin is calculated within the framework of $J_1 - J_2$ Ising HLAF as

$$\hbar\omega_{\rm B1}^{+} = g_{\rm B}^{\parallel}\mu_{\rm B}H - \frac{J_1 + 2J_2}{2}, \tag{3.12}$$

where J_1 and J_2 are the nearest and next-nearest neighbor exchange interactions in subsystem B, as shown in Fig. 1.23(c). $g_{\rm B}^{\parallel}$ is the g-factor for $H \parallel c$ in subsystem B. This resonance condition is common to all the up-spins shown in Figs. 3.17. Fitting Eq. (3.12) to the resonance data for the $\omega_{\rm B1}^{+}$ mode, we obtain $g_{\rm B}^{\parallel} = 6.27$ and $(J_1 + 2J_2)/k_{\rm B} = 112$ K. The black solid line in Fig. 3.16 is the fit with these parameters. From Eq. (3.5), the saturation field for $H_{\rm s}^{\parallel}$ is given by

$$g_{\rm B}^{\parallel}\mu_{\rm B}H_{\rm s}^{\parallel} = \frac{3}{2}(J_1 + 2J_2). \tag{3.13}$$

Using $g_{\mathrm{B}}^{\parallel} = 6.27$ and $(J_1{+}2J_2)/k_{\mathrm{B}} = 112$ K, the saturation field is calculated as $H_{\mathrm{s}}^{\parallel}(\mathrm{cal}) = 39.8$ T, which is agreement with the experimental saturation field of $H_{\mathrm{s}}^{\parallel}(\mathrm{exp}) = 39.0$ T.

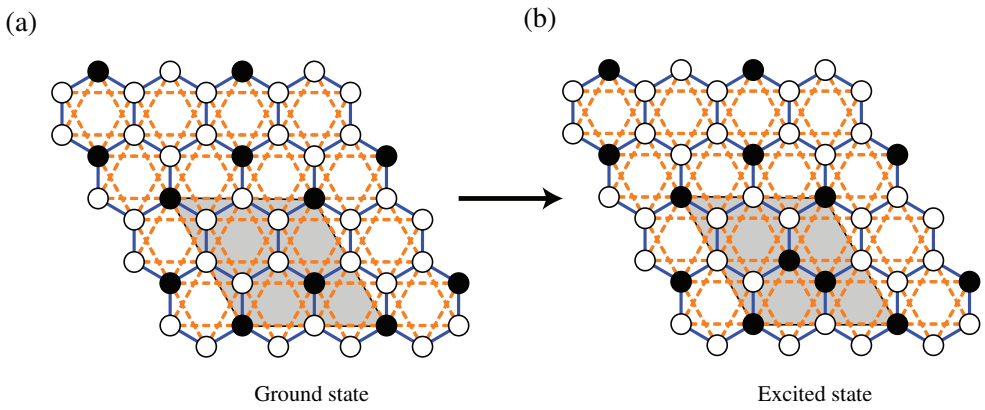

Figure 3.17: (a) Ground state and (b) excited state of the $J_1{-}J_2$ Ising HLAF in the 1/2 - plateau state. The excited state is caused by single flipping of up spin to down spin.

The critical fields $H_{\mathrm{c1}}^{\parallel}$ and $H_{\mathrm{c2}}^{\parallel}$ for $H \parallel c$ are expresseb by Eqs. (3.8) and (3.9). Using Eq. (3.8), $H_{\mathrm{c1}}^{\parallel}(\mathrm{exp}) = 12.3$ T and $(J_1 + 2J_2)/k_{\mathrm{B}} = 112$ K, the exchange constants J_1 and J_2 are evaluated as

$$J_1/k_{\mathrm{B}} = 57.8\,\mathrm{K}, \qquad J_2/k_{\mathrm{B}} = 26.0\,\mathrm{K}, \tag{3.14}$$

for $J_1 \geq 2J_2$. and

$$J_1/k_{\mathrm{B}} = 51.9\,\mathrm{K}, \qquad J_2/k_{\mathrm{B}} = 28.9\,\mathrm{K}, \tag{3.15}$$

for $J_1 < 2J_2$. Substituting these exchange constants in Eq. (3.9), we obtain $H_{\mathrm{c2}}^{\parallel}(\mathrm{cal}) = 14.4$ T, which is consistent with observed value of $H_{\mathrm{c2}}^{\parallel}(\mathrm{exp}) = 14.8$ T. These results indicate that subsystem B can be described by $J_1{-}J_2$ Ising HLAF for $H \parallel c$. For the weak linear ω_{B2}^{-} mode, its origin is not yet identified.

CHAPTER 4

SUMMARY AND FUTURE SCOPE

In this dissertation, we investigated quantum and many-body effects on the static and dynamic magnetic properties in Ba_2CoTeO_6, using single crystals. This compound has a trigonal structure with space group $P\bar{3}m1$, in which Co^{2+} with effective spin-1/2 is surrounded octahedrally by six O^{2-} ions. There are two Co^{2+} sites, Co(1) and Co(2). $Co(1)^{2+}$ ions form a two-dimensional (2D) triangular lattice parallel to the *ab*-plane, while $Co(2)^{2+}$ ions form a double-layered triangular lattice. From crystallographic nature, Ba_2CoTeO_6 is magnetically composed of two subsystems A and B, which are described as a $S = 1/2$ Heisenberg triangular lattice antiferromagnet (TLAF) and a J_1-J_2 Ising honeycomb lattice antiferromagnet (HLAF), respectively.

From the magnetic susceptibility and specific heat measurements, we found that Ba_2CoTeO_6 exhibits two phase transitions, $T_{N1} = 12.0\,\mathrm{K}$ and $T_{N2} = 3.0\,\mathrm{K}$, which correspond to the orderings of subsystems B and A, respectively. We determined the magnetic phase diagrams for $H \parallel c$ and $H \perp c$, as shown in Fig 3.5. The magnetic-field dependence of the phase boundaries related to T_{N2} is very similar to that observed in the $S = 1/2$ Heisenberg TLAF $Ba_3CoSb_2O_9$ with the weak easy-plane anisotropy.

From the analysis of the magnetization curves for $H \parallel c$ and $H \perp c$ obtained by high-field magnetization measurements, it was found that the total magnetization is approximately given by the superposition of magnetizations from magnetically decoupled subsystem A and B. This implies that the coupling between the two subsystems is weak. Heisenberg-like subsystem A exhibits a magnetization plateau at one-third of the saturation magnetization for $H \perp c$, which is a symbolic quantum effect in small spin Heisenberg TLAFs caused by the quantum order-by-disorder. The magnetization curve for $H \perp c$ of subsystem A is in good quantitative agreement with the theoretical result for

the $S = 1/2$ Heisenberg TLAF. Because of weak easy-plane anisotropy and antiferromagnetic interlayer exchange interaction, subsystem A displays no magnetization plateau for $H \parallel c$. The magnetization process of subsystem A is very similar to that observed in $Ba_3CoSb_2O_9$.

For $H \parallel c$, Ising-like subsystem B shows three-step metamagnetic transitions at $H_{c1}^{\parallel} = 12.3$ T, $H_{c2}^{\parallel} = 14.8$ T, and $H_{s}^{\parallel} = 39.0$ T with magnetization plateaus at zero, one-third and one-half of the saturation magnetization. This stepwise magnetization process can be understood within the framework of $J_1 - J_2$ Ising HLAF. On the basis of Kanamori theory, we discussed the field-induced successive transitions and spin structures. We showed that the spin states of the 1/2 - and 1/3 - plateaus for $J_1 \geq 2J_2$ are infinitely degenerate. We also presented the ground-state phase diagram of the $J_1 - J_2$ Ising HLAF model in magnetic fields.

Dynamical properties of Ba_2CoTeO_6 have been investigated via electron spin resonance (ESR). Below T_{N2}, we observed collective ESR modes for $H \parallel c$, which are characteristic of the triangular-lattice Heisenberg antiferromagnet with the small easy-plane anisotropy. We also observed a local excitation mode, which can be assigned as the single flip of Ising-like spin of subsystem B. The collective mode of subsystem A composed of two branches is such that three sublattice spins forming the 120° structure in a triangular layer precess with the cyclic phase difference by $\pm 2\pi/3$. The strong local excitation mode of Ising-like subsystem B observed for $H > H_{c2}^{\parallel}$ can be interpreted as the single flip of up-spin. From a detailed analysis of the collective and local ESR modes, combined with the magnetization process, we determined the magnetic parameters of subsystems A and B, and confirmed that subsystems A and B are almost decoupled. From the obtained magnetic parameters, it was found that the ratio of the easy-plane anisotropy to the intralayer exchange interaction $\Delta J/J$ in subsystem A of Ba_2CoTeO_6 is somewhat smaller than that in $Ba_3CoSb_2O_9$, which means that the exchange interaction is more isotropic in subsystem A than in $Ba_3CoSb_2O_9$.

From experimental results, we concluded that spins in subsystem B are ordered

first at $T_{N1} = 12.0$ K, and then spins in subsystem A are ordered at $T_{N2} = 3.0$ K. However, the spin structures are not verified experimentally. Within the framework of J_1-J_2 Ising HLAF, we discussed the spin structures of subsystem B in magnetic fields and showed two possible set of parameters for $J_1 \geq 2J_2$ and $J_1 < 2J_2$. If we know the spin structure in magnetic fields, we can determine which condition is realized in Ba_2CoTeO_6. Thus, neutron diffraction experiment in zero and magnetic fields are necessary.

We also discussed the some high-field spin states are infinitely degenerate. These degeneracies can be lifted by the quantum fluctuation that originates from the finite transverse component of the exchange interactions. It is interesting to investigate theoretically how these plateau states change with increasing the magnitude of the transverse component. For $S = 1/2$ J_1-J_2 Heisenberg HLAF, exotic quantum ground states were predicted, as shown in Fig. 1.19 [23]. It is of great interest to verify these quantum states in related materials.

For $H \perp c$, additional transition was observed $H_{c4}^{\perp} = 45.9$ T, which is higher than the saturation field $H_{c3}^{\perp} = 37.2$ T of subsystem A. We speculate that this transition ascribed to the quantum phase transition owing to the transverse magnetic field applied to the J_1-J_2 Ising HLAF. Elucidating the origin of the transition at $H_{c4}^{\perp}$ is future problem.

Recently, inelastic neutron scattering was performed on $Ba_3CoSb_2O_9$, which is considered to be the best realization of the $S = 1/2$ Heisenberg TLAF. Surprisingly, the results were significantly different from current theory. It was found that the excitation spectra have a three-stage energy structure, as shown in Fig. 1.17. The lowest first stage is composed of dispersion branches of single-magnon excitations. The second and third stages are dispersive continua accompanied by columnar continuum extending above energy that is six times larger than the exchange interaction. It is considered that these unusual magnetic excitations arise from the quantum many-body effect yet to be revealed. This results strongly indicate the necessity of a new theoretical framework. It is important to establish the magnetic excitations in the $S = 1/2$ Heisenberg TLAF.

Thus, inelastic neutron scattering experiment using different compound is needed. From this study, we found that the magnetic model of subsystem A in Ba_2CoTeO_6 is close to the $S = 1/2$ Heisenberg TLAF. Therefore, Ba_2CoTeO_6 is suitable for investigating the magnetic excitations in the $S = 1/2$ Heisenberg TLAF. Inelastic neutron scattering on Ba_2CoTeO_6 is of great interest.

APPENDICES

APPENDIX A

Effective spin of Co^{2+} at low temperature

Considering Ba_2CoTeO_6 crystal structure, Co^{2+} ion is under an octahedral environment coordinated by six O^{2-} ions. For an independent Co^{2+} ion, there are seven electrons in 3d orbital ($3d^7$) with quantum numbers, L= 3 and $S = 3/2$ in the ground state. When Co^{2+} is in an octahedral environment, energy states splits into three energy levels with two triplet states and one singlet state. In this case, it is enough to consider only the lowest orbital triplet state [2].

$$\left.\begin{aligned} |-1\rangle &= \sqrt{\frac{5}{6}}\,\phi_2 + \frac{1}{\sqrt{6}}\,\phi_{-1}, \\ |0\rangle &= \frac{2}{3}\,\phi_0 - \frac{\sqrt{5}}{3\sqrt{2}}\,(\phi_2 - \phi_{-1}), \\ |+1\rangle &= \sqrt{\frac{5}{6}}\,\phi_{-1} - \frac{1}{\sqrt{6}}\,\phi_1, \end{aligned}\right\} \tag{1}$$

$$\langle \pm 1|L_z|\pm 1\rangle = \mp\frac{3}{2} \tag{2}$$

$$\langle 0|L_z|0\rangle = 0 \tag{3}$$

Considering the lowest orbital triplet state, the splitting of this state is caused by spin-orbit coupling and trigonal distortion of the octahedron, in which they act as perturbations. The parameter δ and the parameter λ denote trigonal distortion and spin-orbit coupling constants, respectively. The perturbation hamiltonian can be described as following

$$\mathcal{H}' = \mathcal{H}'_{SO} + \mathcal{H}'_{(trig)} \tag{4}$$

$$\mathcal{H}' = -\frac{3}{2}\lambda(\boldsymbol{l}\cdot\boldsymbol{S}) - \delta\{(l_z)^2 - 2/3\} \tag{5}$$

$$\begin{aligned}\langle 0, m_s|V_{(trig)}|0, m_s\rangle &= 2\delta/3\\ \langle \pm 1, m_s|V_{(trig)}|\pm 1, m_s\rangle &= -\delta/3\end{aligned} \tag{6}$$

$$\mathcal{H}'_{SO} = A(\boldsymbol{l}\cdot\boldsymbol{S}) = A(\boldsymbol{l_x S_x} + \boldsymbol{l_y S_y} + \boldsymbol{l_z S_z}) \tag{7}$$

$$\begin{aligned}\mathcal{H}'_{SO} =& A\left(\frac{(\boldsymbol{l}_+ + \boldsymbol{l}_-)(\boldsymbol{S}_+ + \boldsymbol{S}_-)}{4} - \frac{(\boldsymbol{l}_+ - \boldsymbol{l}_-)(\boldsymbol{S}_+ - \boldsymbol{s}_-)}{4} + \boldsymbol{l_z S_z}\right)\\ =& A\left(\frac{\boldsymbol{l}_+\boldsymbol{S}_+ + \boldsymbol{l}_-\boldsymbol{S}_-}{2} + \boldsymbol{l_z S_z}\right)\end{aligned} \tag{8}$$

$$\langle l', m'_l, S', m'_s|\boldsymbol{l}_+\boldsymbol{S}_-|l, m_l, S, m_s\rangle = \langle l', m'_l|\boldsymbol{l}_+|l, m_l\rangle\langle S', m'_S|\boldsymbol{S}_-|S, m_s\rangle \tag{9}$$

These matrix elements can be estimated using [65]

$$\langle k', m'_k|\boldsymbol{k}_+|k, m_k\rangle = \hbar\sqrt{k(k+1) - m_k(m_k+1)}\delta_{kk}, \delta_{m_k, m'_k = m_k+1} \tag{10}$$

$$\langle k', m'_k|\boldsymbol{k}_-|k, m_k\rangle = \hbar\sqrt{k(k+1) - m_k(m_k-1)}\delta_{kk}, \delta_{m_k, m'_k = m_k-1} \tag{11}$$

$$\langle k', m'_k|\boldsymbol{k_z}|k, m_k\rangle = \hbar m_k\delta_{kk}, \delta_{m_k, m'_k} \tag{12}$$

	$\lvert -1, \frac{3}{2}\rangle$	$\lvert 0, \frac{1}{2}\rangle$	$\lvert 1, -\frac{1}{2}\rangle$	$\lvert 0, \frac{3}{2}\rangle$	$\lvert 1, \frac{1}{2}\rangle$	$\lvert 1, \frac{3}{2}\rangle$
$\langle -1, \frac{3}{2}\rvert$	$-\frac{1}{3}\delta + \frac{9}{4}\lambda'$	$-\frac{9}{2}(1/\sqrt{6})\lambda'$	0	0	0	0
$\langle 0, \frac{1}{2}\rvert$	$-\frac{9}{2}(1/\sqrt{6})\lambda'$	$\frac{2}{3}\delta$	$-(3/\sqrt{2})\lambda'$	0	0	0
$\langle 1, -\frac{1}{2}\rvert$	0	$-(3/\sqrt{2})\lambda'$	$-\frac{1}{3}\delta + \frac{3}{4}\lambda'$	0	0	0
$\langle 0, \frac{3}{2}\rvert$	0	0	0	$\frac{2}{3}\delta$	$-\frac{9}{2}(1/\sqrt{6})\lambda'$	0
$\langle 1, \frac{1}{2}\rvert$	0	0	0	$-\frac{9}{2}(1/\sqrt{6})\lambda'$	$-\frac{1}{3}\delta - \frac{3}{4}\lambda'$	0
$\langle 1, \frac{3}{2}\rvert$	0	0	0	0	0	$-\frac{1}{3}\delta + \frac{9}{4}\lambda'$

Table 1: Matrix elements of the Hamiltonian in equation (5) for $\langle l_z, S_z|\mathcal{H}'|l_z, S_z\rangle$. The table was adapted from Ref. [2]

The energy eigenvalues and eigenstates corresponding to this Hamiltonian are shown in Table 1.

$m = l_z + S_z$	$\|l_z, m_z\rangle$	Eigenvalue
5/2	$\|1, 3/2\rangle$	E_l
3/2	$\|1, 1/2\rangle$, $\|0, 3/2\rangle$	${E_q}^+$, ${E_q}^-$
1/2	$\|1, -1/2\rangle$, $\|0, 1/2\rangle$, $\|-1, 3/2\rangle$	${E_c}^{(0)}$, ${E_c}^{(1)}$, ${E_c}^{(2)}$

Table 2: Eigenvalues and magnetic moments of Co^{2+} spin in octahedral environment while considering spin-orbit coupling and trigonal distortion of octahedron as perturbations

$$\begin{aligned}
\frac{E_l}{\lambda'} &= -\frac{\delta}{3\lambda'} - \frac{9}{4}, \\
\frac{E_q^{\pm}}{\lambda'} &= \frac{\delta}{6\lambda'} - \frac{3}{8} \pm \frac{1}{2}\sqrt{\left(\frac{\delta}{\lambda'}\right)^2 + \frac{3\delta}{2\lambda'} + \frac{225}{16}}, \\
\frac{E_c^{(i)}}{\lambda'} &= -\frac{\delta}{3\lambda} + \frac{3}{4}\left(x^{(i)} + 3\right) \ (i = 0, 1, 2),
\end{aligned} \tag{13}$$

where ($x^{(i)}$ is defined by

$$\frac{\delta}{\lambda'} = \frac{3}{4}\left(x^{(i)} + 3\right) - \frac{9}{2x^{(i)}} - \frac{6}{x^{(i)} + 2} \tag{14}$$

The eigenvalues are classified as: one linear E_l ($m = \pm\frac{5}{2}$), two quadratics ${E_q}^+$, ${E_q}^-$ ($m = \pm\frac{3}{2}$) and three cubics ${E_c}^{(0)}$, ${E_c}^{(1)}$, ${E_c}^{(2)}$ ($m = \pm\frac{1}{2}$). All energy eigenvalues are plotted into the graph displayed in figure 1.1 as a function of δ/λ. Since the matrix elements of $|l_z, m_z\rangle$ are identical to those in $|-l_z, -m_z\rangle$, energy levels are doubly degenerate. This doubly degenerate state is called Kramer's doublet. The doublet state with lowest energy level is ${E_c}^{(0)}$.

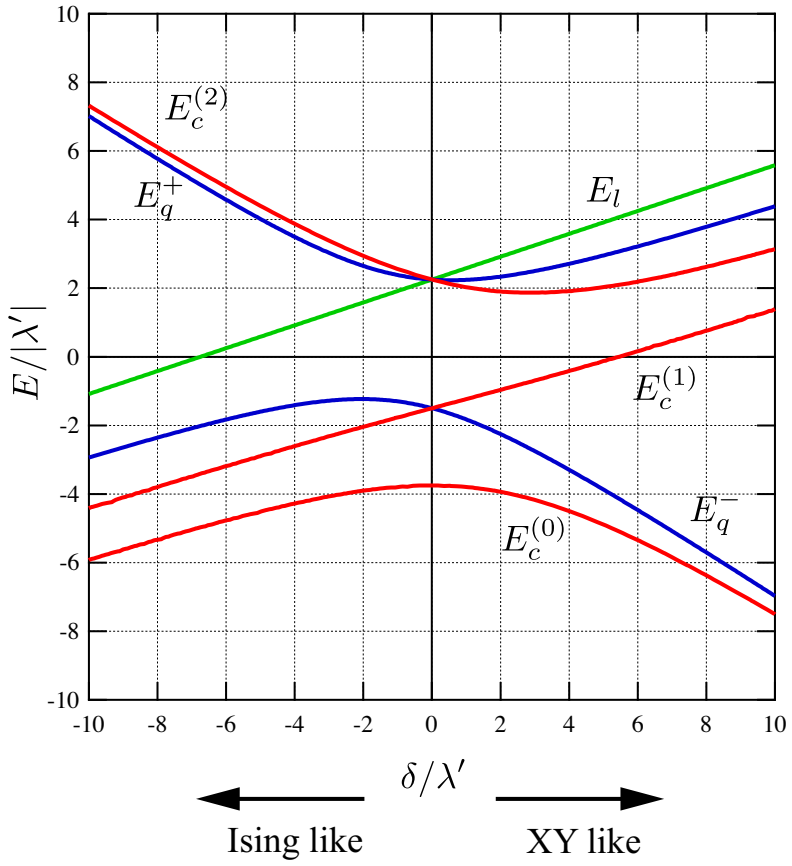

Figure 1: Energy levels of Co^{2+} spin in octahedral environment where the splitting is caused by spin-orbit coupling and trigonal distortion

Wave function of the lowest doublet state is indicated by $\psi_{\pm}^{(0)}$. The expression of this wavefunction can be written as

$$\psi_{\pm}^{(0)} = c_1|\mp 1, \pm 3/2\rangle + c_2|0, \pm 1/2\rangle + c_3|\pm 1, \mp 1/2\rangle \tag{15}$$

We can assume that all states mentioned above can be negligible except the ground state doublets ($E_c^{(0)}$) in case the temperature is below $|\lambda|/k_{\rm B} \simeq 250$ K. Thus, the true spin $\boldsymbol{S}$= 3/2 can be replaced by S^z and $S^{\pm}$ as described below

$$\langle\psi_{\pm}^{(0)}|S^z|\psi_{\pm}^{(0)}\rangle = \pm\frac{1}{2}(3c_1^2 + c_2^2 - c_3^2) = \pm\frac{1}{2}p \tag{16}$$

$$\langle\psi_{\pm}^{(0)}|S^{\pm}|\psi_{\mp}^{(0)}\rangle = 2(\sqrt{3}c_1c_3 + c_2^2) = q \tag{17}$$

$$S^x = qs^x, \quad S^y = qs^y, \quad S^z = ps^z \tag{18}$$

From the equations 16, 17 and 18, we can clearly see that the fictitious spin of Co^2+ is equal 1/2.

According to [2], and [67], anisotropic g-factors have been estimated. In case the magnetic field is applied along z axis (The principal axis of the octahedron), the splitting condition, $g\mu_B S_z$ can be written as

$$\langle\psi_{\pm}^{(0)}| - (3/2)l^z + 2S^z|\psi_{\mp}^{(0)}\rangle\mu_B H \tag{19}$$

g-factor where magnetic field is applied to the z axis can be described as

$$g^{\parallel} = 9a_1^2 + 2a_2^2 - 5a_3^2 \tag{20}$$

Similarly, in the case magnetic field is applied to the ab-plane. g-factor can be described as

$$g^{\perp} = 4a_2^2 + (4\sqrt{3}a_1 - 3\sqrt{2}a_2)a_3 \tag{21}$$

g-factor in octahedral environment of Co^2+ is larger than ordinary g and becomes anisotropic [2, 66, 67]. However, in the case trigonal crystalline field is absent (δ=0), the effective exchange interaction is Heisenberg model, and g-factor becomes isotropic.

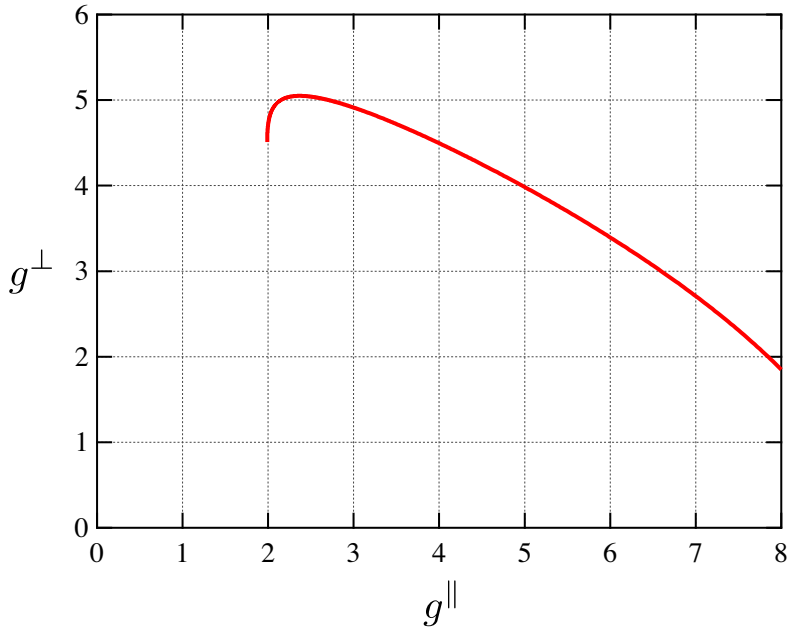

Figure 2: Relationship between $g^{\parallel}$ and $g^{\perp}$ of Co^{2+} octahedron [2, 66, 67]

APPENDIX B

Field-driven ground states of J_1-J_2 Ising-like Honeycomb lattice antiferromagnet

According to J_1-J_2 Ising-like antiferromagnet, Hamiltonian of this system can be described as

$$\mathcal{H} = \frac{1}{2}\sum_{i,k,\rho} J_k\ \sigma(i)\ \sigma(i+\rho_k) - H\sum_i \sigma(i) \tag{22}$$

σ = Ising spin

ρ = Vectors connecting a spin to its interacting neighbors

J_k = it is positive when interaction is antiferromagnet

For $m = 0$

$$\begin{aligned} J_k\ \sigma_i\ \sigma_j &= J_k\ (2S_i^z)(2S_j^z) \\ &= 4J_k\ S_i^z\ S_j^z \\ &= \tilde{J}_k\ S_i^z\ S_j^z\ ;\ \tilde{J}_k = \ 4J_k \end{aligned} \tag{23}$$

Considering magnetic structures of HLAF as shown in figure 3.10, energy of each candidate ground state can be described as

Structure (a)

$$\begin{aligned} E^{(a)} &= \big(\frac{1}{2}\big)\big(4\times\frac{1}{4}\big(-3\tilde{J}_1\frac{1}{4}+\tilde{J}_2\frac{1}{4}\big)+\big(-3\tilde{J}_1\frac{1}{4}+6\tilde{J}_2\frac{1}{4}\big)\big) \\ &= -\frac{3}{4}\tilde{J}_1+\frac{3}{2}\tilde{J}_2 \\ \mathcal{E}^{(a)} &= \frac{1}{2}E^{(a)} \\ \mathcal{E}^{(a)} &= -\frac{3}{8}\tilde{J}_1+\frac{3}{4}\tilde{J}_2 \end{aligned} \tag{24}$$

Structure (b)

$$\begin{aligned} E^{(b)} &= (\frac{1}{4})(4 \times \frac{1}{4}(-\tilde{J}_1\frac{1}{4} - 2\tilde{J}_2\frac{1}{4}) + (-\tilde{J}_1\frac{1}{4} - 2\tilde{J}_2\frac{1}{4}) \\ &\quad + 2 \times \frac{1}{2}(-\tilde{J}_1\frac{1}{4} - 2\tilde{J}_2\frac{1}{4}) + (-\tilde{J}_1\frac{1}{4} - 2\tilde{J}_2\frac{1}{4})) \\ &= (\frac{1}{4})(-\frac{4}{4}\tilde{J}_1 - \frac{8}{4}\tilde{J}_2) \\ &= (-\frac{1}{4}\tilde{J}_1 - \frac{2}{4}\tilde{J}_2 \\ \mathcal{E}^{(b)} &= -\frac{1}{8}\tilde{J}_1 - \frac{1}{4}\tilde{J}_2 \end{aligned} \tag{25}$$

Structure (c)

$$\begin{aligned} E^{(c)} &= (\frac{1}{6})(4 \times \frac{1}{4}(-3\tilde{J}_1\frac{1}{4} - 2\tilde{J}_2\frac{1}{4}) \\ &= +(4 \times \frac{1}{2}(+\tilde{J}_1\frac{1}{4} + 2\tilde{J}_2\frac{1}{4} + (-\tilde{J}_1\frac{1}{4} - 2\tilde{J}_2\frac{1}{4}) \\ &= +2 \times \frac{1}{2}(-\tilde{J}_1\frac{1}{4} - 2\tilde{J}_2\frac{1}{4}) + (-\tilde{J}_1\frac{1}{4} - 2\tilde{J}_2\frac{1}{4})) \\ &= (\frac{1}{4})(-\frac{4}{4}\tilde{J}_1 - \frac{8}{4}\tilde{J}_2) \\ &= (-\frac{1}{4}\tilde{J}_1 - \frac{2}{4}\tilde{J}_2 \\ \mathcal{E}^{(c)} &= -\frac{1}{8}\tilde{J}_1 - \frac{1}{4}\tilde{J}_2 \end{aligned} \tag{26}$$

Structure (d)

$$\begin{aligned} E^{(d)} &= (\frac{1}{12})(4 \times \frac{1}{4}(-3\tilde{J}_1\frac{1}{4} - 6\tilde{J}_2\frac{1}{4}) \\ &= +(4 \times \frac{1}{2}(-\tilde{J}_1\frac{1}{4} + 4\tilde{J}_2\frac{1}{4}) + (2 \times \frac{1}{2}(+\tilde{J}_1\frac{1}{4} + 2\tilde{J}_2\frac{1}{4}) \\ &\quad + (-3\tilde{J}_1\frac{1}{4} - 2\tilde{J}_2\frac{1}{4}) + (2 \times (-3\tilde{J}_1\frac{1}{4})) \\ &\quad + (2 \times (-\tilde{J}_1\frac{1}{4} + 4\tilde{J}_2\frac{1}{4})) + (\tilde{J}_1\frac{1}{4}) \\ &\quad + (+\tilde{J}_1\frac{1}{4} - 2\tilde{J}_2\frac{1}{4}) + (\tilde{J}_1\frac{1}{4}) - (\frac{8-4}{12})h \\ &= (\frac{1}{12})(-\frac{12}{4}\tilde{J}_1 + \frac{8}{4}\tilde{J}_2) - \frac{h}{3} \\ &= (\frac{1}{12})(-3\tilde{J}_1 + 2\tilde{J}_2) - \frac{h}{3} \\ \mathcal{E}^{(d)} &= -\frac{1}{24}(3\tilde{J}_1 - 2\tilde{J}_2) - \frac{h}{6} \end{aligned} \tag{27}$$

Structure (e)

$$\begin{aligned} E^{(e)} &= \big(\frac{1}{6}\big)\big(4\times\frac{1}{4}\big(-3\tilde{J}_1\frac{1}{4}-6\tilde{J}_2\frac{1}{4}\big) \\ &\quad +\big(4\times\frac{1}{2}\big(\tilde{J}_1\frac{1}{4}+0\big)+\big(\tilde{J}_1\frac{1}{4}+0\big)\big) \\ &\quad +\big(2\times\big(\tilde{J}_1\frac{1}{4}+0\big)\big)+\big(-3\tilde{J}_1\frac{1}{4}-6\tilde{J}_2\frac{1}{4}\big)-\big(\frac{4-2}{6}\big)h \\ &= \big(\frac{1}{6}\big)\big(\frac{2}{4}\tilde{J}_1-\frac{12}{4}\tilde{J}_2\big)-\frac{h}{3} \\ &= \big(\frac{1}{12}\big)\big(\tilde{J}_1-6\tilde{J}_2\big)-\frac{h}{3} \\ \mathcal{E}^{(e)} &= -\frac{1}{24}\big(\tilde{J}_1-6\tilde{J}_2\big)-\frac{h}{6} \end{aligned} \tag{28}$$

Structure (f)

$$\begin{aligned} E^{(f)} &= \big(\frac{1}{8}\big)\big(4\times\frac{1}{4}\big(-3\tilde{J}_1\frac{1}{4}-6\tilde{J}_2\frac{1}{4}\big)\big) \\ &\quad +\big(4\times\frac{1}{2}\big(\tilde{J}_1\frac{1}{4}+2\tilde{J}_2\frac{1}{4}\big)\big)+\big(4\times\big(\tilde{J}_1\frac{1}{4}+2\tilde{J}_2\frac{1}{4}\big)\big) \\ &\quad +\big(-3\tilde{J}_1\frac{1}{4}-6\tilde{J}_2\frac{1}{4}\big)-\big(\frac{6-2}{8}\big)h \\ &= -\frac{h}{2} \\ \mathcal{E}^{(f)} &= -\frac{h}{4} \end{aligned} \tag{29}$$

Structure (g)

$$\begin{aligned} E^{(g)} &= \big(\frac{1}{16}\big)\big(4\times\frac{1}{4}\big(-3\tilde{J}_1\frac{1}{4}-6\tilde{J}_2\frac{1}{4}\big) \\ &\quad +\big(8\times\frac{1}{2}\big(\tilde{J}_1\frac{1}{4}+2\tilde{J}_2\frac{1}{4}\big)+\big(3\times\big(-3\tilde{J}_1\frac{1}{4}-6\tilde{J}_2\frac{1}{4}\big)\big) \\ &\quad +\big(8\times\big(\tilde{J}_1\frac{1}{4}+2\tilde{J}_2\frac{1}{4}\big)\big)-\big(\frac{12-4}{16}\big)h \\ &= -\frac{h}{2} \\ \mathcal{E}^{(g)} &= -\frac{h}{4} \end{aligned} \tag{30}$$

$$E = E_F + 2m(H - \sum_k z_k\ J_k) + 4\sum_k p_k\ J_k \tag{31}$$

E_F = energy of ferromagnetic state

m = total number of negative spins

z_k = number of k^{th} interacting neighbors

p_k = number of J_k interaction lines connecting two negative spins

All the energy states mentioned above can be illustrated to see ground-state phase diagram as shown in figure 3

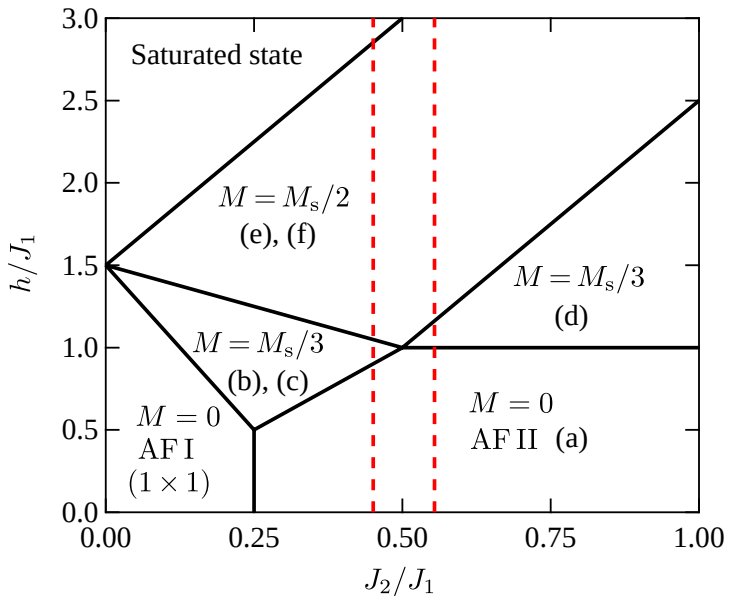

Figure 3: Ground state phase diagram of the J_1-J_2 Ising honeycomb lattice antiferromagnet at varied magnetic fields. The dashed lines represent the ground states for $J_1/J_2 \simeq 0.45$ and 0.55, which were obtained from Ba_2CoTeO_6 magnetization curve for $H \parallel c$

APPENDIX C

Resonance conditions for Heisenberg-like Triangular lattice antiferromagnet for $H \parallel c$

Referred to [64] and [66], the resonance condition has been derived when an applied magnetic field ($< H_c$) is perpendicularly to the easy plane of the triangular lattice antiferromagnet. Six sublattices has been considering, where the sublattice magnetizations are canted from the triangular layer with the same canting angle[39–44]. It can be described by this Hamiltonian

$$\begin{aligned}\mathcal{H} =& J \sum_{<i,j>} \sum_{m} \boldsymbol{S}_{im} \cdot \boldsymbol{S}_{jm} + \Delta J \sum_{<i,j>} \sum_{m} (S^x_{im} S^x_{jm} + S^y_{im} S^y_{jm}) \\ &+ J' \sum_{i} \sum_{m} \boldsymbol{S}_{im} \cdot \boldsymbol{S}_{im+1} - \sum_{i} \sum_{m} g\mu_{\mathrm{B}} \boldsymbol{S}_{im} \cdot \boldsymbol{H}\end{aligned} \tag{32}$$

This applied magnetic field is smaller than the phase transition field (H_c), in which magnetic configuration changes from the umbrella structure to the coplanar-2 structure. The magnetizations of the six sublattices are shifted from the easy plane by the angle ϕ as shown in figure 4. Magnetization of six sublattices can be defined as following.

$$\left.\begin{aligned}\boldsymbol{M_1} =& M_0 \left(0, \quad \cos\phi, \quad \sin\phi \right) \\ \boldsymbol{M_2} =& M_0 \left(-\tfrac{\sqrt{3}}{2}\cos\phi, \quad -\tfrac{1}{2}\cos\phi, \quad \sin\phi \right) \\ \boldsymbol{M_3} =& M_0 \left(-\tfrac{\sqrt{3}}{2}\cos\phi, \quad -\tfrac{1}{2}\cos\phi, \quad \sin\phi \right) \\ \boldsymbol{M_4} =& M_0 \left(0, \quad -\cos\phi, \quad \sin\phi \right) \\ \boldsymbol{M_5} =& M_0 \left(-\tfrac{\sqrt{3}}{2}\cos\phi, \quad \tfrac{1}{2}\cos\phi, \quad \sin\phi \right) \\ \boldsymbol{M_6} =& M_0 \left(-\tfrac{\sqrt{3}}{2}\cos\phi, \quad \tfrac{1}{2}\cos\phi, \quad \sin\phi \right)\end{aligned}\right\} \tag{33}$$

New coordinates are defined with the direction of magnetization of each sublattice in z' axis. The matrix transformation of the coordinate systems can be described as

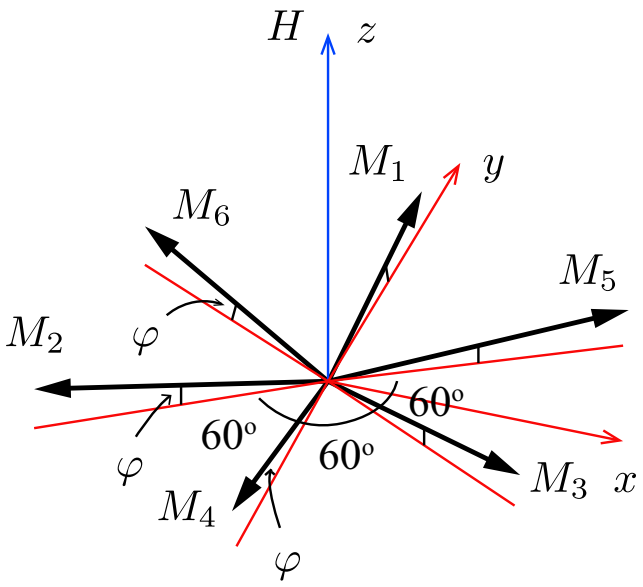

Figure 4: Geometrical magnetization configuration of six sublattices of triangular lattice antiferromagnet for $H \parallel c$. This figure is adapted from Ref. [64]

$$\boldsymbol{R_1} = \begin{pmatrix} 1 & 0 & 0 \\ 0 & \sin\phi & -\cos\phi \\ 0 & \cos\phi & \sin\phi \end{pmatrix}, \quad \boldsymbol{R_1^{-1}} = \begin{pmatrix} 1 & 0 & 0 \\ 0 & \sin\phi & \cos\phi \\ 0 & -\cos\phi & \sin\phi \end{pmatrix}$$

$$\boldsymbol{R_2} = \begin{pmatrix} -\frac{1}{2} & \frac{\sqrt{3}}{2} & 0 \\ -\frac{\sqrt{3}}{2}\sin\phi & -\frac{1}{2}\sin\phi & -\cos\phi \\ -\frac{\sqrt{3}}{2}\cos\phi & -\frac{1}{2}\cos\phi & \sin\phi \end{pmatrix}, \quad \boldsymbol{R_2^{-1}} = \begin{pmatrix} -\frac{1}{2} & -\frac{\sqrt{3}}{2}\sin\phi & -\frac{\sqrt{3}}{2}\cos\phi \\ \frac{\sqrt{3}}{2} & -\frac{1}{2}\sin\phi & -\frac{1}{2}\cos\phi \\ 0 & -\cos\phi & \sin\phi \end{pmatrix}$$

$$\boldsymbol{R_3} = \begin{pmatrix} -\frac{1}{2} & -\frac{\sqrt{3}}{2} & 0 \\ \frac{\sqrt{3}}{2}\sin\phi & -\frac{1}{2}\sin\phi & -\cos\phi \\ \frac{\sqrt{3}}{2}\cos\phi & -\frac{1}{2}\cos\phi & \sin\phi \end{pmatrix}, \quad \boldsymbol{R_3^{-1}} = \begin{pmatrix} -\frac{1}{2} & \frac{\sqrt{3}}{2}\sin\phi & \frac{\sqrt{3}}{2}\cos\phi \\ -\frac{\sqrt{3}}{2} & -\frac{1}{2}\sin\phi & -\frac{1}{2}\cos\phi \\ 0 & -\cos\phi & \sin\phi \end{pmatrix}$$

$$\boldsymbol{R_4} = \begin{pmatrix} 1 & 0 & 0 \\ 0 & \sin\phi & \cos\phi \\ 0 & -\cos\phi & \sin\phi \end{pmatrix}, \quad \boldsymbol{R_4^{-1}} = \begin{pmatrix} 1 & 0 & 0 \\ 0 & \sin\phi & -\cos\phi \\ 0 & \cos\phi & \sin\phi \end{pmatrix}$$

$$\boldsymbol{R_5} = \begin{pmatrix} -\frac{1}{2} & \frac{\sqrt{3}}{2} & 0 \\ -\frac{\sqrt{3}}{2}\sin\phi & -\frac{1}{2}\sin\phi & \cos\phi \\ \frac{\sqrt{3}}{2}\cos\phi & \frac{1}{2}\cos\phi & \sin\phi \end{pmatrix},\ \boldsymbol{R_5^{-1}} = \begin{pmatrix} -\frac{1}{2} & -\frac{\sqrt{3}}{2}\sin\phi & \frac{\sqrt{3}}{2}\cos\phi \\ \frac{\sqrt{3}}{2} & -\frac{1}{2}\sin\phi & \frac{1}{2}\cos\phi \\ 0 & \cos\phi & \sin\phi \end{pmatrix}$$

$$\boldsymbol{R_6} = \begin{pmatrix} -\frac{1}{2} & -\frac{\sqrt{3}}{2} & 0 \\ \frac{\sqrt{3}}{2}\sin\phi & -\frac{1}{2}\sin\phi & \cos\phi \\ -\frac{\sqrt{3}}{2}\cos\phi & \frac{1}{2}\cos\phi & \sin\phi \end{pmatrix},\ \boldsymbol{R_6^{-1}} = \begin{pmatrix} -\frac{1}{2} & \frac{\sqrt{3}}{2}\sin\phi & -\frac{\sqrt{3}}{2}\cos\phi \\ -\frac{\sqrt{3}}{2} & -\frac{1}{2}\sin\phi & \frac{1}{2}\cos\phi \\ 0 & \cos\phi & \sin\phi \end{pmatrix}$$

Using transformation matrices mentioned above in the condition that $\boldsymbol{R_i^{-1}M_i'} = \boldsymbol{M_i}$, where $\boldsymbol{M_i'} = (M_i'^x, M_i'^y, M_i'^z)$, we can get $\boldsymbol{M_i}$ in the function of M_i' as follows

$$\boldsymbol{R_1^{-1}M_1'} = \boldsymbol{M_1} = \begin{pmatrix} M_1'^x \\ M_1'^y\sin\phi + M_1'^z\cos\phi \\ -M_1'^y\cos\phi + M_1'^z\sin\phi \end{pmatrix} \tag{34}$$

$$\boldsymbol{R_2^{-1}M_2'} = \boldsymbol{M_2} = \begin{pmatrix} -\frac{1}{2}M_2'^x - \frac{\sqrt{3}}{2}M_2'^y\sin\phi - \frac{\sqrt{3}}{2}M_2'^z\cos\phi \\ \frac{\sqrt{2}}{2}M_2'^x - \frac{1}{2}M_2'^y\sin\phi - \frac{1}{2}M_2'^z\cos\phi \\ -M_2'^y\cos\phi + M_2'^z\sin\phi \end{pmatrix} \tag{35}$$

$$\boldsymbol{R_3^{-1}M_3'} = \boldsymbol{M_3} = \begin{pmatrix} -\frac{1}{2}M_3'^x + \frac{\sqrt{3}}{2}M_3'^y\sin\phi + \frac{\sqrt{3}}{2}M_3'^z\cos\phi \\ -\frac{\sqrt{2}}{2}M_3'^x - \frac{1}{2}M_3'^y\sin\phi - \frac{1}{2}M_3'^z\cos\phi \\ -M_3'^y\cos\phi + M_3'^z\sin\phi \end{pmatrix} \tag{36}$$

$$\boldsymbol{R_4^{-1}M_4'} = \boldsymbol{M_4} = \begin{pmatrix} M_4'^x \\ M_4'^y\sin\phi - M_4'^z\cos\phi \\ M_4'^y\cos\phi + M_4'^z\sin\phi \end{pmatrix} \tag{37}$$

$$\boldsymbol{R_5^{-1}M_5'} = \boldsymbol{M_5} = \begin{pmatrix} -\frac{1}{2}M_5'^x - \frac{\sqrt{3}}{2}M_5'^y\sin\phi + \frac{\sqrt{3}}{2}M_5'^z\cos\phi \\ \frac{\sqrt{2}}{2}M_5'^x - \frac{1}{2}M_5'^y\sin\phi + \frac{1}{2}M_5'^z\cos\phi \\ M_5'^y\cos\phi + M_5'^z\sin\phi \end{pmatrix} \tag{38}$$

$$\boldsymbol{R_6^{-1}M_6'} = \boldsymbol{M_6} = \begin{pmatrix} -\frac{1}{2}M_6'^x + \frac{\sqrt{3}}{2}M_6'^y\sin\phi - \frac{\sqrt{3}}{2}M_6'^z\cos\phi \\ -\frac{\sqrt{2}}{2}M_6'^x - \frac{1}{2}M_6'^y\sin\phi + \frac{1}{2}M_6'^z\cos\phi \\ M_6'^y\cos\phi + M_6'^z\sin\phi \end{pmatrix} \tag{39}$$

Considering the equation of motion

$$\frac{1}{\gamma}\frac{d\boldsymbol{M}_i}{dt} = \boldsymbol{M}_i \times \boldsymbol{H}_i \tag{40}$$

By applying the matrix operations mentioned above to this equation of motion, we can get the relation that

$$\begin{aligned} \boldsymbol{R}_i\frac{1}{\gamma}\frac{d\boldsymbol{M}_i}{dt} =& \boldsymbol{R}_i(\boldsymbol{M}_i \times \boldsymbol{H}_i) \\ \frac{1}{\gamma}\frac{d\boldsymbol{M}'_i}{dt} =& \boldsymbol{R}_i(\boldsymbol{M}_i \times \boldsymbol{H}_i) \end{aligned} \tag{41}$$

By considering equation (32) and (33), the equation of the free energy can be written as

$$\begin{aligned} \boldsymbol{E} = & -\sum_{i=1}^{6} \boldsymbol{M_i} \cdot \boldsymbol{H} \\ & + A(\boldsymbol{M_1} \cdot \boldsymbol{M_4} + \boldsymbol{M_2} \cdot \boldsymbol{M_5} + \boldsymbol{M_3} \cdot \boldsymbol{M_6}) \\ & + B(\boldsymbol{M_1} \cdot \boldsymbol{M_2} + \boldsymbol{M_2} \cdot \boldsymbol{M_3} + \boldsymbol{M_3} \cdot \boldsymbol{M_1} + \boldsymbol{M_4} \cdot \boldsymbol{M_5} + \boldsymbol{M_5} \cdot \boldsymbol{M_6} + \boldsymbol{M_6} \cdot \boldsymbol{M_4}) \\ & + K(M_1^x M_2^x + M_2^x M_3^x + M_3^x M_1^x + M_4^x M_5^x + M_5^x M_6^x + M_6^x M_4^x \\ & \quad + M_1^y M_2^y + M_2^y M_3^y + M_3^y M_1^y + M_4^y M_5^y + M_5^y M_6^y + M_6^y M_4^y) \end{aligned} \tag{42}$$

As parameters A, B and K are corresponding to

$$A = \frac{6}{N}\frac{2J'}{(g\mu_B)^2}, \qquad B = \frac{6}{N}\frac{3J}{(g\mu_B)^2}, \qquad K = \frac{6}{N}\frac{3\Delta J}{(g\mu_B)^2} \tag{43}$$

A, B and K is the parameters refering to interlayer, intralayer, and anisotropic exchange interactions, respectively. However, magnetization of i^{th}sublattice can be written as

$$\boldsymbol{M_i} = \frac{N}{6} g\mu_B \langle S_i \rangle \tag{44}$$

where $< S_i >$ is average of spins at the thermal equilibrium in the i^{th} sublattice and N is the number of magnetic ions in the crystal. ϕ is the angle of between a direction of

tilting spin and the ab-plane due to an external magnetic field (H) parallel to the z axis. Then

$$\begin{aligned}\frac{\partial E}{\partial \phi} =& -6M_0 H\cos\phi + 6AM_0^2\sin 2\phi \\ &+ 18BM_0^2\cos\phi\sin\phi + 6KM_0^2\sin\phi\cos\phi = 0\end{aligned} \tag{45}$$

$$-H + (2A + 3B + K)M_0\sin\phi = 0 \tag{46}$$

We can see that

$$\sin\phi = \frac{H}{(2A + 3B + K)M_0} \tag{47}$$

Considering sublattice 1^{st}, there is a magnetization $\boldsymbol{M}_1$ caused by the external magnetic field $\boldsymbol{H}_1$. Since $H = dE/dM$, $\boldsymbol{H}_1$ can be described as

$$\boldsymbol{H_1} = \left(-\frac{\partial E}{\partial M_1^x}, \quad -\frac{\partial E}{\partial M_1^y}, \quad -\frac{\partial E}{\partial M_1^z} \right) \tag{48}$$

Considering a component in each axis, we can write H_1 as

$$\left.\begin{aligned} H_1^x =& -AM_4^x - (B+K)(M_2^x + M_3^x) \\ H_1^y =& -AM_4^y - (B+K)(M_2^y + M_3^y) \\ H_1^z =& H - AM_4^z - B(M_2^z + M_3^z) \end{aligned}\right\} \tag{49}$$

Because $M_i'^z \gg M_i'^x, M_i'^y$, we can assume that $M_i'^z \approx M_0$. Using matrix transformation mentioned above, we can transform M_i into M_i' as following

$$\left.\begin{aligned} H_1^x =& -AM_4'^x - \frac{B+K}{2}\left\{ M_2'^x + M_3'^x + \sqrt{3}(M_2'^y - M_3'^y)\sin\phi \right\} \\ H_1^y =& AM_0\cos\phi - AM_4'^4\sin\phi \\ &- \frac{B+K}{2}\{\sqrt{3}(M_2'^x - M_3'^x) - (M_2'^y + M_3'^y)\sin\phi - 2M_0\cos\phi\} \\ H_1^z =& H - AM_4'^y\cos\phi - AM_0\sin\phi + B\{(M_2'^y + M_3'^y)\cos\phi - 2M_0\sin\phi\} \end{aligned}\right\} \tag{50}$$

The cross product between $\boldsymbol{M_1} = (M_1'^x, M_1'^y \sin\phi + M_1'^z \cos\phi, -M_1'^y \cos\phi + M_1'^z \sin\phi)$ and $\boldsymbol{H_1} = (H_1^x, H_1^y, H_1^z)$ can be written as

$$\begin{aligned}
[\boldsymbol{M_1} \times \boldsymbol{H_1}]_x &= HM_1'^y \sin\phi - AM_0M_1'^y \sin^2\phi - 2BM_0M_1'^y \sin^2\phi + M_0H\cos\phi \\
&\quad - AM_0M_4'^y \cos^2\phi - AM^2 \sin\phi\cos\phi + BM_0(M_2'^y + M_3'^y)\cos^2\phi \\
&\quad - 2BM^2 \sin\phi\cos\phi + AM_0M_1'^y \cos^2\phi + (B+K)M_0M_1'^y \cos^2\phi \\
&\quad - AM_0^2 \sin\phi\cos\phi + AM_0M_4'^y \sin^2\phi \\
&\quad + \frac{\sqrt{3}}{2}(B+K)M_0(M_2'^x - M_3'^x)\sin\phi - \frac{B+K}{2}M_0(M_2'^x + M_3'^x)\sin^2\phi \\
&\quad - (B+K)M_0^2 \sin\phi\cos\phi \\
&= [\{H - (A+2B)M_0\sin\phi\}\sin\phi + (A+B+K)M_0\cos^2\phi]M_1'^y \\
&\quad - AM_0M_4'^y \cos 2\phi \\
&\quad + \frac{\sqrt{3}}{2}(B+K)M_0(M_2'^x - M_3'^x)\sin\phi \\
&\quad + \left\{B\left(\cos^2 - \frac{1}{2}\sin^2\phi\right) - \frac{K}{2}\sin^2\phi\right\}M_0(M_2'^y + M_3'^y)
\end{aligned} \tag{51}$$

$$\begin{aligned}
[\boldsymbol{M_1} \times \boldsymbol{H_1}]_y &= \{-H + (A+2B)M_0\sin\phi\}M_1'^x \; - AM_0M_1'^x \sin\phi \\
&\quad + \frac{B+K}{2}M_0(M_2'^x + M_3'^x)\sin\phi \\
&\quad + \frac{\sqrt{3}}{2}(B+K)M_0(M_2'^x - M_3'^x)\sin^2\phi
\end{aligned} \tag{52}$$

$$\begin{aligned}
[\boldsymbol{M_1} \times \boldsymbol{H_1}]_z &= (A+B+K)M_0M_1'^x \cos\phi \; - AM_0M_1'^x \cos\phi \\
&\quad - \frac{B+K}{2}M_0(M_2'^x + M_3'^x)\cos\phi \\
&\quad - \frac{\sqrt{3}}{2}(B+K)M_0(M_2'^x - M_3'^x)\sin\phi\cos\phi
\end{aligned} \tag{53}$$

The equations of motion of the magnetizations of sublattices can be described as

$$
\begin{aligned}
\frac{1}{\gamma}\frac{d\boldsymbol{M}_1'^x}{dt} &= [\boldsymbol{R_1}(\boldsymbol{M_1}\times\boldsymbol{H_1})]_x \\
&= [\boldsymbol{M_1}\times\boldsymbol{H_1}]_x \\
&= [H-(A+2B)M_0\sin\phi+(A+B+K)M_0\cos^2\phi]M_1'^y \\
&\quad -AM_0M_4'^y\cos 2\phi \\
&\quad +\frac{\sqrt{3}}{2}(B+K)M_0(M_2'^x-M_3'^x)\sin\phi \\
&\quad +\{B(\cos^2\phi-\frac{1}{2}\sin^2\phi)-\frac{K}{2}\sin^2\phi\}M_0(M_2'^y+M_3'^y) \\
&= (A+B+K)M_0M_1'^y-\{AM_0(1-2\sin^2\phi)\}M_4'^y \\
&\quad +\frac{\sqrt{3}}{2}(B+K)M_0(M_2'^x-M_3'^x)\sin\phi \\
&\quad +\{B(1-\frac{3}{2}\sin^2\phi)-\frac{K}{2}\sin^2\phi\}M_0(M_2'^y+M_3'^y)
\end{aligned}
\tag{54}
$$

$$
\begin{aligned}
\frac{1}{\gamma}\frac{d\boldsymbol{M}_1'^y}{dt} &= [\boldsymbol{R_1}(\boldsymbol{M_1}\times\boldsymbol{H_1})]_y \\
&= [\boldsymbol{M_1}\times\boldsymbol{H_1}]_y\sin\phi-[\boldsymbol{M_1}\times\boldsymbol{H_1}]_z\cos\phi \\
&= [-H\cos\phi+(A+2B)M_0\sin^2\phi-(A+B+K)M_0\cos^2\phi]M_1'^x \\
&\quad -AM_0M_4'^x \\
&\quad +\frac{B+K}{2}M_0(M_2'^x+M_3'^x) \\
&\quad +\frac{\sqrt{3}}{2}(B+K)M_0(M_2'^y-M_3'^y)\sin\phi \\
&= -(A+B+K)M_0M_1'^x-AM_0M_4'^x \\
&\quad +\frac{B+K}{2}M_0(M_2'^x+M_3'^x) \\
&\quad +\frac{\sqrt{3}}{2}(B+K)M_0(M_2'^y-M_3'^y)\sin\phi
\end{aligned}
\tag{55}
$$

$$
\begin{aligned}
\frac{1}{\gamma}\frac{d\boldsymbol{M}_1'^z} &= [\boldsymbol{R_1}(\boldsymbol{M_1}\times\boldsymbol{H_1})]_z \\
&= [\boldsymbol{M_1}\times\boldsymbol{H_1}]_y\cos\phi-[\boldsymbol{M_1}\times\boldsymbol{H_1}]_z\sin\phi \\
&= [-H\cos\phi+(A+2B)M_0\sin^2\phi-(A+B+K)M_0\cos^2\phi]M_1'^x \\
&= \{-H+(2A+3B+K)M_0\sin\phi\}M_1'^x\cos\phi \\
&= 0
\end{aligned}
\tag{56}
$$

The equations mentioned above are from the calculation of $\boldsymbol{M}_1'$. For the values of $\boldsymbol{M}_2'$, $\boldsymbol{M}_3'$, $\boldsymbol{M}_4'$, $\boldsymbol{M}_5'$ and $\boldsymbol{M}_6'$, we can obtain by replacing the cyclic numbers as following,

For $\boldsymbol{M}_2'$: cyclic change $1 \to 2$, $2 \to 3$, $3 \to 1$, and $4 \to 5$.

For $\boldsymbol{M}_3'$: cyclic change $1 \to 3$, $2 \to 2$, $3 \to 2$, and $4 \to 6$.

For $\boldsymbol{M}_4'$: cyclic change $1 \to 4$, $2 \to 5$, $3 \to 6$, and $4 \to 1$.

For $\boldsymbol{M}_5'$: cyclic change $1 \to 5$, $2 \to 6$, $3 \to 4$, and $4 \to 2$.

For $\boldsymbol{M}_6'$: cyclic change $1 \to 6$, $2 \to 4$, $3 \to 5$, and $4 \to 3$.

Here, we reduce the parameters in order to make it easier to solve the differential equation. Thus,

$$\left.\begin{aligned} \boldsymbol{M}_a &= \boldsymbol{M}_1' + \boldsymbol{M}_4' \\ \boldsymbol{M}_b &= \boldsymbol{M}_2' + \boldsymbol{M}_5' \\ \boldsymbol{M}_c &= \boldsymbol{M}_3' + \boldsymbol{M}_6' \end{aligned}\right\} \tag{57}$$

$$\begin{aligned} \frac{1}{\gamma}\frac{d\boldsymbol{M}_1'^x}{dt} = \; & (2A\sin^2\phi + B + K)M_0 M_a^y \\ & + \frac{\sqrt{3}}{2}(B+K)M_0(M_b^x - M_c^x)\sin\phi \\ & + \left\{B\left(1 - \frac{3}{2}\sin^2\phi\right) - \frac{K}{2}\sin^2\phi\right\}M_0(M_b^y + M_c^y) \end{aligned} \tag{58}$$

$$\begin{aligned} \frac{1}{\gamma}\frac{d\boldsymbol{M}_1'^y}{dt} = & -(2A + B + K)M_0 M_a'^x \\ & + \frac{B+K}{2}M_0(M_b'^x + M_c'^x) \\ & + \frac{\sqrt{3}}{2}(B+K)M_0(M_b^x - M_c^x)\sin\phi \end{aligned} \tag{59}$$

Since it is symmetry along z-axis, and a, b and c have a cyclic relation, the expression of $\boldsymbol{M}_a, \boldsymbol{M}_b$ and $\boldsymbol{M}_c$ can be described as

$$\left.\begin{aligned} \boldsymbol{M}_a^x = \lambda\Delta M\cos\omega t\ ,\ \boldsymbol{M}_a^y = \Delta M\sin\omega t \\ \boldsymbol{M}_b^x = \lambda\Delta M\cos\left(\omega t+\frac{2}{3}\pi\right)\ ,\ \boldsymbol{M}_b^y = \Delta M\sin\left(\omega t+\frac{2}{3}\pi\right) \\ \boldsymbol{M}_c^x = \lambda\Delta M\cos\left(\omega t+\frac{4}{3}\pi\right)\ ,\ \boldsymbol{M}_c^y = \Delta M\sin\left(\omega t+\frac{4}{3}\pi\right) \end{aligned}\right\} \tag{60}$$

Next, substitute equation (60) into equation (58), so that the result will be

$$\begin{aligned} -\frac{\omega}{\gamma}\lambda = (2A\sin^2\phi + B + K)M_0 - \frac{3}{2}\lambda(B+K)M_0\sin\phi \\ -\left\{B\left(1-\frac{3}{2}\sin^2\phi\right) - \frac{K}{2}\sin^2\phi\right\}M_0 \end{aligned} \tag{61}$$

Then, substitute equation (60) into equation (59), then it can be expressed as

$$-\frac{\omega}{\gamma} = \left(2A+\frac{3}{2}B+\frac{3}{2}K\right)M_0\lambda - \frac{3}{2}(B+K)M_0\sin\phi \tag{62}$$

$$\lambda = -\frac{\dfrac{\omega}{\gamma} - \dfrac{3}{2}\big(B+K\big)M_0\sin\phi}{(2A+\dfrac{3}{2}B+\dfrac{3}{2}K)M_0} \tag{63}$$

By substituting equation (63) into equation (61), and solving the quadratic equation of $\dfrac{\omega}{\gamma}$. In case the $\dfrac{\omega}{\gamma}$ is positive, ti can be expressed as

$$\begin{aligned} \left(\frac{\omega}{\gamma}\right)^2 = 3(B+K)M_0\sin(\phi)\left(\frac{\omega}{\gamma}\right) \\ -\left(2A+\frac{3}{2}B+\frac{3}{2}K\right)\left\{\left(2A+\frac{3}{2}B+\frac{3}{2}K\right)\sin^2\phi + K\right\}M_0^2 \\ +\frac{9}{4}(B+K)^2M_0^2\sin^2\phi = 0 \end{aligned} \tag{64}$$

$$\begin{aligned}\frac{\omega}{\gamma} &= \frac{1}{2}\sqrt{(4A+3B+3K)\{4A+3B+K)\sin^2\phi+2K\}M_0^2} \\ &\quad + \frac{3}{2}(B+K)M_0\sin^2\phi \\ &= \sqrt{K\left(2A+\frac{3}{2}B+\frac{3}{2}K\right)M_0^2 - \frac{\left(2A+\frac{3}{2}B+\frac{3}{2}K\right)\left(2A+\frac{3}{2}B+\frac{K}{2}\right)}{(2A+3B+K)^2}H^2} \\ &\quad + \frac{3(B+K)}{2(2A+3B+K)}H\end{aligned} \tag{65}$$

Next, substitute A, B, K and M_0 from (43) and (44), and multiply both sides of equation (65) by $\hbar\gamma$, and then we can express

$$\begin{aligned}\hbar\omega &= \sqrt{\left(4J'+\frac{9}{2}J+\frac{9}{2}\Delta J\right)\left\{\frac{3\Delta J}{4}+\frac{8J'+9J+3\Delta J}{2(4J'+9J+3\Delta J)^2}(g\mu_{\mathrm{B}}H)^2\right\}} \\ &\quad + \frac{9J+9\Delta J}{8J'+18J+6\Delta J}g\mu_{\mathrm{B}}H\end{aligned} \tag{66}$$

Observable ESR mode include $\omega_\pm$ is mentioned above.

$$\left.\begin{aligned}\boldsymbol{M}_a^x = \lambda\Delta M_0\cos\omega t\ ,\ \boldsymbol{M}_a^y &= \Delta M_0\sin\omega t \\ \boldsymbol{M}_b^x = \lambda\Delta M_0\cos\left(\omega t-\frac{2}{3}\pi\right)\ ,\ \boldsymbol{M}_b^y &= \Delta M_0\sin\left(\omega t-\frac{2}{3}\pi\right) \\ \boldsymbol{M}_c^x = \lambda\Delta M_0\cos\left(\omega t-\frac{4}{3}\pi\right)\ ,\ \boldsymbol{M}_c^y &= \Delta M_0\sin\left(\omega t-\frac{4}{3}\pi\right)\end{aligned}\right\} \tag{67}$$

For other observable ESR mode, we can follow the same procedure as the $\omega_\pm$ one

$$\left.\begin{aligned}\boldsymbol{M}_a^x = \boldsymbol{M}_b^x = \boldsymbol{M}_c^x &= \Delta M_0\cos\omega t \\ \boldsymbol{M}_a^y = \boldsymbol{M}_b^y = \boldsymbol{M}_c^y &= \lambda\Delta M_0\sin\omega t\end{aligned}\right\} \tag{68}$$

From the equations above, finally, the result is

$$\frac{\omega}{\gamma} = 0 \tag{69}$$

This ESR mode is corresponding to a uniform rotational movement around the magnetic field. Since the restoration force has no work done, the excitation energy becomes zero.

REFERENCES

[1] A. Abragam and M. H. L. Pryce, Proc. R. Soc. London Ser. A **206**, 173 (1956).

[2] M. E. Lines, Phys. Rev. **131**, 546 (1963).

[3] A. V. Chubokov and D. I. Golosov, J. Phys.: Condens. Matter **3**, 69 (1999).

[4] T. Nikuni and H. Shiba, J. Phys. Soc. Jpn. **62**, 3268 (1993).

[5] A. Honecker, J. Phys.: Condens. Matter **11**, 4697 (1999).

[6] D. J. J. Farnell, R. Zinke, J. Schulenburg, and J. Richter, J. Phys.: Condens. Matter **21**, 406002 (2009).

[7] T. Sakai and H. Nakano, Phys. Rev. B **83**, 100405(R) (2011).

[8] C. Hotta, S. Nishimoto, and N. Shibata, Phys. Rev. B **87**, 115128 (2013).

[9] D. Yamamoto, G. Marmorini, and I. Danshita, Phys. Rev. Lett. **112**, 127203 (2014).

[10] D. Sellmann, X. F. Zhang, and S. Eggert, Phys. Rev. B **91**, 081104 (2015).

[11] O. Starykh, Rep. Prog. Phys. **78**, 052502 (2015).

[12] D. Yamamoto, G. Marmorini, and I. Danshita, Phys. Rev. Lett. **114**, 027201 (2015).

[13] Y. Shirata, H. Tanaka, T. Ono, A. Matsuo, K. Kindo, and H. Nakano, J. Phys. Soc. Jpn. **80**, 093702 (2011).

[14] Y. Shirata, H. Tanaka, A. Matsuo, and K. Kindo, Phys. Rev. Lett. **108**, 057205 (2012).

[15] H. D. Zhou, C. Xu, A. M. Hallas, H. J. Silverstein, C. R. Wiebe, I. Umegaki, J. Q. Yan, T. P. Murphy, J. H. Park, Y. Qiu, J. R. D. Copley, J. S. Gardner, Y. Takano, Phys. Rev. Lett. **109**, 267206 (2012).

[16] T. Susuki, N. Kurita, T. Tanaka, H. Nojiri, A. Matsuo, K. Kindo, and H. Tanaka, Phys. Rev. Lett. **110**, 267201 (2013).

[17] G. Quirion, M. Lapointe-Major, M. Poirier, J. A. Quilliam, Z. L. Dun, and H. D. Zhou, Phys. Rev. B **92**, 014414 (2015).

[18] G. Koutroulakis, T. Zhou, Y. Kamiya, J. D. Thompson, H. D. Zhou, C. D. Batista, and S. E. Brown, Phys. Rev. B **91**, 024410 (2015).

[19] J. Ma, Y. Kamiya, T. Hong, H. B. Cao, G. Ehlers, W. Tian, C. D. Batista, Z. L. Dun, H. D. Zhou, and M. Matsuda, Phys. Rev. Lett. **116**, 087201 (2016).

[20] M. Matsuda, M. Azuma, M. Tokunaga, Y. Shimakawa, and N. Kumada, Phys. Rev. Lett. **105**, 187201 (2010).

[21] H. Mosadeq, F. Shahbazi, and S. A. Jafari, J. Phys.: Condens. Matter **23**, 226006 (2011).

[22] R. Ganesh, D. N. Sheng, Y. J. Kim, and A. Paramekanti, Phys. Rev. B **83**, 219903 (2011).

[23] R. Ganesh, S. Nishimoto, and J. van den Brink, Phys. Rev. B **87**, 054413 (2013).

[24] Y. Doi, Y. Hinatsu, and K. Ohoyama, J. Phys.: Condens. Matter **16**, 8923 (2004).

[25] S. Miyahara, K. Ueda, J. Phys.: Condens. Matter **15**, R327 (2003).

[26] S. Nishimoto, N. Shibata, and C. Hotta, Nat. Commun. **4**, 2287 (2013).

[27] S. Capponi, O. Derzhko, A. Honecker, A. M. Lauchli, and J. Richter, Phys. Rev. B **88**, 144416 (2016).

[28] P. W. Anderson, Mat. Res. Bull. **8**, 153 (1973).

[29] P. Fazekas and P. W. Anderson, Philo. Mag. **30**, 423 (1974).

[30] D. A. Huse and V. Elser, Phys. Rev. Lett. **60**, 2531 (1988).

[31] T. Jolicoeur and J. C. Le Guillou, Phys. Rev. B **40**, 2727 (1989).

[32] B. Bernu, P. Lecheminant, C. Lüthi, and L. Pierre, Phys. Rev. B **50**, 10048 (1994).

[33] R. R. P. Singh and D. A. Huse, Phys. Rev. Lett. **68**, 1766 (1992).

[34] S. R. White and A. L. Chenyshev, Phys. Rev. Lett. **99**, 127004 (2007).

[35] L. Balents, Nature **464**, 199 (2010).

[36] J. Alicea, A. V. Chubukov, and O. A. Starykh, Phys. Rev. Lett. **102**, 137201 (2009).

[37] T. Ono, H. Tanaka, H. A. Katori, F. Ishikawa, H. Mitamura, and T. Goto, Phys. Rev. B **67**, 104431 (2003).

[38] T. Ono, H. Tanaka, O. Kolomiyets, H. Mitamura, T. Goto, K. Nakajima, A. Oosawa, Y. Koike, K. Kakurai, J. Klenke, P. Smeibidle, M. Meissner: J. Phys.: Condens. Matter **16**, S773 (2004).

[39] O. A. Starykh, A. V. Chubukov, and A. G. Abanov, Phys. Rev. B **74**, 052502 (2006).

[40] W. Zheng, J. O. Fjærestad, R. R. P. Singh, R. H. McKenzie, and R. Coldea, Phys. Rev. B **74**, 224420 (2006).

[41] A. L. Chernyshev and M. E. Zhitomirsky, Phys. Rev. B **79**, 144416 (2009).

[42] A. Mezio, C. N. Sposetti, L. O. Manuel, and A. E. Trumper, Europhys. Lett. **94**, 47001 (2010).

[43] M. Mourigal, W. T. Fuhrman, A. L. Chernyshev, and M. E. Zhitomirsky, Phys. Rev. B **93**, 099901 (2016).

[44] E. A. Ghioldi, A. Mezio, L. O. Manuel, R. R. P. Singh, J. Oitmaa, and A. E. Trumper, Phys. Rev. B **91**, 134423 (2015).

[45] B. L. W. Palme, F. Mertens, O. Born, Solid State Commun. **76**, 873 (1990).

[46] H. Nojiri, Y. Tokunaga, and M. Motokawa, J. Phys. (Paris) **49** Supplementary C8, 1459 (1988).

[47] K. Adachi, N. Achiwa, and M. Mekata, J. Phys. Soc. Jpn. **49**, 545 (1980).

[48] H. Tanaka, U. Schotte, and K. D. Schotte, J. Phys. Soc. Jpn. **61**, 1344 (1992).

[49] A. Sera, Y. Kousaka, J. Akimitsu, M. Sera, and K. Inoue, Phys. Rev. B **96**, 014419 (2017).

[50] N. A. Fortune, S. T. Hannahs, Y. Yoshida, T. E. Sherline, T. Ono, H. Tanaka, and Y. Takano, Phys. Rev. Lett. **102**, 26 (2009).

[51] S. Ito, N. Kurita, H. Tanaka, S. Ohira-Kawamura, K. Nakajima, S. Itoh, K. Kuwahara, and K. Kakurai, Nat. Commun. (to be published).

[52] E. Rastelli, A. Tassi, and L. Reatto, Physica B **97**, 1 (1979).

[53] J. B. Fouet, P. Sindzingre, and C. Lhuillier, Eur. Phys. J. B **20**, 241 (2001).

[54] H. Kobayashi and T. Haseda, J. Phys. Soc. Jpn. **19**, 765 (1964).

[55] J. Kanamori, Prog. Theor. Phys. **35**, 16 (1966).

[56] S. A. Ivanov, P. Nordblad, R. Mathieu, R. Tellgren, and C. Ritter, Dalton Trans. **39**, 5490 (2010).

[57] K. Yokota, N. Kurita, and H. Tanaka, Phys. Rev. B **90**, 014403 (2014).

[58] T. Koga, N. Kurita, M. Avdeev, S. Danilkin, T. J. Sato, and H. Tanaka, Phys. Rev. B **93**, 054426 (2016).

[59] Q. D. Inc., MPMS XL Hardware Reference Manual, Quantum Design Inc., Santiago C.A. (2005).

[60] K. Kindo, Meas. Sci. Technol. **14** 2144 (2003).

[61] J. P. Shepherd, Rev. Sci. Instrum. **56**, 273 (1985).

[62] K. Katayama, Ph.D. dissertation, Tokyo Institute of Technology (2016).

[63] H. Nojiri, and Z. W. Ouyang, Terahertz Sci. Technol. **5**, 1 (2012).

[64] H. Tanaka, S. Teraoka, E. Kakehashi, K. Ito, and K. Nagata, J. Phys. Soc. Jpn. **57**, 3979 (1988).

[65] University of Basel, Molecular spectroscopy and chemical dynamics lecture note (2013).

[66] T. Susuki, Master thesis, Tokyo Institute of Technology (2014).

[67] A. Sera, Y. Kousaka, J. Akimitsu, M. Sera, T. Kawamata, Y. Koike, and K. Inoue, Phys. Rev. B **93**, 214408 (2016).

PUBLICATION LIST

- P. Chanlert, N. Kurita, H. Tanaka, D. Goto, A. Matsuo, and K. Kindo, Field-driven successive phase transitions in the quasi-two-dimensional frustrated antiferromagnet Ba_2CoTeO_6 and highly degenerate classical ground states, Phys. Rev. B **94**, 094420 (2016).

- G. Gitgeatpong, M. Suewattana, Shiwei Zhang, A. Miyake, M. Tokunaga, P. Chanlert, N. Kurita, H. Tanaka, T. J. Sato, Y. Zhao, and K. Matan, High-field magnetization and magnetic phase diagram of $\alpha-Cu_2V_2O_7$, Phys. Rev. B **95** 245119 (2017).

- P. Chanlert, N. Kurita, H. Tanaka, M. Kimata, and H. Nojiri, Collective and local excitations in Ba_2CoTeO_6: A composite system of a spin-1/2 triangular-lattice Heisenberg antiferromagnet and a honeycomb-lattice J_1-J_2 Ising antiferromagnet, Phys. Rev. B **96** 064419 (2017).